Volume: 3 Issue: 2 2022

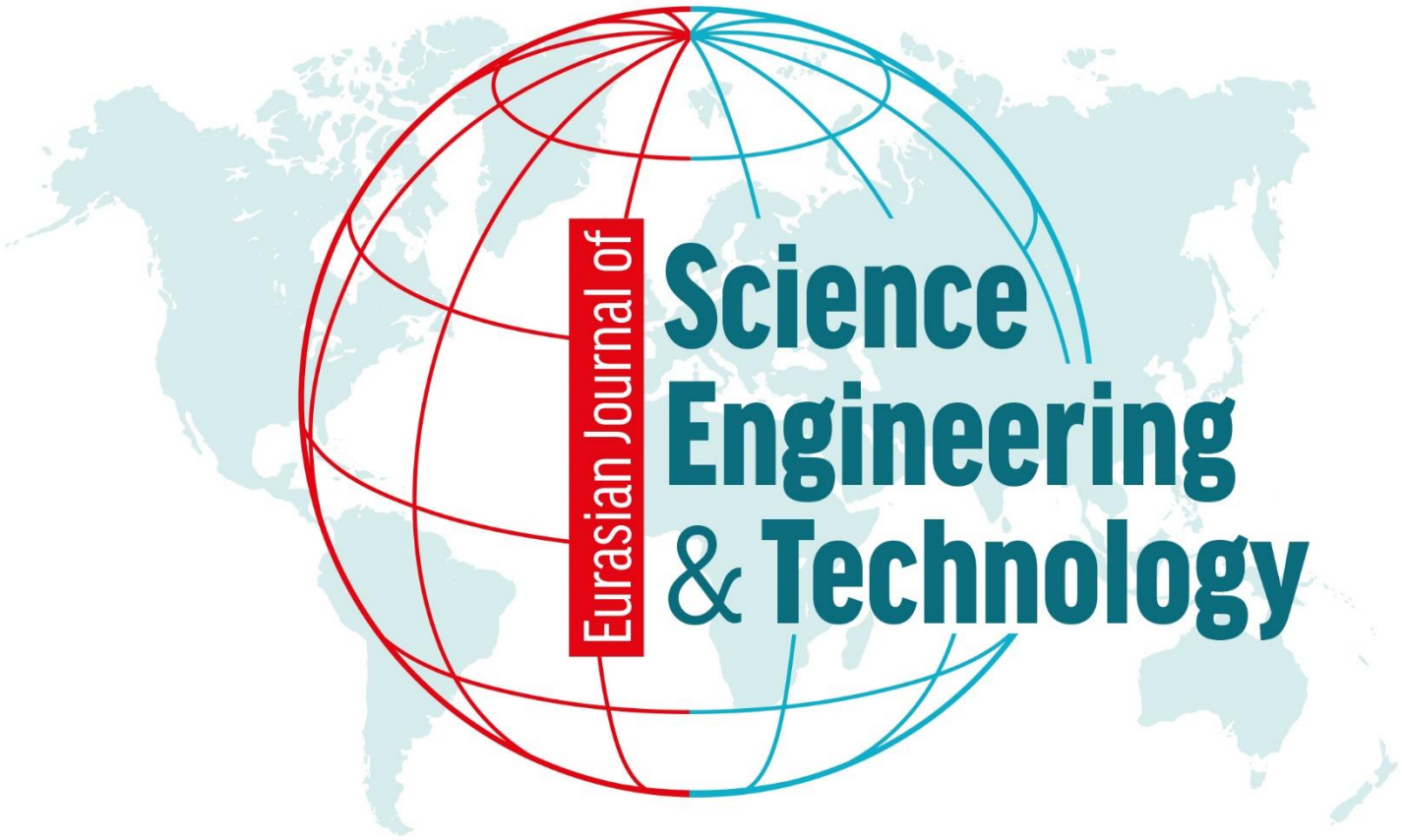

Eurasian Journal of Science Engineering and Technology

Editors

Editorial Board

Eurasian Journal of Science Engineering and Technology

Scientific Board

Eurasian Journal of Science Engineering and Technology

Correspondence Address

Niğde Ömer Halisdemir University
Eurasian Journal of Science Engineering and Technology Publishing Coordinatorship, 51240
Niğde/Türkiye

***E-mail*:** recep.zan@ohu.edu.tr

***Web page*:** https://dergipark.org.tr/tr/pub/ejset

Publication information

The objective of Eurasian Journal of Science Engineering and Technology (EJSET) is to provide an academic environment for researchers in various fields of science and engineering and for the publication and dissemination of high-quality research results in the fields of science, applied science, engineering, architecture, agricultural science and technology.

Eurasian Journal of Science Engineering and Technology

CONTENTS/*İÇİNDEKİLER*

MONTE-CARLO (MC) ANALYSIS OF BORATED MATERIALS FOR NEUTRON SHIELDING APPLICATIONS

(Research Article)

Abdul Rahman ALBAROUDI, Pelin USLU KİÇECİ, Selcen UZUN DURAN, M. Bilge DEMİRKÖZ

63-70

GURSON-TVERGAARD-NEEDLEMAN (GTN) PARAMETERS OF DP STEELS WITH DIFFERENT ROLLING DIRECTIONS WERE DETERMINED AND INVESTIGATED AT DIFFERENT STRAIN RATES

(Research Article)

Labinot TOPILLA, Serkan TOROS

71-83

A COMPARATIVE STUDY ON THE PHOTORESIST PATTERNING OF GLASS AND SILICON WITH MICROHOLES VIA MASKLESS PHOTOLITHOGRAPHY

(Research Article)

Furkan GÜÇLÜER, Filiz KELEŞ

84-90

INVESTIGATION OF THE EFFECT OF BENDING PROCESS ON FATIGUE LIFE AND MECHANICAL STRENGTH OF HEAVY COMMERCIAL VEHICLE DRAG LINKS

(Research Article)

İbrahim KILINÇ, Serkan TOROS

91-102

A CASE STUDY ON COST ANALYSIS AND LOAD ESTIMATION OF HYBRID RENEWABLE ENERGY SYSTEM USING HOMER PRO

(Research Article)

Saba MUNIR, Ausnain NAVEED, Raja Tahir IQBAL, Mohtasim USMAN

103-108

THE INFLUENCE OF POST-ANNEALING CdS THIN FILMS GROWN ON ZnO SEED LAYER FOR CdTe SOLAR CELLS

(Research Article)

Ali ÇİRİŞ

109-115

Eurasian Journal of Science Engineering and Technology

Research

MONTE-CARLO (MC) ANALYSIS OF BORATED MATERIALS FOR NEUTRON SHIELDING APPLICATIONS

Abdul Rahman ALBAROUDI[1], Pelin USLU KİÇECİ[2], Selcen UZUN DURAN[3,*], M. Bilge DEMİRKÖZ[4]

[1,2,4]*The Research and Application Center for Space and Accelerator Technologies, Middle East Technical University, Ankara-Türkiye*
[3]*Program of Medical Imaging Techniques, Vocational School of Health Sciences, Karadeniz Technical University, Trabzon, Türkiye*

ABSTRACT

Neutron shielding is of utmost importance in radiation environments such as nuclear reactors and particle accelerators and in fields such as health physics. In this work, the percentages of neutrons stopped by shields comprising of boron minerals (HDPE/B2O3, Epoxy/Priceite, Epoxy/Colemanite, Epoxy/Kernite) in their composition against neutron radiation of different energies is investigated using two separate MC simulations. Different layer combinations of epoxy based borated shielding materials with HDPE sheets were then simulated to find the optimum shielding configuration. In addition, radioactivation studies were carried out for these designs. The most suitable design was found to be the layered setup of the HDPE sheet and the epoxy/colemanite composite sheet for mixed neutron energies (<1MeV).

Keywords: Neutron shielding, Monte-Carlo simulations, Borated materials, Boron composites.

1. INTRODUCTION

Low energy and thermal neutrons are considered to be of significant threat to human health and electronic equipment [1]. Nuclear reactors and particle accelerators can generate high fluxes of neutron radiation. Therefore, shielding is very important to protect the workers and the equipment in these facilities from the detrimental effects of radiation. In principle, a good neutron radiation shield is composed of a combination of light elements, such as hydrogen (H) and carbon (C) for neutron moderation, and high neutron absorption cross-section (Σabs) having elements such as boron (B), lithium (Li) and cadmium (Cd) for neutron capture. Therefore, hydrogen-rich polymers can be used to thermalize neutrons (KE=0.025 eV at 20 ^{0}C) which are then captured and absorbed through boron-containing compounds. The higher the number of stopped neutrons, the better the neutron attenuation efficiency of the shield [2]. High carbon and hydrogen content materials such as polyethylene, paraffin and concrete are typically used against neutrons for protection based on the large and constant nature of the total cross section of neutrons for carbon and hydrogen in the energy range between 0.1 MeV and 0.1 eV as shown in Fig. 1 [3,4]. The high total neutron cross-section of the atoms in a hydrocarbon polymer matrix makes it one of the most effective candidates for low energy applications, especially high-density polyethylene (HDPE), which is a widely used material due to its high density, availability, affordability, and desirable mechanical properties.

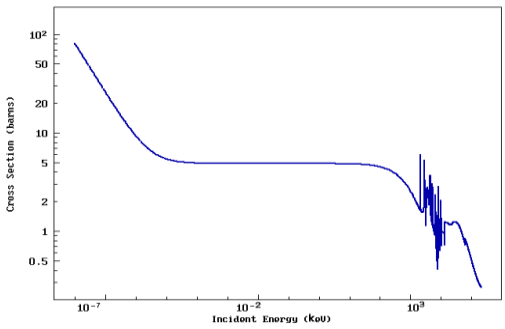

Figure 1. Total neutron cross-section for Carbon-12. [3]

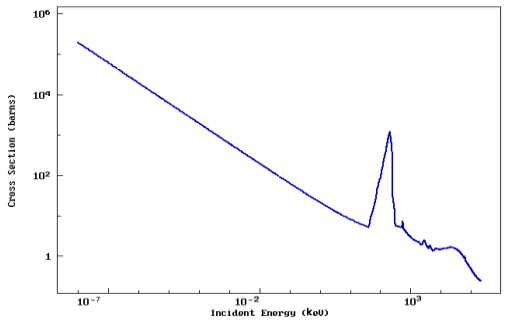

Figure 2. Total neutron cross-section for Boron-10. [3]

* Corresponding author, e-mail: selcenduran@ktu.edu.tr (S. Uzun Duran)
Recieved: 12.04.2022 Accepted: 18.07.2022
doi: 10.55696/ejset.1102371

Another good neutron shielding material candidate is boron, which has two naturally abundant and stable isotopes, B-10, and B-11. 20% of all-natural boron is B-10 and it has a very high absorption cross-section of slow neutrons to transition into the more stable isotope B-11 [4]. Total neutron cross-section for B-10 is shown in Fig. 2. The high cross-section at the thermal neutron capture region is very favorable for shielding applications, since it results in the production of a stable B-11 nucleus that is not going to decay. This prevents unnecessary activation of the shielding material.

The total neutron cross-section B-10 and its production of B-11 daughters, along with its relatively high natural abundance, makes it a very good contender for shielding materials against low energy neutrons compared to other alternatives, such as heavy metals, which can be poisonous, and add significant weight to the shielding. Boron is lighter, safer, and much more available [5]. In this work, the effect of adding boron salts and boron containing minerals into existing shielding setups is investigated using Monte-Carlo simulation methods with the Geant4 toolkit and MCNP6. The aim of this study is to find the optimum shielding configuration by determining the percentages of neutrons stopped in their compositions against neutron radiation of different energies by shields made of boron minerals (HDPE/B_2O_3, Epoxy/Priceite, Epoxy/Colemanite, Epoxy/Kernite).

2. MATERIAL AND METHOD

2.1. Monte-Carlo Simulations

In applications involving radiation, Monte Carlo method and simulation technique provide modeling and animation of experimental conditions in computer environment. With this method, devices and materials producing radiation can be simulated in the computer environment and exposed to radiation. Products doped with different materials can be tested without the physical difficulties caused by the experimental conditions, and a wide range of material analysis can be performed inexpensively.

The Monte-Carlo analysis in this work is done using Geant4 and MCNP6. A C++ program using the Geant4 toolkit was written to evaluate the performance of the different suggested shielding configurations by sending in a beam of neutrons with normal incidence towards the shield [6]. The percentage of neutrons that are completely stopped inside the shield is used as a measure of performance. Slowed down neutrons and thermal energy neutrons are still considered to be highly damaging, thus only neutrons that lose all their kinetic energy and are absorbed by the shielding material are accounted for in this case. Nevertheless, the slowing down of neutrons inside polyethylene is also investigated as a part of the effort to obtain the optimum boron concentration.

The neutron gun in the simulation is rectangular, 2.0×2.0 cm in size and placed 50 cm from the target. The gun has multiple energy settings with monoenergetic and mixed energies representing high energy (HE) and low energy (LE) regions for neutrons. Therefore, samples can be tested for neutrons in different energy ranges. The different energy settings of the gun can be found in Table 1. The high and low energy linear spectra are meant to represent the behavior of mixed neutron energy distributions within shielding materials.

Table 1. Neutron beam energy specifications defined in Geant4 simulation

ENERGY SETTING	ENERGY	SPECTRUM
Thermal neutrons	0.025 eV	Mono-Energetic
Epithermal neutrons	0.2 eV	Mono-Energetic
Slow neutrons	5 eV	Mono-Energetic
Fast neutrons	20 MeV	Mono-Energetic
High Energy (HE)	1 MeV-1 keV	Linear Gradient = 1 intercept = 1
Low Energy (LE)	1 keV-1 eV	Linear Gradient = 1 intercept = 1

The prepackaged physics list FTFP-BERT-HP was used along with the G4ENDL4.5 datasets to achieve the most accuracy in the Geant4 simulation [6]. This physics-list is modified form the original FTFP-BERT for high energy physics experiments to add high precision calculations for low energy neutron interactions. However, it does not allow for radioactive decay to take place, which is necessary to observe the effects of the activation of the shielding material. It also lacks the inclusion of low energy electromagnetic processes. But since the simulation runs for only neutrons as incident particles and to make the simulation more efficient, this physics-list was chosen. As for the study of activation, FLUKA was used to qualitatively determine the radioactive isotopes produced by each proposed shielding material.

Layers of materials are placed against the neutron beam with a scoring volume on the opposite side as shown in Figure 3. The layers have lateral dimensions of 30.0×30.0 cm. The thickness of the target material was selected as 1 cm and 5 cm to observe the efficiency and the scaling effect on the shielding performance. The scoring volume behind is 20% larger in area to account for particles exiting the shielding layer with large momentum components in the lateral direction.

The Monte-Carlo analyses were also performed using MCNP6. It is a general-purpose code that is developed by Los Alamos Laboratory to track many particle types over a broad range of energies. The beam energy and geometry were the same as in Geant4. Stopping percentages of the shielding materials were found using the F1 tally. It calculates the particle current passing from the target surface. Therefore, this tally is used for the calculation of the percentages of the stopping neutrons in the shielding material.

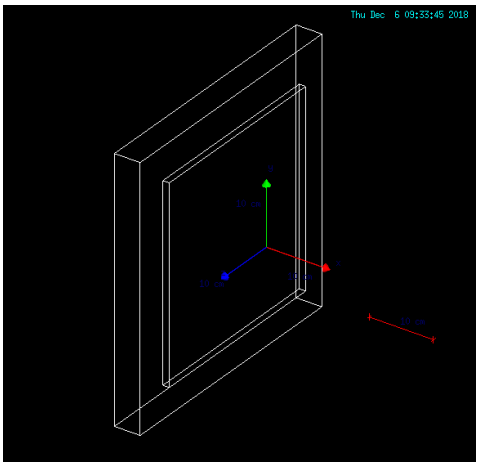

Figure 3. Single sheet testing setup inside Geant4 environment.

2.2. Candidate Material Selection

HDPE and HDPE/B_2O_3 composites are widely used as effective neutron shielding materials, but they have poor mechanical strength, heat resistance and durability [1-7-8]. Epoxy resin is used for coating floors in radiation facilities since it has good durability against gamma ray and neutron irradiation. Therefore, a mix of epoxy resin with boron carbide is used in a nuclear fuel cask, but boron carbide is very expensive. Therefore, a new neutron shielding material based on colemanite and epoxy resin was developed, and its shielding performance was also estimated in this study [9].

Valuable boron compounds such as colemanite ($Ca_2B_6O_{11}.5H_2O$), tincal ($Na_2B_4O_7.5H_2O$) and ulexite ($NaCaB_5O_9.8H_2O$) have found various application areas [10]. Colemanite, tincal and ulexite are thoroughly investigated in literature [10-11-12-13-14-15-16]. On the other hand, studies about kernite ($Na_2[B_4O_6(OH)_2]\cdot 4H_2O$) and Priceite ($Ca_2B_5O_7(OH)5\cdot H_2O$) minerals and their neutron shielding effects are limited.

In this study, borated HDPE is tested to show an improvement on the thermal neutron absorption of HDPE as boron is added into the polymer matrix uniformly. The aim is to use the large carbon content to slow down the energetic neutrons to thermal energies via scattering, at which point a B-10 nucleus is 104 times more likely to capture the neutron than any other atomic constituent of HDPE. There exist many commercial setups for the incorporation of powders into the HDPE polymer matrix that would be useful for such purposes [18].

The thermal, electrical, and surface characteristics of such a composite material is thoroughly investigated in the literature [1,5,15-20]. The amount of boron inside the shield was changed to see the effects of increasing boron concentration in the mixture and whether an optimum composition exists. Also, the thicknesses of the shields were changed as 1 and 5 cm.

Other materials were tested with polyethylene in layered setups using the same working principle. Boron rich minerals infused within epoxy resins were tested, including Kernite ($Na_2[B_4O_6(OH)_2]\cdot 4H2O$), Priceite ($Ca_2B_5O_7(OH)_5\cdot H_2O$) and Colemanite ($CaB_3O_4(OH)_3\cdot H_2O$). These materials are readily supplied commercially as solid sheets and powders. Each candidate was tested in a setup in which a 2.5 cm thick layer of the material was placed either before or after a similarly sized HDPE layer. 55% epoxy and 45% boron mineral were used in each material. The volumetric makeup of the composite material is given in Table 2.

Table 1. Volumetric breakdown of the composition of the shielding sheet material.

	Mineral	**Epoxy**
% Volume	55%	45%

2.3. Binning and Data Analysis

Neutrons exhibit a highly probabilistic behavior when interacting with matter. Two neutrons of the same energy may pass the same thickness of shield with one experiencing negligible energy loss and the other being completely absorbed by it. Therefore, Monte-Carlo simulations must incorporate a very high number of primary particles and average the results over all events to assess the integrated effect of all particles. By binning specific energy ranges and averaging interactions over it, the shield's performance can be assessed. The slowdown of neutrons inside the shield was calculated from the kinetic energies of neutrons using the following formula:

$$\%slowdown = \frac{\sum_i^n ((E_i(i) - E_f(i))/E_i(i)\ )}{n} * 100 \quad (1)$$

Where n is the number of particles inside the bin, Ei (i) is the initial energy of the ith neutron in the bin, Ef (i) is the energy of the ith neutron after passing through the shield.

3. RESULTS AND DISCUSSION

3.1. Borated Polyethylene

Using the Monte-Carlo simulations and using the equation defined in the method, a 5 cm thick borated HDPE sheet with different percentages of boron slowed down neutrons with effectiveness shown in Fig. 4.

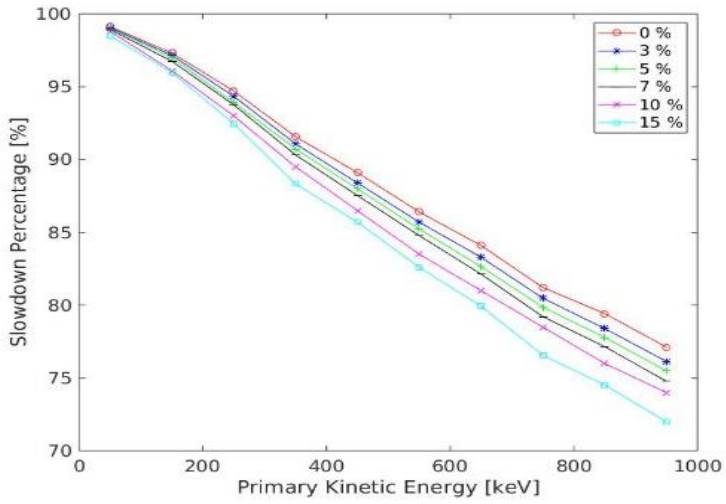

Figure 4. Neutron stopping percentages of HDPE sheet, depending on different neutron energies and different boron ratios.

As the concentration of boron inside polyethylene increases, the advantage gained diminishes. That is because as the percentage of boron increases, the number density of carbon decreases, making it less probable for the neutron to scatter off it and thus compromising the potential of the boron capturing it.

The simulation was repeated while changing the thicknesses and the energy ranges of the beam to better visualize the advantages of certain concentration values and to determine the optimum concentration of boron in the sheet. A 1 cm thick sheet was subjected to the beam and the amount of stopped neutrons was counted for by different beam energy settings, the results of which are shown in Fig. 5-a.

The difference in the shielding effectiveness between pure HDPE and borated HDPE is very significant at low neutron energies. The concentration of boron has a decaying effect on the shielding efficiency after 5% for low energy neutrons. For higher energy neutrons, the effect is very subtle and is not significant. The minor change in shielding performance is shown in Fig. 5-b to emphasize more on how the shield interacts with the mixed energy beam HE and LE.

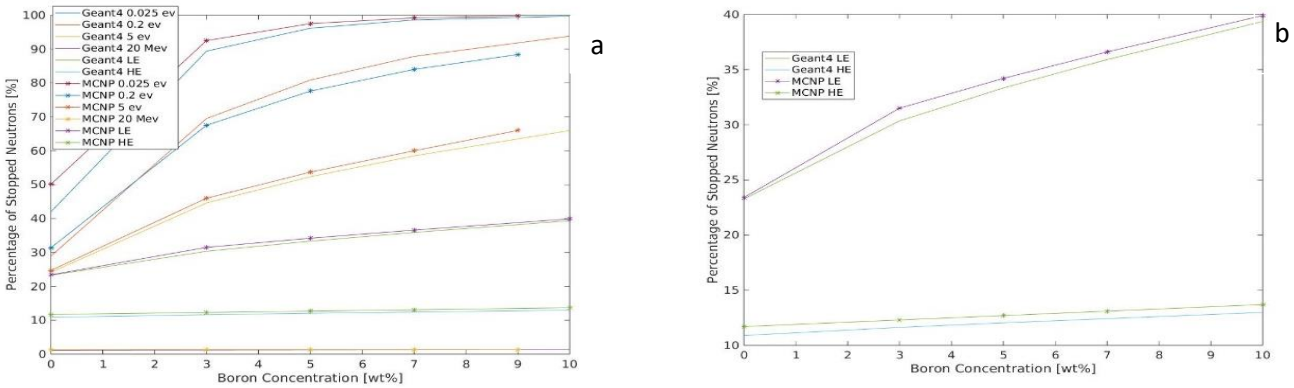

Figure 5-a: The Percentage of stopped neutrons of 1 cm thick HDPE, depending on the boron ratio. **5-b:** The Percentage of stopped neutrons of 1 cm thick HDPE sheet, for HE and LE neutrons, depending on different boron ratios. Error bars < 0.1%.

Fig. 5-b shows that the LE beam achieves more shield penetration with increasing boron concentration, while the HE beam exhibits the opposite behavior. Upon further investigation by sending a linear energy spectrum with the same parameters between 1 MeV and 1 eV and increasing the thickness to 5 cm, a peak in the shield performance can be seen at 5% boron concentration in Fig. 6-a. This observation further verifies the explanation behind the diminishing return of stopping neutrons on increasing boron concentrations, since boron has a low cross-section of absorption for high energy neutrons and less carbon is present to scatter the energy off. This effect being more prominent at 5 cm thickness is to be expected since addition of more shielding material will provide enough scattering medium to emphasize this effect.

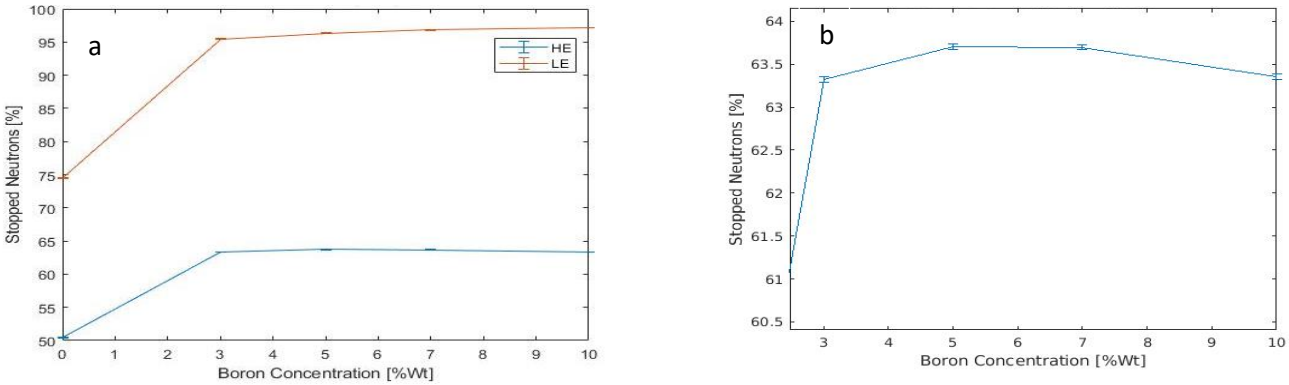

Figure 6-a. The Percentage of Stopped Neutrons of 5 cm Thick HDPE Sheet, For HE and LE Neutrons, Depending on Different Boron Ratios. **Figure 6-b.** Close-Up of The HE Neutrons Results.

The scaling up of the behavior of neutrons with the thickness of the shield can be seen in Fig. 7, in which a comparison of the two thicknesses is made for the LE beam. The biggest jump in performance is again made at 5% boron concentration, after which the gain in performance diminishes significantly. Close to 96% of LE neutrons are shown to be stopped by a mere 5 cm thickness of this lightweight shield.

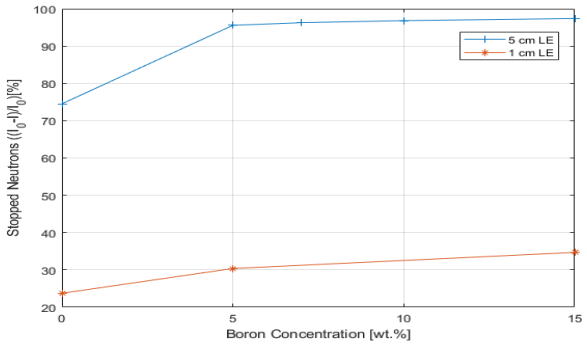

Figure 7. Comparison between the performance of the shield at 1 cm and 5 cm. Plotted for the LE beam.

3.2. Epoxy/Boron Composites

Sheets of epoxy resin incorporating boron rich minerals (Colemanite, Priceite and Kernite) were tested using the same simulation environment as borated polyethylene. First, colemanite sheets were tested at thicknesses of 1 and 5 cm and with both beam configurations. The results can be seen in Fig. 8.

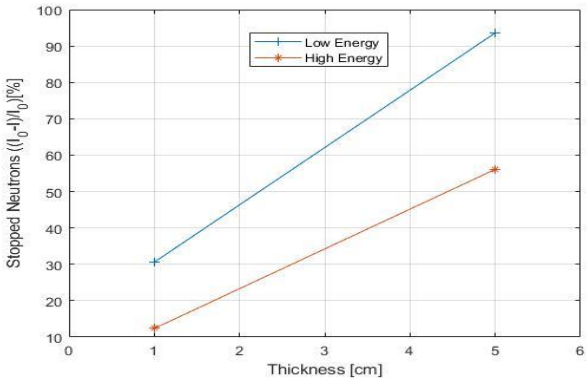

Figure 8. The percentage of stopped neutrons relative to the thickness of the epoxy-colemanite-containing sheet for LE and HE neutrons.

At high energies, Epoxy/Colemanite composite behaves poorly compared to Polyethylene due to the lower concentration of carbon and hydrogen atoms in the material. However, when using LE beam, the sheet achieves a significant increase in performance over pure polyethylene even at 1 cm thickness.

The same behavior is consistent across other mineral candidates as can be seen from Table 3 for 5 cm thickness. Amongst the three tested candidates, Epoxy/Colemanite showed the best performance.

Table 3. The percentage of stopped neutrons compared for different minerals in the epoxy composite in addition to layered setups with HDPE for HE and LE beams at 5 cm thickness. Error bars < 0.1%.

Type of Composites	Material	Stopped Neutrons ($(I_0-I)/I_0$) [% ±0.1]	
		HE	LE
Epoxy Composites	E/Priceite	54.1	93.4
	E/Kernite	51.4	91.6
	E/Colemanite	57.7	95.0
HDPE + Composites	HDPE First + E/Colemanite	62.1	96.8
	HDPE Last + E/Colemanite	56.1	93.6

A compound shield setup was proposed involving two layers totaling 5 cm in thickness, the first of which is a 2.5 cm polyethylene sheet, and the latter is a 2.5 cm composite sheet to harness the effectiveness of the materials at low energies. The aim is to use the polyethylene for slowing down the fast neutrons before they reach the epoxy/boron composite. The beam was set to hit the pure polyethylene sheet first, and again to hit the composite sheet first to test this hypothesis. Results, presented in Table 3, show a significant advantage to placing polyethylene before the borated composite. The combined assembly achieves a higher performance than a single layer polyethylene or the composite of the same total thickness.

3.3. Activation

Depending on the nuclei present in the shielding material and their concentrations, radioactive isotopes may be formed as the material is exposed to neutron radiation. The proposed materials were tested for production of radioactive isotopes in MC simulations for neutrons < 20 MeV. Since Colemanite and Priceite are comprised from the same elements with different compositions, they have similar activation properties. The most prominent radioisotopes for Colemanite and Priceite after neutron irradiation are B^{12}, N^{16} and Li^{8}. These isotopes have relatively short half-lives (max 7.2 s for N^{16}) and would quickly cool down after the irradiation is stopped. Other isotopes with half-lives in the order of days are also produced such as (Ca^{47}, Ca^{45}, Sc^{47}, K^{44}), but these isotopes are produced with much lower rates (5 orders of magnitude). This could eventually limit the

lifetime these materials can be used depending of the neutron flux and the amount of shielding used. In the same manner, the sodium in Kernite generates radioactive isotope such as (Na^{24}, Ne^{23}, Mg^{23}, Na^{22}) which have half-lives that are marginally shorter than Colemanite and Priceite. Making it slightly better suited for high flux and long exposure scenarios.

4. CONCLUSION

Different boron containing materials have been studied through MC analysis using Geant4 and MCNP6. Borated HDPE and different epoxy/boron composites were tested for their neutron shielding performance and compared to each other at different energy regimes. Effects of thicknesses and ordering of multi-layered shields were also investigated. The optimal concentrations for borated polyethylene shields were found at 5 wt.%. The slowdown behaviour of neutrons was also tested as a function of incident neutron energy. The multi-layered shield of HDPE with the Epoxy/Colemanite composite has been shown to have superior shielding characteristics among the tested materials, along with its better availability and affordability.

SIMILARTY RATE: 7%

ACKNOWLEDGEMENT

The work was supported by grants from TUBITAK (5190039).

REFERENCES

[1] J.W. Shin, J.W. Lee, S. Yu, B.K., Beak J.P. Hong, Y. Seo, W.N. Kim, S.M. Hong, C.M. Koo, “Polyethylene/boron-containing composites for radiation shielding”, *Thermochimica Acta*, vol. 585, pp. 5-9, 10 June 2014. https://doi.org/10.1016/j.tca.2014.03.039.

[2] S. T. Abdulrahman, Z. Ahmad, S. Thomas, A. A. Rahman, “Chapter 1-Introduction to neutron-shielding materials,” in Micro and Nanostructured Composite Materials for Neutron Shielding Applications, Woodhead Publishing Series in Composites Science and Engineering, pp. 1–23, 2020.

[3] International Atomic Energy Agency, “NGATLAS: Atlas of Neutron Capture Cross Sections,” March 2014.

[4] J.C. Sublet, A.J. Koning, D. Rochman, M. Fleming, M. Gilbert, “Delivering Both Completeness and Robustness”, In Advances in Nuclear Nonproliferation Technology and Policy Conference, Santa Fe, NM, USA. Sept. 25-30, 2015.

[5] Ş.G. İrim, A.A. Wis, M.A. Kestin, O. Baykara, G. Ozkoc, A. Avcı, M. Doğru, M. Karakoç, “Physical, mechanical and neutron shielding properties of h-BN/Gd2O3/HDPE ternary nanocomposites”, *Radiation Physics and Chemistry*. Vol. (144), pp. 434-443. March 2018. https://doi.org/10.1016/j.radphyschem.2017.10.007.

[6] CERN, "Geant4 User's Guide for Application Developers," 2016.

[7] X. Campo, R. Méndez, M.A.S. Lacerda, D. Garrido, M. Embid, J. Sanz, “Experimental evaluation of neutron shielding materials”, *Radiation protection dosimetry*. Vol. 180, no. (1-4), pp. 382-385. 1-4-August 2018. https://doi.org/10.1093/rpd/ncx202.

[8] X. Zhang, M. Yang, X. Zhang, H. Wu, S. Guo, Y. Wang, “Enhancing the neutron shielding ability of polyethylene composites with an alternating multi-layered structure”, *Composites Science and Technology*, vol. 150, pp. 16-23, 29 September 2017. https://doi.org/10.1016/j.compscitech.2017.06.007.

[9] K. Okuno, “Neutron shielding material based on colemanite and epoxy resin”, *Radiation Protection Dosimetry*, vol. 115, no. 258-261, 20 December 2005. https://doi.org/10.1093/rpd/nci154.

[10] F. Demir, A. Un, “Radiation Transmission of Colemanite, Tincalconite and Ulexite For 6 And 18 MV X-Rays By Using Linear Accelerator”, *Applied Radiation and Isotopes*, vol. 72, pp. 1-5, February 2013. https://doi.org/10.1016/j.apradiso.2012.09.020.

[11] T. Korkut, A. Karabulut, G. Budak, B. Aygün, O. Gencel, A. Hançerlioğları, “Investigation Of Neutron Shielding Properties Depending On Number Of Boron Atoms For Colemanite, Ulexite And Tincal Ores By Experiments And FLUKA Monte Carlo Simulations”, *Applied Radiation and Isotopes*, vol. 70 no. (1), pp. 341-345, January 2012.

[12] H. Binici, O. Aksogan, A.H Sevinc, A. Kucukonder, “Mechanical and Radioactivity Shielding Performances Of Mortars Made With Colemanite, Barite, Ground Basaltic Pumice And Ground Blast Furnace Slag”, *Construction and Building Materials*, vol. 50, pp. 177-183, 2014. https://doi.org/10.1016/j.conbuildmat.2013.09.033.

[13] G. Cosansu, C. Cogun, "An İnvestigation On Use Of Colemanite Powder As Abrasive İn Abrasive Waterjet Cutting (AWJC)", *Journal Of Mechanical Science And Technology* vol. 26, no. 8, pp. 2371-2380. DOI 10.1007/s12206-012-0619-9, 2012.

[14] C. Kaynak, N.A. Isitman, "Synergistic Fire Retardancy of Colemanite, A Natural Hydrated Calcium Borate, ın High-İmpact Polystyrene Containing Brominated Epoxy and Antimony Oxide", Polymer *Degradation and Stability* vol.96, no.5, pp.798-807, May 2011. https://doi.org/10.1016/j.polymdegradstab.2011.02.011.

[15] N.A. Isitman, C. Kaynak, "Effect of Partial Substitution Of Aluminum Hydroxide With Colemanite İn Fire Retarded Low-Density Polyethylene", *Journal of Fire Sciences* vol. 31, no. 1, pp. 73-84, August 2 2013. https://doi.org/10.1177/0734904112454835.

[16] R. Bagheri, S.P. Shirmardi, R. Adeli, "Study on Gamma-Ray Shielding Characteristics Of Lead Oxide, Barite, And Boron Ores Using MCNP-4C Monte Carlo Code And Experimental Data", *Journal of Testing and Evaluation* vol. 45, no. 6, pp. 2259-2266, 24 January 2017. DOI: 10.1520/JTE20160284.

[17] K. Okuno, M. Kawai, H. Yamada, "Development Of Novel Neutron Shielding Concrete", Nuclear Technology vol. 168 no. 2, pp. 545-552, 10 Apr 2009. https://doi.org/10.13182/NT09-A9241.

[18] J. Kim, B.C. Lee, Y.V. Uhm, W. H. Miller, "Enhancement of Thermal Neutron Attenuation of Nano-B4C-BN Dispersed Neutron Shielding Polymer Nanocomposites", *Journal of Nuclear Materials* vol. 453 no. 1-3, pp. 48-53, October 2014.

[19] T. Özdemir, A. Güngör, A.İ. Reyhancan, "Flexible Neutron Shielding Composite Material of EPDM Rubber With Boron Trioxide: Mechanical, Thermal Investigations And Neutron Shielding Tests", *Radiation Physics and Chemistry* vol. 131, pp. 7-12, February 2017. https://doi.org/10.1016/j.radphyschem.2016.10.012.

[20] A.S. Kipcak, P. Gurses, E.M. Derun, N. Tugrul, S. Piskin, "Characterization of Boron Carbide Particles And İts Shielding Behavior Against Neutron Radiation", *Energy conversion and management* vol. 72, pp. 39-44, August 2013. https://doi.org/10.1016/j.enconman.2012.08.026.

Eurasian Journal of Science Engineering and Technology

Research

GURSON-TVERGAARD-NEEDLEMAN (GTN) PARAMETERS OF DP STEELS WITH DIFFERENT ROLLING DIRECTIONS WERE DETERMINED AND INVESTIGATED AT DIFFERENT STRAIN RATES

Labinot TOPILLA[1,*], Serkan TOROS[2]

[1,2] *Nigde Omer Halisdemir University, Mechanical Engineering Department, 51245, Nigde, Türkiye*

ABSTRACT

Dual Phase steels are high-strength and well-formability steels, which are widely used in the automobile industry. However, based on their microstructural observations, the shapes, orientations, and directions of the grains of these two steels are different and vary depending on the degree of observation. Therefore, the objective of this research was to compare the stress and strain distribution at different strain rates of standard specimens and cut at different rolling directions of DP steels, namely DP600 and DP800 steels. Besides, in this study, the finite element modeling method is used through optimization to determine the GTN fracture failure, constitutive and nucleation parameters of the mentioned steels based on their rolling directions and strain rates. The experimental and numerical simulation results are also compared, and they are in good agreement.

Keywords: DP steels. Experimental, Optimizations, Simulations, GTN parameters.

1. INTRODUCTION

It is important to investigate high-strength and well formability steels to advance fuel efficiency, environmental protection, and vehicle safety from accidents. Strength and strain ability are characterized by a microstructure consisting of a strength martensitic phase distribution in a soft ferritic phase, which is developed in the late 1970s The term "Dual-Phase" refers to the presence of ferritic and martensitic microstructures composed of small amounts of bainite, perlite, and austenite [1]. And which are widely used in the automotive industry [2], [3] A favorable combination of strength and ductility can be obtained by developing a dual-phase or multi-phase microstructure in steel. The soft phase of steel, ferrite, has a body-centered cubic (BCC) crystal structure and can contain only a few hundredths of a percent carbon, according to [4]. The ferrite phase is the primary phase in the low range, while martensite is the generic term for microstructures formed by diffusion-free phase transformations. When the steel is annealed in the inter-critical range, it converts to austenite and ferrite, which form an FCC or BCC crystal structure. There are two basic forms of martensite structures, lath martensite, and slab martensite. While the reinforcing effect on DP structures is realized by adding martensite to the matrix ferrite. After that, the DP steels can be tensiled using conventional tools while maintaining their properties. For example, the tensile stress for DP600 steel can be increased by approximately 20% compared to micro-alloy steel (HSLA) with the same thickness. [5].

On the other hand, many finite element models determine the behavior of the material under stress-strain conditions, and so the purpose of our research was to determine the GTN parameters through finite element modeling. (MAT_GURSON_120). In addition, in 1977, Gurson proposed a yield surface based on the growth of spherical voids. This model is commonly used to describe the evolution of micromechanical damage in ductile materials. Seven years later, in 1984, Tvergaard and Needleman modified the Gurson model by introducing two additional material parameters (q1 and q2), [6]. So that the model could detect the phenomenon of cavity coalescence and the corresponding sudden loss of strength [7], since a ductile material is assumed to be porous. So, the Gurson damage model is a single-stage void model that considers the influence of void expansion on the material's plastic behaviour [8]. It is important to note that it has been recognized in recent years that the Gurson-type damage models are unable to model ductile fracture under shear dominated stress states with low-stress triaxiality [9]. There are some main parameters of the GTN damage model for a detailed analysis of the material behavior and a good understanding of the damage: the effective work-hardening parameters; the nucleation parameters; the initial porosity parameter; the yield loci parameters; and the failure parameters [10]. The modified Gurson-Tvergaard-Needleman (GTN) model is widely used in the modelling of ductile fracture [11]. As a result, this model has been adapted in many finite element programs, and it is a micromechanical damage model in which defects are assumed to exist in the materials, forming global spheres [12]. In the case of determining the GTN model parameters, the deformation curve of the stress unit, which was obtained from an experimentally used uniaxial tensile test, is required. Model parameters can be determined by adjusting the results of the finite element model, which is created by taking into account the boundary conditions of the relevant experiment. In the case of the forming process a slight deformation could be observed after the constriction, so that a break could occur even before the deformation si localized.

* Corresponding author, e-mail: labino.topilla@gmail.com (L. Topilla)
Recieved: 07.05.2022 Accepted: 18.07.2022
doi: 10.55696/ejset.1113577

Crack initiation can occur in dual-phase steel before constriction and there is a tendency for a macro crack to occur in an early state [13]. The damage curve explains the relationship between the stress triaxiality and the equivalent plastic strains [14]. Nowadays, a valuable contribution is being made by the computer field, through which it is attempted to give a continuous contribution to the knowledge of the behavior of metals during the process of deformation and failure. One of the software applications to research the behavior of materials, in general, is LS-DYNA. However, there are many models in some integrated software that mainly determine the failure and cracking of materials. The Gurson – Tvergaard – Needleman (GTN) damage model, micromechanics damage modeling (MDM), and continuum damage mechanics (CDM) are a few examples, according to [15].

Based on the literature review, no case is found where the optimization is done with finite element methods by LS-OPT, in terms of determining Gurson parameters, such as effective performance hardening parameters, nucleation parameters, initial porosity parameter, yield location parameters, and failure parameters. Therefore, by researching and considering the properties of DP600 and DP800 steels, this study aimed to contribute to the sheet metal forming industry, through describing the process of optimizations realized in LS-OPT, to determine the GTN parameters, specifically the fracture failure, the constitutive and the nucleation parameters for the mentioned steel. Morover, the aim was to determine the parameters in terms of elongation by using standard specimens resulting from different rolling directions. and tested at different strain rates, because there appear to be changes in strain, see Tables 3 and 5. Because the microstructure of Dual Phases steel is known to be mostly composed of the ferrite phase, which offers ductility, and the martensite phase, which provides strength. However, the shapes, orientations, and directions of the grains of these two phases are different and vary depending on the degree of observation. Finally, based on our research done in the literature, so far we have not found any research similarities with our research goals.

2. MATERIAL AND METHOD

2.1 Experimental procedure

In the following Figures 1, and 2, are presented the comparisons between experimental results of DP600, and DP800 steels, cut at 0°, 45°, and 90° degrees of rolling directions (RD). The specimens were based on the ASTM E8 standard, and with average properties equipped with a 50 mm gauge length, a nominal thickness of 0.78 mm, and a width of 12.5 mm. Where the preformation of the experimental, uniaxial tensile test was done at room temperature and at strain rates 0.0083 s^{-1}, 0.042 s^{-1}, and 0.16 s^{-1}. In the mentioned figures, the graphical representation of mechanical properties is presented. And the curves are realized based on the general engineering stress-strain equation. Figure 1 shows graphical comparisons of engineering stress-strain curves of DP600 steel cut at 0°, 45°, and 90° degrees (RD) and tested at three different strain rates. While In Figure 2. (a, b, and c) are the graphical comparison representations of engineering stress-strain curves of DP800 steel, cut at 0°, 45°, and 90° degrees (RD), and tested at three different strain rates too. While their differences are expressed in tabular form in terms of elongations, they are presented in Tables 3 and 5.

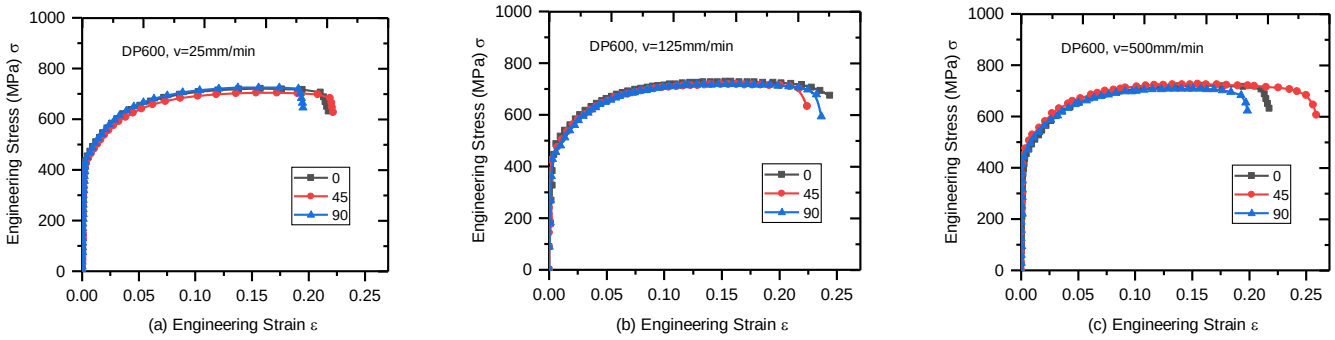

Figure 1 Comparison of force displacement results of DP600 steel as a result of different rolling directions and different strain rate

GURSON-TVERGAARD-NEEDLEMAN (GTN) PARAMETERS OF DP STEELS WITH DIFFERENT ROLLING DIRECTIONS WERE DETERMINED AND INVESTIGATED AT DIFFERENT STRAIN RATES

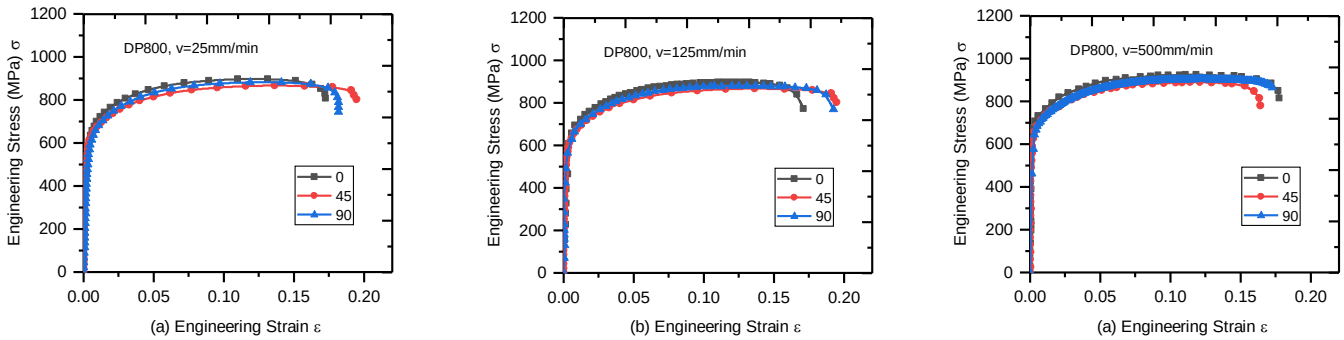

Figure 2. Comparison of force displacement results of DP800 steel as a result of different rolling directions and different strain rate

The microstructure of DP600 and DP800 steels based on microscopic observation is shown in Figures 3 and 4. The aim was to give a visual view of the orientation of the grains seen from a different angle of rolling direction (RD). Figures 3. (a) and 4. (a) show the view of the microstructure when viewed from an angle of 0° of RD, whereas Figures 3. (b) and 4. (b) shows the view of the microstructure when viewed from an angle of 45° of RD. In figures 3. (c) and 4. (c), microstructure images are presented when viewed from an angle of 90° of RD. The martensite phase is shown in black, while the ferrite phase is shown in yellow.

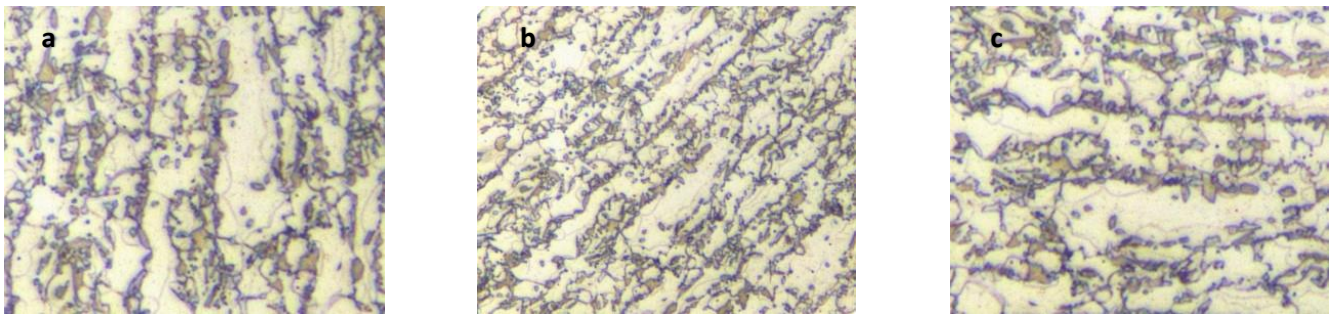

Figure 3. Microstructure observation of DP600 steel from different rolling directions

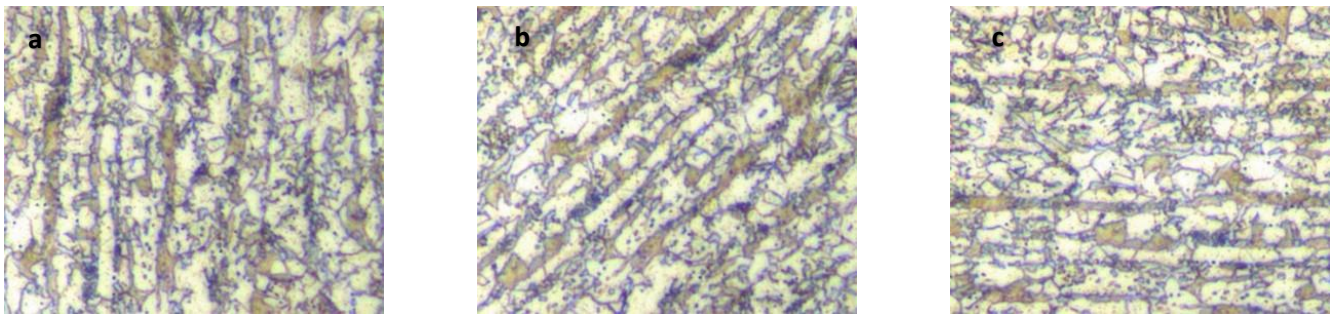

Figure 4. Microstructure observation of DP800 steel from different rolling directions.

2.2 Numerical modeling of ductile damage Gurson_120_Mat_Model

This model, which has been adapted into most finite element software, is basically a micromechanical damage model that assumes that defects are already present in materials and that these defects form spherical voids. Standard uniaxial tensile testing, microstructural characterization, and finite element modeling were used to assess the continuity of damage behavior investigations in the DP600 and DP800 steels investigated by [18] on the void analysis and experimental data of the uniaxial

traction test, and the determination of the damage parameters of the Gurson-Tvergaard-Needleman (GTN) damage model. As a result, a good agreement is reached between the predictions and the experimental load elongation, allowing the identification of the complete set of parameters of the GTN damage model of the DP600 and DP800 steels. According to [16] which emphasize that physical approach that introduces a damage model coupled with the behavior of porous materials was the Gurson theory.

$$\Phi = \left(\frac{q}{\sigma_0}\right)^2 + 2f\cosh\left(-\frac{3p}{2\sigma_0}\right) - 1 - f^2 = 0 \quad (1)$$

where σ_0 is the flow stress of the material, f represents the voids volume fraction of the material, $q = \sqrt{(3/2)}\, s{:}s$ is the von Mises equivalent stress with s is the deviatoric part of the stress tensor and $p = -trace(\sigma)/3$ is the hydrostatic stress. The original Gurson model was later modified by Tvergaard and Needleman and started to be referred to as the GTN criterion. During the determination of the GTN model parameters, the stress strain curve obtained from an experimentally applied tensile test is needed. The model parameters can be determined by adapting the results obtained from the finite element model created by considering the boundary conditions of the relevant experiment to the experimental results. The formulations related to the GTN model are given below. The Gurson flow function is defined as:

$$\Phi = \frac{\sigma_M^2}{\sigma_y^2} + 2q_1 f^* \cosh\left(\frac{3q_2\sigma_H}{2\sigma_y}\right) - 1 - (q_1 f^*)^2 = 0 \quad (2)$$

The *q1* and *q2* parameters in Equation 3 were added to the model by Tvergaard and are two important parameters for improving the model prediction performance. With the expression *f* in the model, it shows the amount of defects in the material and is determined as follows.

$$f^*(f) = \begin{cases} f & f \le f_c \\ f_c + \frac{1/q_1 - f_c}{f_F - f_c}(f - f_c) & f > f_c \end{cases} \quad (3)$$

While the defect rate is taken until the defects that occur with the deformation in the material reach a certain level, the calculations in the 2nd step are made if it exceeds the critical value. However, according to the studies of Gurson Tvergaard and Needieman, and Nahshon and Hutchiston, the increase in voids in the material internal structure can be expressed by Equation 4-7. The growth of the void volume fraction is defined as

$$\dot{f} = \dot{f_G} + \dot{f_N} \quad (4)$$

where the growth of existing voids is defined as

$$\dot{f_G} = (1 + f)\ \dot{\varepsilon}_{kk}^p \quad (5)$$

and the nucleation of new voids is defined as

$$\dot{f_N} = A\dot{\varepsilon}_p, \quad \text{Where} \quad (6)$$

$$A = \frac{f_N}{S_N\sqrt{2\pi}} exp\left(-\frac{1}{2}\left(\frac{\varepsilon_p - \varepsilon_N}{S_N}\right)^2\right) \quad (7)$$

The *fo, fN, fc and ff* values in the given models should be determined and introduced to the programs.

2.3 Finite Element Modeling For Gurson Model

The solid element was used for MAT_GURSON_120 MODEL during the construction of kye cards to perform numerical optimizations and simulations. It is understood that all the properties of the mechanical data placed on the key cards are similar to the experimental data, including similarity to geometric shapes of specimens, size, thickness, width, time duration, and even strain rate, applied to perform uniaxial tensile testing. Along with the GTN parameters: ε_N, f_c, f_f, f_N ,q_1 ,q_2, S_N, mechanical properties such as density (p = 7.830e-06), Young module (E = 216), and Poisson ratio (v = 0.28) are included in the key cards. While at load curve ID: LCSS =, each specimen was given its own experimental Hollomon's curve. Nevertheless, regarding this model, [10] have contributed to explaining the GTN parameters. Figure 5. will show the mash and the geometric shapes of the used specimens.

Figure 5. The finite element mesh of the ASTEM E8 uniaxial tensile test specimen

2.4 Theory of optimization

Optimization can be defined as a procedure for "achieving the best outcome of a given operation while satisfying certain restrictions." This objective has always been central to the design process but is now assuming greater significance than ever because of the maturity of the mathematical and computational tools available for design. Solving the optimization problem requires an optimization algorithm. The two basic optimization branches employed in LS-OPT are metamodel-based optimization and direct optimization [17]. The optimizations of Gurson parameters were realized in the application software LS-OPT (metamodel-based optimization). For the mentioned model, a total of 18 specimens were optimized separately, one by one, followed by a 10 x 10 itineration. In the LS-OPT software are placed all the necessary mechanical and geometric dates, which are similar to the experimental results and key cards. While, in the setup, the parameters for the optimizations expressed at the starting, minimum, and maximum are set. See tables 1–2. As all investigated cases result in different parameters as mentioned [6] the choice of different tests could result in different parameter values for the modified Gurson model. See the optimization process in Figure 6.

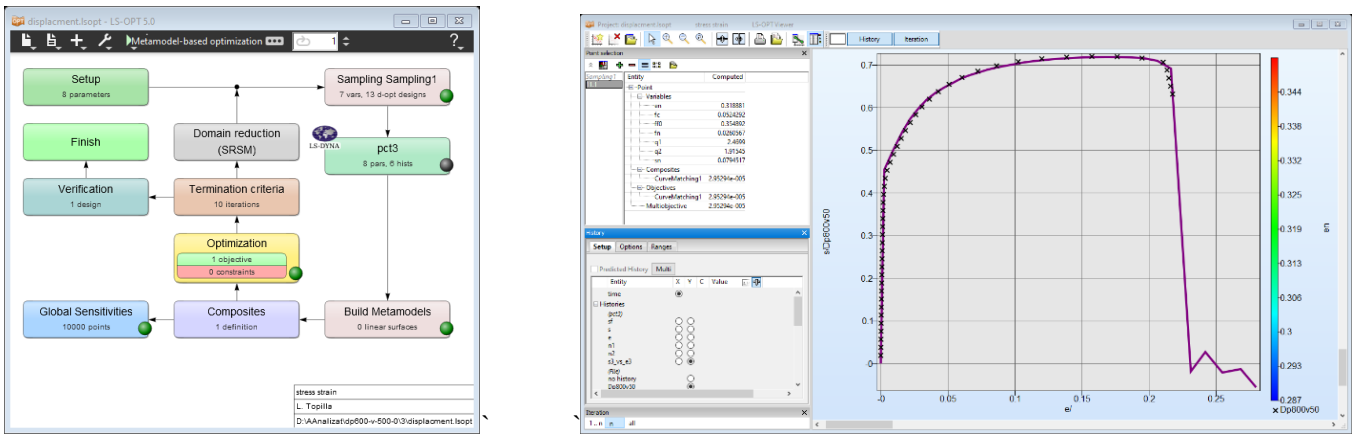

Figure 6. LS-OPT optimization figurative process in Figure 6

3 RESULTS AND DISCUSSION

3.1 Results and Discussion of GTN parameters

Parameters ε_N, $and\ S_N$ usually have their standard values from 0.1 up to 0.3, and mostly for DP steels. Therefore, these are thought of as statistical constants of nucleation and not as internal proportions of materials [11]. So, S_N, is the standard deviation, f_N is the volume fraction of particles, and during the material deformation process, the f_N stands for volume fraction when voids nucleate. And the meaning of ε_N, value is the strain when void nucleation happens. The influence of value ε_N, is interrelated with the influence of [11]. While in our case, the aforementioned materials are used as working parameters ε_N, S_N, $and\ f_N$ during the optimization process, the starting parameters for DP800 steels were defined as $\varepsilon_N, = 0.065 - 0.085$: and the maximum variates ranged from: 0.27-32. It is important to note that this was a key parameter that had a large impact on defining the curve fitting. While S_N the starting parameters were set to be: 0.05–0.1, the maximum was set to: $S_N = 0.25 - 0.3$. The following are the starting parameters: $f_N = 0.01$ and the maximum is given by: $f_N = 0.05$. Where's for DP600 steels, for parameter ε_N starting were defined to be: $\varepsilon_N, = 0.06 - 0.09$ and the maximum variations range from 0.27 to 35. In terms of S_N parameters, the minimum was set to 0.03 and the maximum was set to: $S_N = 0.25 - 0.3$. For f_N parameter the starting point was defined as: $f_N = 0.0104$ and the maximum as: $f_N = 0.05$. Tables 1–2 show the results.

Table 1. Exhibit optimisation parameters prediction of GTN of DP600 steels.

Specimens	Parameter	ε_N	f_c	f_f	f_N	q_1	q_2	S_N
DP600, 0° 0.00833 s^{-1}	Starting	0.06	0.016	0.22	0.0104	1.84	0.8	0.28
	Minimum	0.01	0.002	0.001	0.003	0.45	0.3	0.03
	Maximum	0.30	0.052	0.62	0.05	2.5	2.21	0.25
	Results	0.2816	0.002	0.3704	0.0171	2.1981	1.9287	0.0438
DP600, 0° 0.042 s^{-1}	Starting	0.09	0.013	0.25	0.0104	1.86	0.8	0.03
	Minimum	0.01	0.002	0.001	0.003	0.45	0.3	0.013
	Maximum	0.34	0.53	0.61	0.05	2.5	2.2	0.25
	Results	0.0138	0.3955	0.5505	0.0199	1.9922	1.3056	0.2019
DP600, 0° 0.16 s^{-1}	Starting	0.09	0.012	0.21	0.0104	1.86	0.8	0.03
	Minimum	0.01	0.002	0.001	0.003	0.45	0.3	0.013
	Maximum	0.35	0.50	0.63	0.05	2.5	2.2	0.25
	Results	0.3188	0.0524	0.3540	0.0260	2.4699	1.9154	0.0794

Table 2. Exhibit optimisation parameters prediction of GTN of DP800 steel.

Specimens	Parameter	ε_N	f_c	f_f	f_N	q_1	q_2	S_N
DP800, 90° 0.00833 s^{-1}	Starting	0.065	0.0091	0.17	0.01	1.7	0.8	0.1
	Minimum	0.05	0.001	0.003	0.003	0.45	0.3	0.033
	Maximum	0.27	0.7	0.8	0.05	2.5	1.8	0.25
	Results	0.2614	0.0020	0.3274	0.0430	1.0966	1.0715	0.0660
DP800, 45° 0.042 s^{-1}	Starting	0.085	0.0057	0.16	0.01	1.5	0.8	0.1
	Minimum	0.05	0.002	0.001	0.003	0.45	0.3	0.033
	Maximum	0.28	0.65	0.84	0.05	2.5	1.8	0.25
	Results	0.2230	0.1722	0.1926	0.0324	1.6605	1.5819	0.0653
DP800, 0° 0.16 s^{-1}	Starting	0.085	0.0058	0.17	0.01	1.7	0.8	0.05
	Minimum	0.01	0.002	0.001	0.003	0.45	0.3	0.033
	Maximum	0.28	0.73	0.7	0.05	2.5	1.8	0.25
	Results	0.2636	0.4370	0.4572	0.0206	2.2835	1.8	0.033

3.3 Constitutive parameters

The constitutive parameters introduced by Tvergaard and Needleman (q_1- q_3) [18] or the yield locus parameters [10], usually thought to be fixed: $q_1 = 1.5$, $q_2 = 2$, $q_3 = q_1^2$ [19]. However, by optimizing DP00 and DP800 steels with their tested properties, These q_1 *and* q_2 parameters are being used in each case, So, for DP800 steel, the starting point was set to q_1 = 1.7 and the maximum was set to q_1 =2.5. As for q_2 the starting point was set to be $q_2 = 0.8$, and the maximum range was set to 1.8-2.2. While, for DP600 steel q_1 starting were defined to be: $q_1 = 1.86$ and the maximum were given by: 2.5, as for q_2 starting were defined to be: $q_2 = 0.8$ and the maximum were given to be: 2.2.

3.4 Failure Parameters

The porosities, f_c and f_f are considered material parameters and there are several methods to determine them, especially the critical void volume fraction, which is the failure parameter f_c, and corresponds to the onset of void coalescence. Also f_c can be numerically obtained by fitting the numerical curve with the experimental one [11]. But in the respective study, the determination of the critical void volume fraction f_c is obtained from the plastic strain corresponding to the ultimate yield strength[10], Because when the deformation reaches this point, then it starts to take the form of plastic deformation as the pores begin to settle and the whole coalescence is created. While the failure parameter (the final void volume fraction) f_f is obtained from the plastic deformation at the moment of falling, at the cross-sectional area, when the curve downwards or when the stress loses its carrying ability completely. In this diagram Figure 7 are presented the targeting of f_c and f_f parameters for optimization

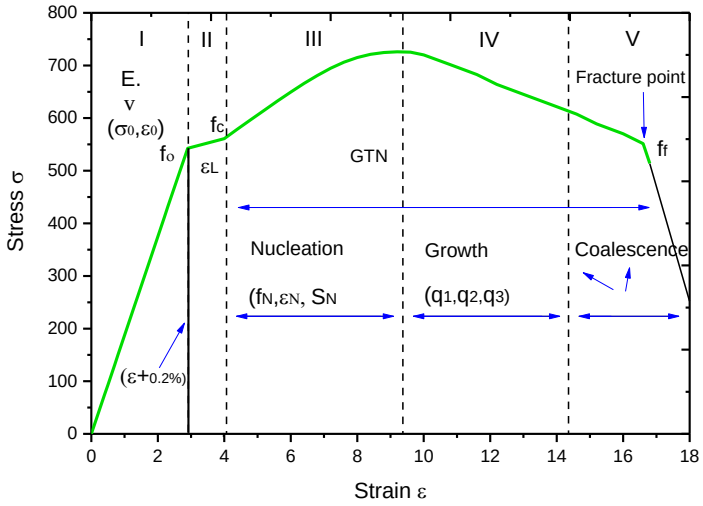

Figure 7. The graphic explanation of defining the GTN model parameters can be subdivided into three subsets.

3.5 Comparison between the model predictions and experimental results of DP600 steel, ε_r = 0.0083 s^{-1}, at different rolling directions (RD)

The comparison of the experimental and numerical simulation results obtained from the d3plot file generated after the optimizations are shown in the following figures. The compared properties are listed above in Table 3, while the GTN parameters are shown in Table 4. Figures 8, 9. and 10 show the comparisons between experimental and numerical curves and the mechanical properties of standard specimens of DP600 steel cut at 0°, 45° and 90° to the rolling direction (RD). The experimental and numerically simulated uniaxial tensile tests were performed at a strain rate of ε_r = 0.0083 s^{-1} for all specimens studied. These curve comparisons agree well with the results of [14] for all tests in terms of fracture displacement. As a result, the graphical comparisons of mechanical properties are based on the general stress-strain equation and are shown in Figures 8, 9, and 10. (a) depicts the graphical comparisons of engineering stress-strain curves. Figures 8, 9. and 10, (b) show the graphical comparisons of the true stress-strain curves, and Figures 8, 9. and 10, (c) show the graphical comparisons of the Hollomon plastic deformation flow curve.

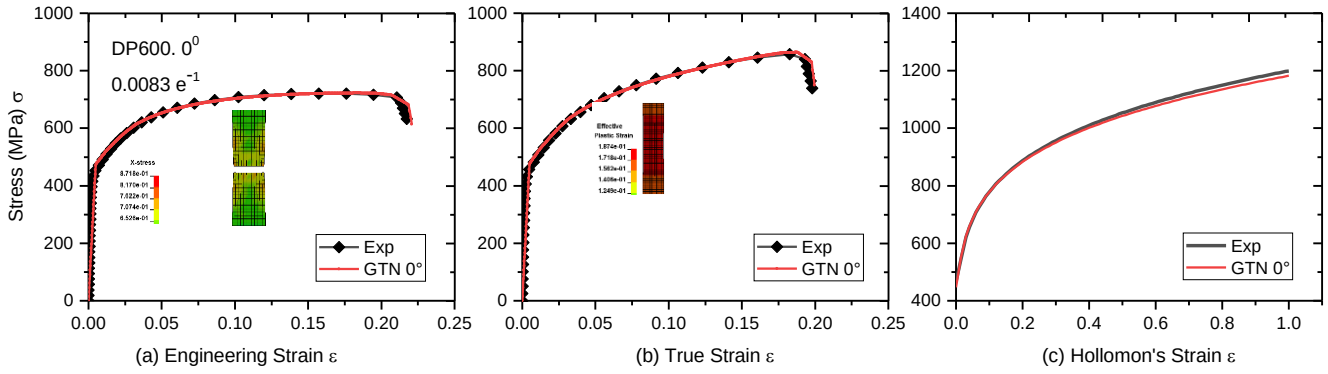

Figure 8. Compariosns between experimental and numerical simulation results of DP600 steel, RD = 0°, ε_r = 0.0083 s^{-1}, (a) σ_{eng}, (b) σ_{true}, (c) Hollomon curve

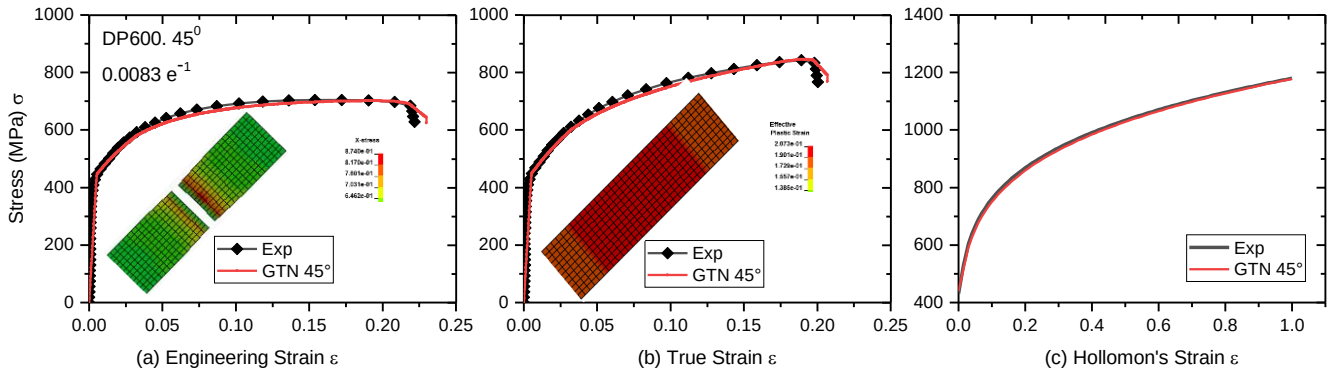

Figure 9. Compariosns between experimental and numerical simulation results of DP600 steel, RD = 45°, $\boldsymbol{\varepsilon_r}$ = 0.0083 s^{-1}, (a) $\boldsymbol{\sigma_{eng}}$, (b) $\boldsymbol{\sigma_{true}}$, (c) Hollomon curve

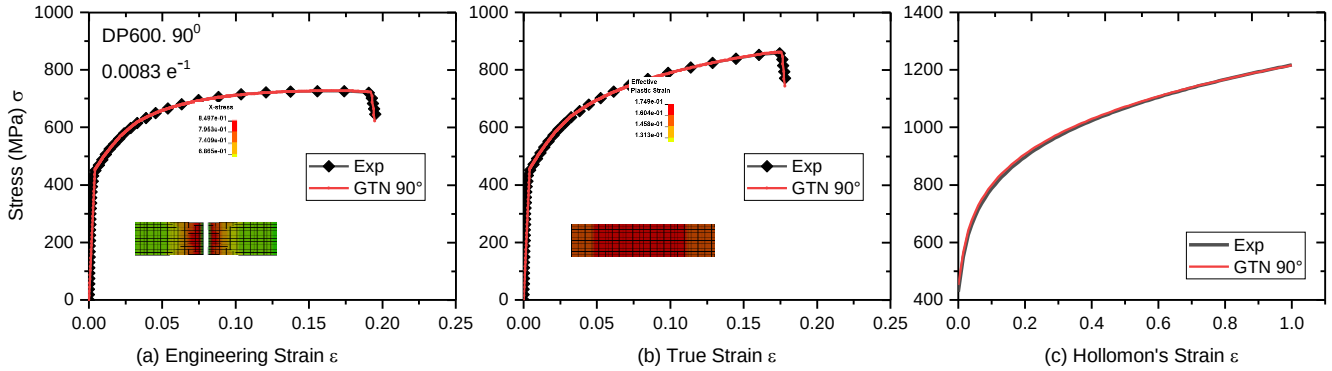

Figure 10. Compariosns between experimental and numerical simulation results of DP600 steel, RD = 90°, $\boldsymbol{\varepsilon_r}$ = 0.0083 s^{-1}, (a) $\boldsymbol{\sigma_{eng}}$, (b) $\boldsymbol{\sigma_{true}}$, (c) Hollomon curve

In this section, relative errors (RE) between experimental results and numerical simulation results for DP600 steel with different rolling directions (RD) and tested at a strain rate $(\varepsilon_r)\ of,\ \varepsilon_r$ = 0.0083 s^{-1}, a are presented. Comparisons were made for all specimens tested, with particular emphasis on engineering fracture strain. (ε_{eng_f}), true fractures strain (ε_{true_f}), and Hollomon ultimate tensile strength (σ_H), Hence, in Figure 8, are presented relative errors (RE) calculations of DP600 steel, RD = 0°. And from the numerical calculation of the RE that was done for the engineering fracture strain (ε_{eng_f}) this is the result of RE = 1.05%, whereas, for the true fractures strain (ε_{true_f}) this is the result of RE = 1.01%, and regarding Hollomon flow curve (σ_H) this is the result of RE = 1.44%. Whereas, Figure 9 presents RE calculations for the same steel, but with a different RD = 45°. And from the mathematical calculation of the difference that has been done for the engineering fracture strain (ε_{eng_f}) this is the result of RE = 3.10%, while, for the true fractures strain (ε_{true_f}) this is the result of RE = 2.9%, and for Hollomon flow curve (σ_H) this is the result of RE = 1.17%. Finally, Figure 10. presents RE calculations for the mentioned steel, also with a different RD = 90°. And from the mathematical calculations of the RE that were done for the engineering fracture strain (ε_{eng_f}) this is the result of RE = 0.05%, while for the true fractures strain (ε_{true_f}) this is the result of RE = 0.00%, and for Hollomon flow curve (σ_H) this is the result RE = 0.16%.

The mechanical properties of DP600 steel obtained from the experimental and numerical simulation results of true-stress-strain measures of specimens tested at three different rolling directions and three different strain rates are summarized in Table 3. These properties include true ultimate tensile strength (σ_u), Holloman's ultimate tensile strength(σ_H), and true fracture strain (ε_{true_f}) comparisons are similar [10]. While Figure 11 represents graphically the comparisons for true fracture strain.

Table 3. Comparisons between experimental and numerical simulation results of the mechanical properties of DP600 steel.

DP600		(σ_u) (Mpa)		Hollomon (σ_H) Mpa		Fracture (ε_{true_f})	
Specimens	Velocity	Exp	Sim	Exp	Sim	Exp	SIM
S - RD=0°	0.00833 s^{-1}	858	863	1199	1182	0.197	0.199
S - RD=45°		842	846	1179	1177	0.201	0.207
S - RD=90°		857	862	1217	1215	0.178	0.178
S - RD=0°	0.042 s^{-1}	873	866	1192	1173	0.22	0.221
S - RD=45°		859	855	1190	1159	0.2	0.211
S - RD=90°		858	867	1206	1193	0.21	0.213
S - RD=0°	0.16 s^{-1}	856	857	1164	1181	0.196	0.197
S - RD=45°		872	865	1149	1139	0.23	0.235
S - RD=90°		826	834	1155	1139	0.18	0.182

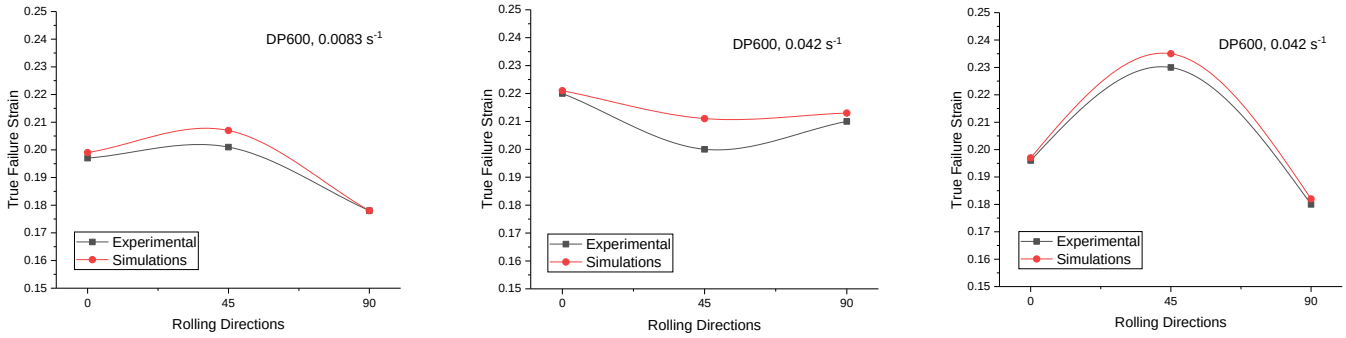

Figure 11. Experimental and simulation comparisons of DP600 steel as a result of different rolling directions and different strain rate.

The GTN parameters that are presented in table 4 are obtained from the optimization with special emphasis on the samples mentioned. All these final results have been leaked as a result of the optimization made in LS-OPT, separately for each specimen.

Table 4. Exhibit parameters prediction of GTN of DP600 steel.

Specimens	**GTN Parameters**	ε_N	f_c	f_f	f_N	q_1	q_2	S_N
DP600, 0°,	**0.00833 s^{-1}**	0.2816	0.002	0.3704	0.0171	2.1981	1.9287	0.0438
DP600, 45°,	**0.00833 s^{-1}**	0.2596	0.0037	0.1601	0.0119	2.2461	1.7898	0.0485
DP600, 90°,	**0.00833 s^{-1}**	0.1032	0.4010	0.0211	0.0212	1.8589	1.6026	0.1687
DP600, 0°,	**0.042 s^{-1}**	0.0138	0.3955	0.5505	0.0199	1.9922	1.3056	0.2019
DP600, 45°,	**0.042 s^{-1}**	0.2633	0.2917	0.1881	0.0224	1.9635	1.808	0.0212
DP600, 90°,	**0.042 s^{-1}**	0.29	0.2152	0.4143	0.0038	2.2369	2.2	0.0978
DP600, 0°,	**0.16 s^{-1}**	0.3188	0.0524	0.3540	0.0260	2.4699	1.9154	0.0794
DP600, 45°,	**0.16 s^{-1}**	0.35	0.1344	0.4597	0.0103	1.1613	1.9352	0.0158
DP600, 90°,	**0.16 s^{-1}**	0.1909	0.1062	0.4245	0.0135	2.3191	1.9536	0.0174

3.6 Comparison between the model predictions and experimental results of DP800 steel, ε_r= 0.0083 s^{-1}, at different rolling directions (RD)

In addition to the results obtained from the d3plot file simulation as a result of the optimization, the comparisons between the experimental results and the numerical simulation results are presented graphically. In terms of steel DP800, cut at RD 0°, 45°, and 90°, performing the uniaxial tensile test for both analyses with a strain rate of ε_r= 0.0083 s^{-1}. Those curve comparisons are in good agreement for all tests in terms of fracture displacement, with a difference of less than 1.5%, as shown in [6]. In

Table 5, the comparisons that belong to the mechanical properties are listed. Also in Table 6, the GTN parameters are listed for all the comparison specimens. In the following Figures 12.13, and 14, the comparisons between experimental and numerical simulation are shown graphically: Figures 12, 13 and 14 (a) show the graphical comparisons of the engineering stress-strain curves; Figures 12. 13 and 14. (b) show the graphical comparisons of the true stress-strain curves; and Figures 12. 13 and 14. (c) shows the graphical comparisons of Hollomon plastic deformation.

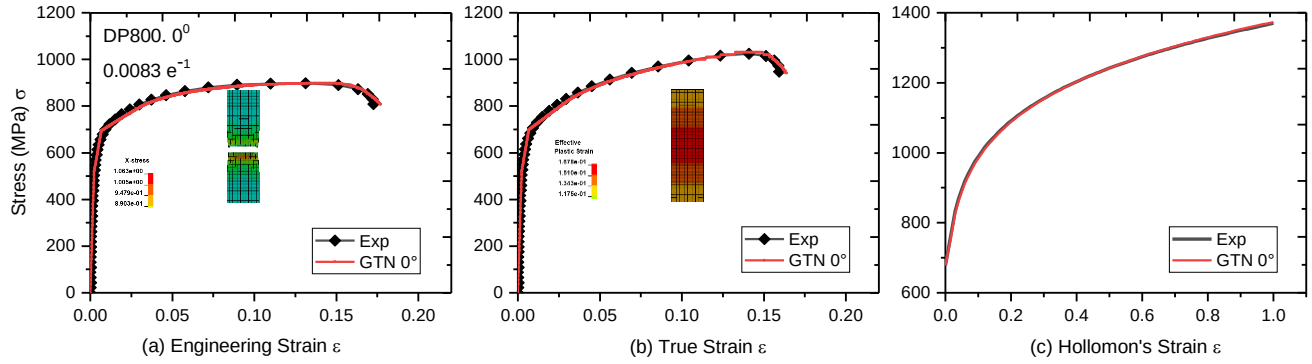

Figure 12. Compariosns between experimental and numerical simulation results of DP800 steel, RD = 0°, $\boldsymbol{\varepsilon_r}$= 0.0083 s^{-1}, (a) $\boldsymbol{\sigma_{eng}}$, (b) $\boldsymbol{\sigma_{true}}$, (c) Hollomon curve Ɛ

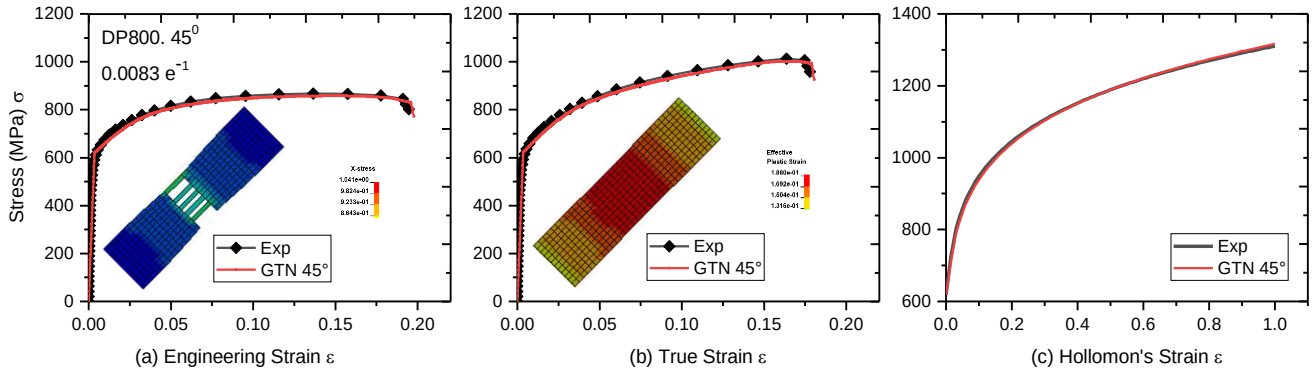

Figure 13. Compariosns between experimental and numerical simulation results of DP800 steel, RD = 45°, ε_r= 0.0083 s^{-1}, (a) σ_{eng}, (b) σ_{true}, (c) Hollomon curve

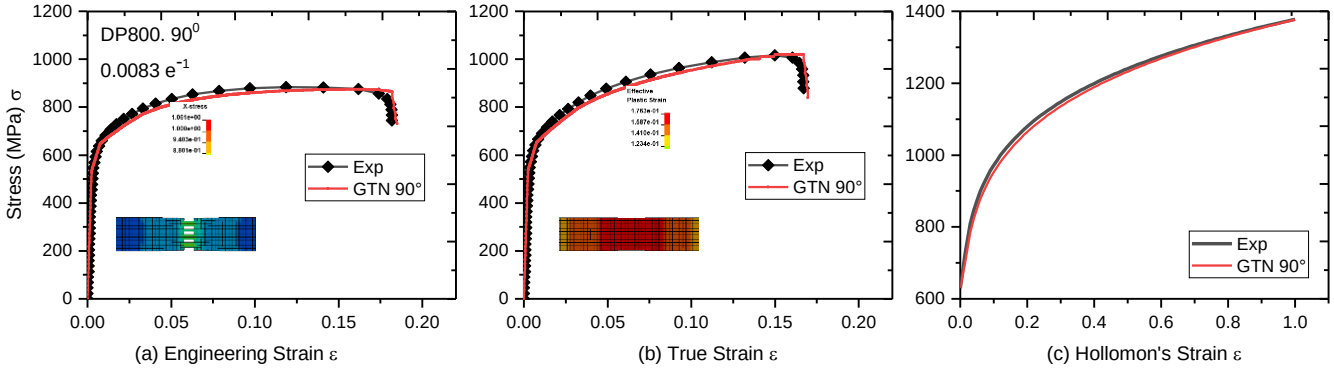

Figure 14. Compariosns between experimental and numerical simulation results of DP800 steel, RD = 90°, ε_r= 0.0083 s^{-11}, (a) σ_{eng}, (b) σ_{true}, (c) Hollomon curve

GURSON-TVERGAARD-NEEDLEMAN (GTN) PARAMETERS OF DP STEELS WITH DIFFERENT ROLLING DIRECTIONS WERE DETERMINED AND INVESTIGATED AT DIFFERENT STRAIN RATES

In this part, relative errors between experimental results and numerical results are for DP800 steel specimens with different rolling directions, tested at a strain rate (ε_r) of ε_r= 0.0083 s^{-1}. As well, comparisons were made for all specimens tested with particular emphasis of engineering fractures strain (ε_{eng_f}), true fractures strain (ε_{true_f}), and Hollomon ultimate tensile strength (σ_H). Similarly, Figure 12. represents relative errors in calculations of the mentioned steel, RD = 0°. Hence, the relative errors defined for engineering fracture strain is (ε_{eng_f}) is RE = 2.49%, for true fractures strain (ε_{true_f}) is RE = 2.45%, and for Hollomon flowe curve (σ_H) is RE = 0.29%. Figure 13 shows relative error calculations for the previously mentioned steels, but with varying RD = 45°. Where the relative errors defined regarding engineering fracture strain (ε_{eng_f}) is RE = 1.74%, true fracture strain (ε_{true_f}) is RE = 1.67%, and for Hollomon flowe curve (σ_H) is RE = 0.46%. Finally, Figure 14 shows relative error calculations for the same steel with a different RD = 90°. As a result, the engineering fracture strain defines the relative errors. (ε_{eng_f}) results is RE = 1.33%, and from true fractures strain (ε_{true_f}) results is RE = 1.18%, while from Hollomon flowe curve (σ_H) results RE = 0.15%.

Table 5 summarizes the mechanical parameters of DP800 steel derived from experimental and numerical simulations of true-stress-strain measures of specimens evaluated in three distinct rolling directions and three different strain rates. These properties include true ultimate tensile strength (σ_u), Holloman's ultimate tensile strength(σ_H), and true fracture strain (ε_{true_f}) comparisons are similar [10]. Figure 15 shows the comparisons for true fracture strain graphically.

Table 5. Comparisons between experimental and numerical simulation results of the mechanical properties of DP800 steel.

DP800		**(σ_u) (Mpa)**		**Hollomon (σ_H) (Mpa)**		**Fracture (ε_{true_f})**	
Specimens	Velocity	Exp	Sim	Exp	Sim	Exp	SIM
S - RD=0°	0.00833 s^{-1}	1024	1030	1369	1373	0.159	0.163
S - RD=45°		1012	1000	1310	1316	0.177	0.180
S - RD=90°		1016	1020	1378	1376	0.167	0.169
S - RD=0°	0.042 s^{-1}	1020	1030	1328	1400	0.159	0.162
S - RD=45°		1012	996	1310	1319	0.177	0.178
S - RD=90°		1021	1030	1348	1358	0.176	0.178
S - RD=0°	0.16 s^{-1}	1053	1060	1328	1384	0.163	0.165
S - RD=45°		1009	1010	1288	1321	0.152	0.154
S - RD=90°		1070	1072	1368	1370	0.18	0.182

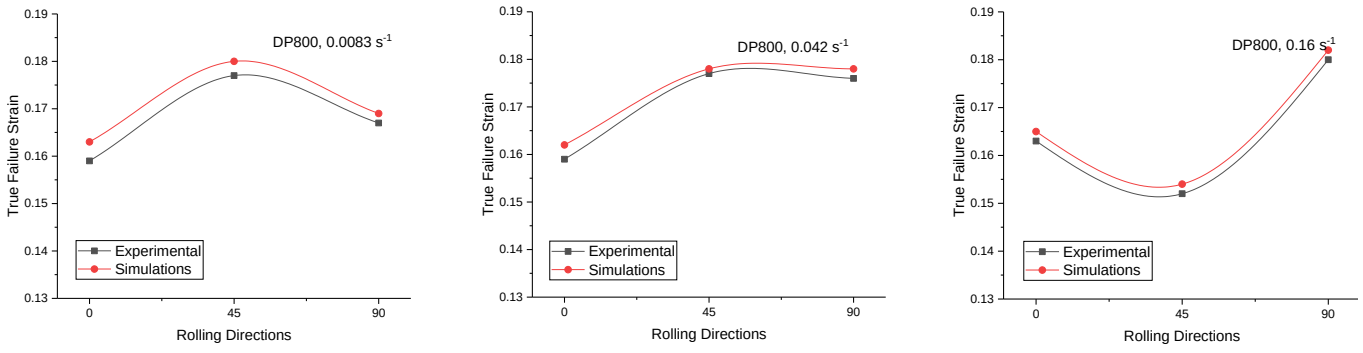

Figure 15. Experimental and simulation comparisons of DP800 steel as a result of different rolling directions and different strain rate.

The GTN parameters obtained from the optimization are presented in Table 6, with special emphasis on the samples mentioned in the table. All these final results were leaked as a result of the optimization made in LS-OPT, separately for each specimen.

Table 6. Exhibit parameters prediction of GTN of DP800 steel. ε_r= 0.0083 s^{-1}

Specimens GTN Parameters	ε_N	f_c	f_f	f_N	q_1	q_2	S_N
DP600, 0°, 0.00833 s^{-1}	0.2614	0.0020	0.3274	0.0430	1.0966	1.0715	0.0660
DP600, 45°, 0.00833 s^{-1}	0.3199	0.2196	0.7314	0.0144	0.8610	2.2	0.0378
DP600, 90°, 0.00833 s^{-1}	0.2693	0.4604	0.6357	0.0756	1.7334	1.8272	0.0345
DP600, 0°, 0.042 s^{-1}	0.2230	0.1722	0.1926	0.0324	1.6605	1.5819	0.0653
DP600, 45°, 0.042 s^{-1}	0.3199	0.2196	0.7314	0.0144	0.8610	2.2	0.0379
DP600, 90°, 0.042 s^{-1}	0.2620	0.1862	0.6617	0.0206	1.9337	1.8	0.0447
DP600, 0°, 0.16 s^{-1}	0.2636	0.4370	0.4572	0.0206	2.2835	1.8	0.033
DP600, 45°, 0.16 s^{-1}	0.2084	0.5074	0.3838	0.0192	2.5	1.8	0.0392
DP600, 90°, 0.16 s^{-1}	0.2493	0.0039	0.475	0.0351	1.0737	1.7999	0.0477

In relation to the numerical simulation results of the GTN model, and comparisons between specimens regarding effective plastic strain are particularly important, because their FEM values are similar to experimental values. Moreover, Figure 16. (a) depicts comparisons of EPS regarding DP600 steel, while Figure 16. (b) shows the comparison between numerical simulation results in the area of ESP regarding DP800 steel. These results are obtained from the simulations, which can be seen in Figures (b) from 8–14. Also, X stress in parallel with EPS was obtained.

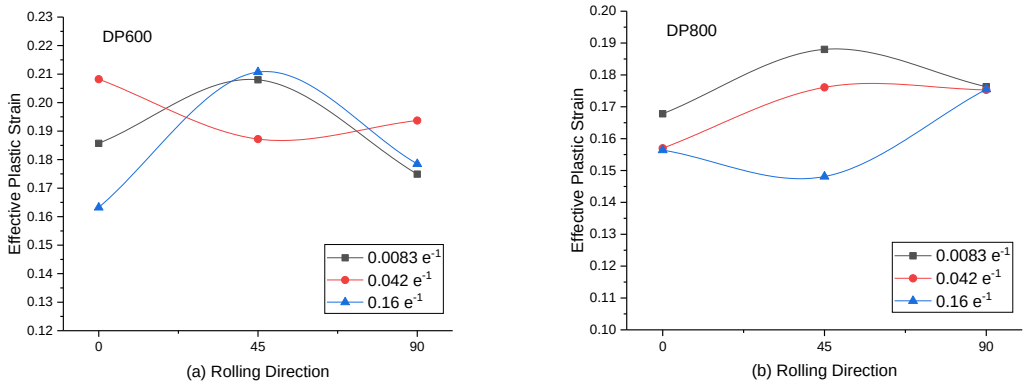

Figure 16. Finite element modeling comparisons of effective plastic strain between specimens tested at different strain rates with different rolling directions, (a) DP600 steel (b), DP800 steel

4. CONCLUSION

The presented work is divided into two parts of the study: the experimental study and the finite element modeling study.

The purpose of the experimental study was to investigate the behavior of steels cut from three different rolling directions and tested at three different strain rates. And as a result of this research, it turns out that the samples that belong to the same material but when their cutting was done in different angles, when thay were tested, they present different strain from each other, and all these changes stem from the orientations of the grains in the microstructure. Also, for the same samples, when analyzing is done at different strain rate, they show different extensions too. All experimental results were compared with each other by comparing the tested samples, which had similar strain rates but that the angle of prairie or rolling directions was different, and their results are given in the above figures.

On the other hand, in terms of finite element modeling, the aim was to find all GTN parameters through the optimization method that was realized in LS-OPT. Also, all the necessary parameters for the realization of optimizations are defined. The values of effective plastic strain that appear as a result of the finite element modeling results, as well as modeling stress displayed as x-stress, when they are compared with the experimental results, they have very good similarities. This means that the degree of strain and stress can be determined by paying attention to these FEM values. Finally, this optimization model is very convenient, and also serves to specify the parameters of other materials, and other models too.

GURSON-TVERGAARD-NEEDLEMAN (GTN) PARAMETERS OF DP STEELS WITH DIFFERENT ROLLING DIRECTIONS WERE DETERMINED AND INVESTIGATED AT DIFFERENT STRAIN RATES

SIMILARTY RATE: 6%

REFERENCES

[1] A. S. Podder, D. Bhattacharjee, and R. K. Ray, "Effect of martensite on the mechanical behavior of ferrite-bainite dual phase steels," *ISIJ Int.*, vol. 47, no. 7, pp. 1058–1064, 2007, doi: 10.2355/isijinternational.47.1058.

[2] C. M. Gómora, R. R. Ambriz, C. J. García, I. Ruíz-López, and D. Jaramillo, "Dissimilar Dual Phase-Low Carbon Steel Joints by the GMAW Process Subjected to Impact Load," *Metals (Basel).*, vol. 12, no. 3, pp. 1–18, 2022, doi: 10.3390/met12030404.

[3] C. Sébastien Y.P.Allain, Irina Pushkareva, JulienTeixeira, Mohamed Gouné, "Dual-Phase Steels: The First Family of Advanced High Strength Steels," *Encycl. Mater. Met. Alloy.*, 2022.

[4] S. Kang and H. Kwon: s, *No TitleMetall. Tran*. 1987.

[5] "www.arcelormittal.com." .

[6] M. Achouri, G. Germain, P. Dal Santo, and D. Saidane, "Experimental characterization and numerical modeling of micromechanical damage under different stress states," *Mater. Des.*, vol. 50, pp. 207–222, 2013, doi: 10.1016/j.matdes.2013.02.075.

[7] M. Feucht, D.-Z. Sun, T. Erhart, and T. Frank, "Recent development and applications of the Gurson model," in *LS-DYNA Anwenderforum*, 2006.

[8] F. Feng *et al.*, "Application of a GTN damage model predicting the fracture of 5052-O aluminum alloy high-speed electromagnetic impaction," *Metals (Basel).*, vol. 8, no. 10, 2018, doi: 10.3390/met8100761.

[9] K. L. Nielsen and V. Tvergaard, "Ductile shear failure or plug failure of spot welds modelled by modified Gurson model," *Eng. Fract. Mech.*, vol. 77, no. 7, pp. 1031–1047, 2010, doi: 10.1016/j.engfracmech.2010.02.031.

[10] R. O. Santos *et al.*, "Damage identification parameters of dual-phase 600-800 steels based on experimental void analysis and finite element simulations," *J. Mater. Res. Technol.*, vol. 8, no. 1, pp. 644–659, 2019, doi: 10.1016/j.jmrt.2018.04.017.

[11] M. H. Miloud, I. Zidane, and M. Mendas, "Coupled identification of the hardening behavior laws and Gurson–Tvergaard–Needleman damage parameters - validation on tear test of 12NiCr6 CT specimen," *Frat. ed Integrita Strutt.*, vol. 13, no. 49, pp. 630–642, 2019, doi: 10.3221/IGF-ESIS.49.57.

[12] F. Andrade and M. Feucht, "A comparison of damage and failure models for the failure prediction of dual-phase steels," 2017.

[13] C. Netrasiri and S. Suranuntchai, "Damage curve determination of dual phase steel based on gtn mode-l failure criteria," *Int. J. Mech. Eng. Robot. Res.*, 2016, doi: 10.18178/ijmerr.5.4.268-271.

[14] Y. Bao and T. Wierzbicki, "On fracture locus in the equivalent strain and stress triaxiality space," *Int. J. Mech. Sci.*, 2004, doi: 10.1016/j.ijmecsci.2004.02.006.

[15] H. Chalal and F. Abed-Meraim, "Determination of forming limit diagrams based on ductile damage models and necking criteria," *Lat. Am. J. Solids Struct.*, vol. 14, no. 10, pp. 1872–1892, 2017, doi: 10.1590/1679-78253481.

[16] M. Achouri, G. Germain, P. Dal Santo, and D. Saidane, "Numerical integration of an advanced Gurson model for shear loading: Application to the blanking process," *Comput. Mater. Sci.*, vol. 72, pp. 62–67, 2013, doi: 10.1016/j.commatsci.2013.01.035.

[17] N. STANDER, W. ROUX, T. GOEL, T. EGGLESTON, and K. E. N. CRAIG, *LS-OPT User ' s Manual: A DESIGN OPTIMIZATION AND PROBABILISTIC ANALYSIS TOOL*, no. February. 2012.

[18] N. A. Tvergaard, V, "Analysis of the cup-cone fracture in a round tensile bar," 1984.

[19] M. Springmann and M. Kuna, "Determination of ductile damage parameters by local deformation fields: Measurement and simulation," *Arch. Appl. Mech.*, vol. 75, no. 10–12, pp. 775–797, 2006, doi: 10.1007/s00419-006-0033-9.

Eurasian Journal of Science Engineering and Technology

Research

A COMPARATIVE STUDY ON THE PHOTORESIST PATTERNING OF GLASS AND SILICON WITH MICROHOLES VIA MASKLESS PHOTOLITHOGRAPHY

Furkan GÜÇLÜER[1], Filiz KELEŞ[2*]

[1] *Nigde Ömer Halisdemir University, Department of Energy Science and Technologies, 51240, Nigde, Türkiye*
[1,2] *Nigde Ömer Halisdemir University, Nanotechnology Application and Research Center, 51240, Nigde, Türkiye*
[2] *Nigde Ömer Halisdemir University, Department of Physics, 51240, Nigde, Türkiye*

ABSTRACT

Maskless photolithography, a useful tool used in patterning the photoresist which acts as a mask prior to the actual etching process of substrate, has attracted attention mainly due to the taking advantage of reducing cost because of not requiring a preprepared mask and freedom in creating the desired pattern on any kind of substrate. In this study, we performed the positive photoresist patterning with microstructures on both glass and silicon substrates via maskless photolithography. Specifically, we examined the discrepancies between the transparent (glass) and reflective (silicon) substrates even though the photolithographic process has been carried out under the same conditions. Since the positive photoresist patterning was the subject of this study, we could successfully produce the microholes with almost circular shapes and properly placed in squarely packed on both substrates as confirmed by optical microscopy and profilometer mapping measurements. We observed additional rings around the holes when silicon was used as substrate while very clear microholes were obtained for glass. Besides, the number of the rings increased when the writing speed of laser (velocity) reduced. We claim that these important findings can be attributed to the standing wave effect phenomenon which results from the multiple reflections through the semi-transparent photoresist coated on the reflective surface of the polished silicon. In brief, we reveal an important conclusion, in this study, based on the differences in formation of the microholes only due to the substate preference while all the photolithographic process parameters are kept the same.

Keywords: Maskless photolithography, Positive photoresist, Microholes, Glass, Silicon, Standing wave effect

1. INTRODUCTION

Minimizing the reflection caused by the interaction of incident light with the material surface and thus maximizing the absorption has been intensely studied in literature to improve the performance of optoelectronic devices especially such as photodetectors [1, 2] and solar cells [3, 4]. Surface patterning is one of the most preferred methods regarding in reducing reflection from sample surface. The microstructures with different shapes and physical properties are mainly preferred to pattern the substrates specifically glass and silicon via etching. The etching process to conduct the patterning of the substrate can be classified mainly as wet [5, 6] and dry [7, 8] based on either physical or chemical interactions subjected. Prior to the etching process, the usage of an appropriate patterning mask with well-defined structures in micro-scale is vital to carry out a successful patterning. Photolithography is one of the most efficient, versatile, and practical methods to obtain a well-prepared mask.

Photolithography is operated to perform the photoresist delineation with microstructures for a more controllable surface patterning prior to the actual etching. Therefore, a well-defined complete etching is mainly dependent on a successful lithographic process. The photolithography can be operated via with and without a mask. In the masked photolithography [9], exposing process occurs faster since the laser shines on the whole substrate at the same time through a mask. Contrary to this advantage, the price of the mask is the main factor that reduces the interest in masked photolithography. In the maskless lithography, on the other hand [10], an extraordinary parameter called laser velocity (writing speed, mm/s) has an important role in determining the exposing process as the maskless lithography is like directly writing with a laser pen. Another advantage of the direct laser writer system is that it can be performed for patterning in different shapes without using any additional masks unlike the masked photolithography.

Photolithography is generally carried out by three steps called coating of photoresist, laser exposure and development. For the photoresist, a light-sensitive and polymer-structured material, homogenous coating with desirable thickness is important. To achieve a homogenous photoresist coating, the process of spin coating parameters such as temperature and speed of rotation should be tuned accordingly [11]. The second step is the laser exposure onto the photoresist. There are two types of photoresists; positive [12, 13] and negative [14, 15]. When the positive photoresist is used, the laser exposed areas of the photoresist are weakened and cleared off during the development step. Whereas, the parts exposed to the laser of photoresist are strengthened

* Corresponding author, e-mail: fkeles@ohu.edu.tr (F. Keleş)
Recieved: 30.07.2022 Accepted: 28.09.2022
doi: 10.55696/ejset.1150239

and the remaining parts are removed by development in negative photoresist process. The wavelength and power of the laser are important parameters for the exposing step. In the development step, the duration of the chemical bath and the solution temperature [16] are two effective parameters. Through the photolithographic steps, the following facts such as photoresist uniformity, alignment, overexposing, pattern resolution and standing wave effect [17] need to be evaluated carefully.

In this study, we used soda lime glass (SLG) and polished float zone (FZ) silicon substrates to carry out the positive photoresist patterning via maskless photolithography. We spin coated the photoresist onto the substrates under the same conditions and then, the laser exposition with the same parameters onto the photoresist on the substrates has been carried out. Finally, the development step of both substrates was conducted simultaneously. We mainly conducted a study based on the formation of microholes on the photoresist on two different substrates. Furthermore, whether the physical properties of the microholes differ or not according to the preferred substrate has been investigated.

2. MATERIAL AND METHOD

Soda lime glass (SLG) and polished (FZ) silicon used as substrates in this study to observe the difference in photolithographic process for transparent and reflective materials, respectively. Two different processes were applied for two different substrates for the cleaning procedure. The glass substrate was cleaned with acetone for 5 minutes, isopropyl alcohol for 5 minutes and deionized water for 10 minutes, respectively, by ultrasonic bath and then dried with nitrogen gas. The RCA (Radio Corporation of America) cleaned silicon was additionally cleaned with hydrofluoric acid for 90 seconds and then washed with distilled water for 30 seconds to remove the natural oxide layer on its surface.

Both clean glass and silicon substrates were then heated up to 200 ^{0}C on hot plate to remove possible residues. Then, the substrates were placed onto spin coating and rotated at 4000 rpm for photoresist coating. A positive type of photoresist, Shipley S1805 was used as photoresist material. Figure 1 represents the hot plate device, spin coating system and the schematic representation of the photoresist coating onto substrate.

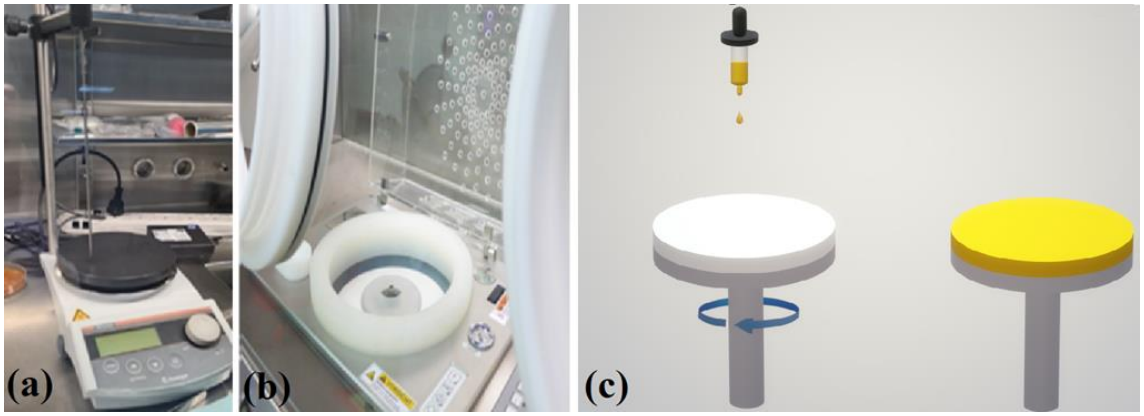

Figure 1. Hot plate device (a), spin coating system (b) and schematic representation of the photoresist coating (c).

Table 1. Sample names obtained by only contouring & contouring and filling with different laser velocities.

Sample Name	**Contour & Filling**		**Velocity (**mm/s**)**	
	Contour	**Filling**	**Contour**	**Filling**
G-CF	✓	✓	0.3	10
S1-CF	✓	✓	0.3	10
S2-C	✓	**X**	0.4	**X**
S2-CF	✓	✓	0.4	13
S3-C	✓	**X**	0.6	**X**
S3-CF	✓	✓	0.6	13

A maskless photolithography instrument, Kloe Dilase 650, was operated for the exposure process. The wavelength of the laser used during the process was 375 nm (Ultraviolet). The microstructures with desired diameters in squarely packed construction that constitute the pattern were first defined by the device's software and then the pattern was transferred onto the photoresist via laser exposure. During the defining of microstructures prior to the laser operation, the two parameters called "contour" and "filling" to outline the circles and to fill in the circles, respectively, should be applied. We have produced the patterns of microstructures with contour only and contour and filling for comparison in terms of structural formation. Additionally, the laser parameter of velocity (writing speed, mm/s) has been differed as well during the contour and filling formation of the circles. As the velocity decreases, the larger area of photoresist is affected since the photoresist is exposed by the laser for a longer time, and vice versa. The samples obtained with only contour & contour and filling under different velocities are summarized in Table I.

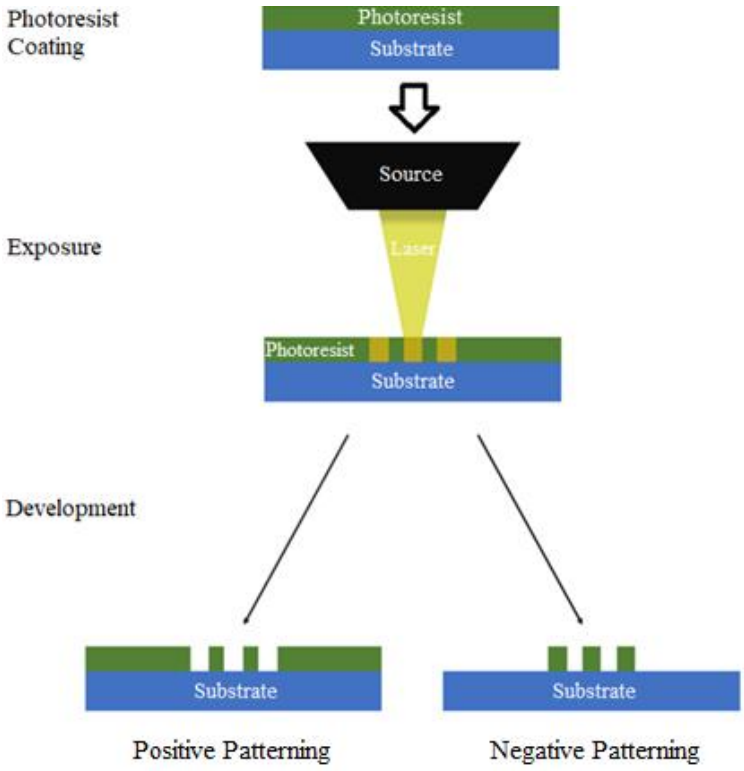

Figure 2. Schematic illustration of positive and negative patterning process steps via maskless photolithography.

Microposit MF-319 was used in the development process for positive photoresist. The substrates coated with photoresist with the patterns of microstructures were immersed into the developer solution for a few seconds. Then, the substrates were washed with deionized water and dried with nitrogen gas, respectively. After the development process, the substrates were heated and stayed at 100 ^{0}C for 1 min on hot plate for the evaporation of any unwanted chemicals that could possibly remain. The three main steps for the photolithography process to obtain positive or negative patterning is schematically demonstrated in Figure 2.

In this study, we performed the positive photoresist patterning. Thus, we obtained the microholes on photoresist for both substrates because of photoresist delineation. The top view images of microholes were captured by optical microscopy of photolithography device. The angled images and dept profiles of the patterns were obtained by profilometer (Bruker DektakXT).

3. RESULTS AND DISCUSSION

Top view and angled images of SLG and silicon with microstructures obtained by optical microscopy and profilometer, respectively, are demonstrated in Figure 3 (a-d). The regarding depth profiles of the patterns measured by a line laterally drawn through the microholes can be seen in Figure 3 (e-f). Since the same procedure has been applied for the depth profile measurement for both samples, the line was added only to the SLG image.

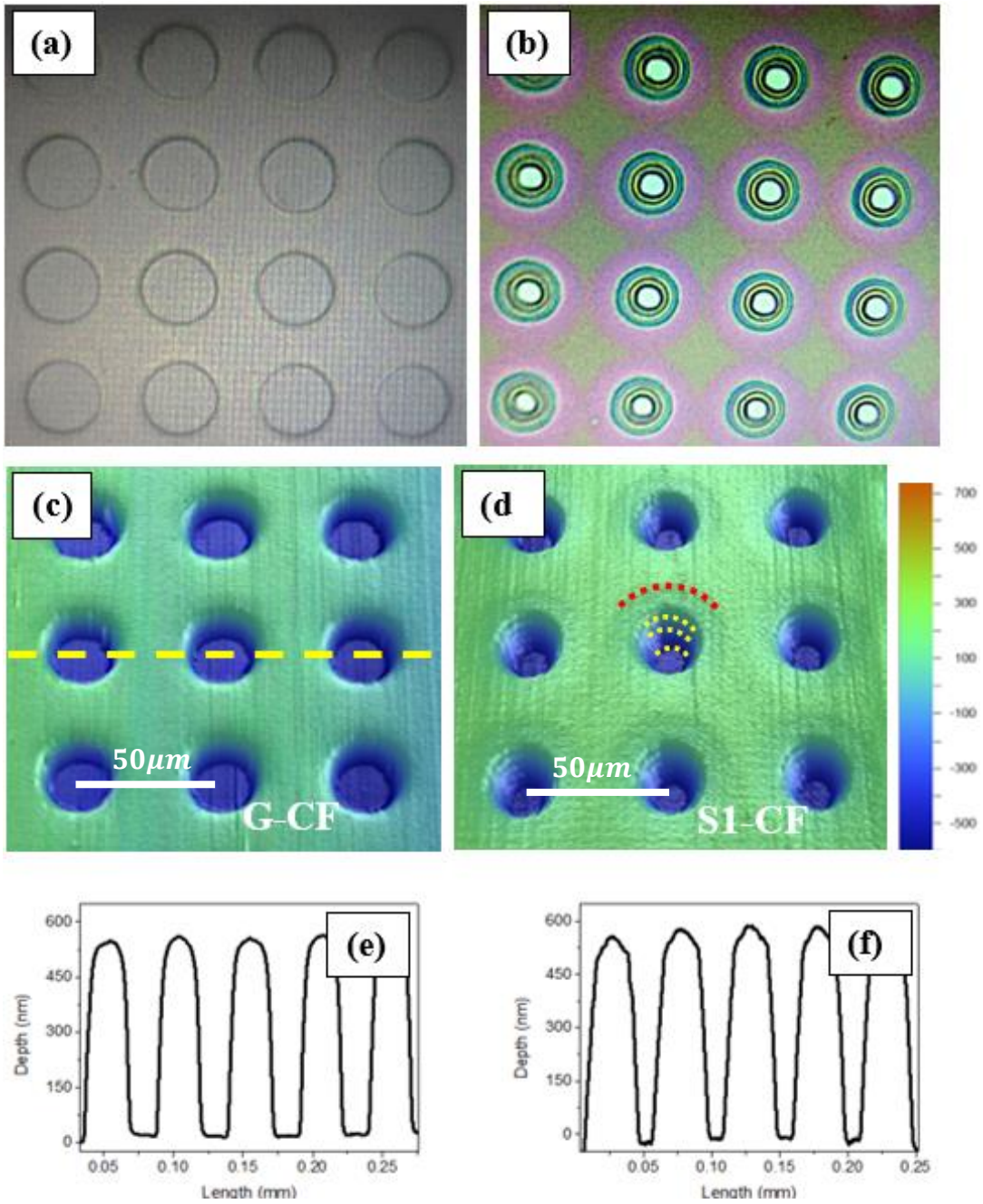

Figure 3. The top (optical microscopy) and angled (profilometer) images of microholes delineated on photoresit coated on SLG (a & c) and silicon (b & d), respectively; the regarding depth profiles of SLG and silicon obtained by laterally drawn line through microholes.

The most significant difference between the performed patterns made up of microholes on glass and silicon is the formation of the rings when the silicon is used as substrate while no ring is observed for glass. Since the photoresist patterning process is the same for both substrates, the main reason behind this important finding is probably due to the optical reflection properties of the substrates. Since glass is quite transparent in UV-Vis range [18], the laser passes through both semi-transparent photoresist and glass. Therefore, one-directional trajectory of the laser results in formation of almost perfectly circular microholes. On the other hand, silicon with a polished surface has approximately 30-40 % reflectance of light in UV-Vis range [19]. As a result, the laser has been subjected to the multiple reflections from the silicon surface which produces the standing wave effect and thus, the circles along with the microholes are formed on photoresist coated silicon. Standing wave effect is a phenomenon that

generally observed when a substrate with reflective surface is used. The meeting of the incident light with the reflected light results in the formation of constructive and destructive interference creates the standing waves [20].

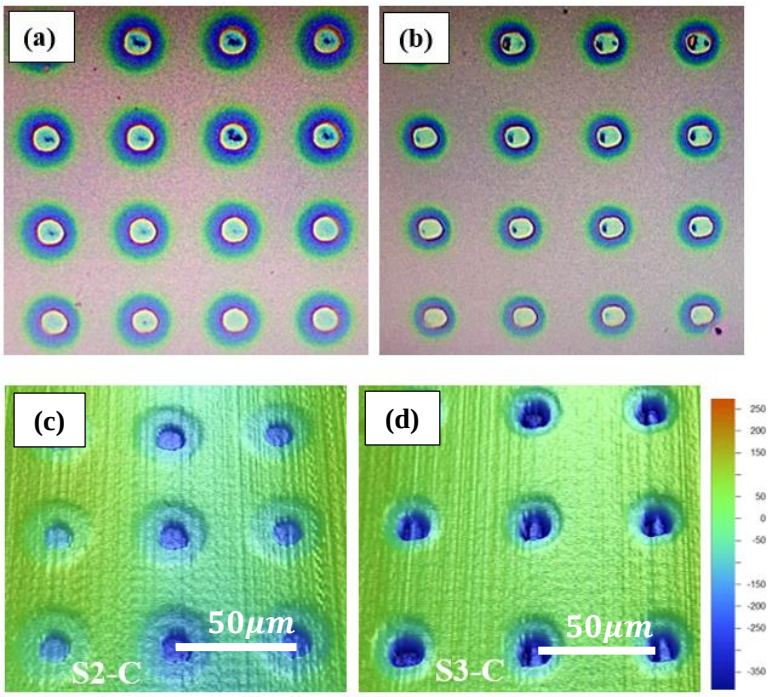

Figure 4. The top (optical microscopy) and angled (profilometer) images of microholes delineated on silicon only by contour formation under different velocities; samples of S2-C (a & c) and S3-C (b & d), respectively.

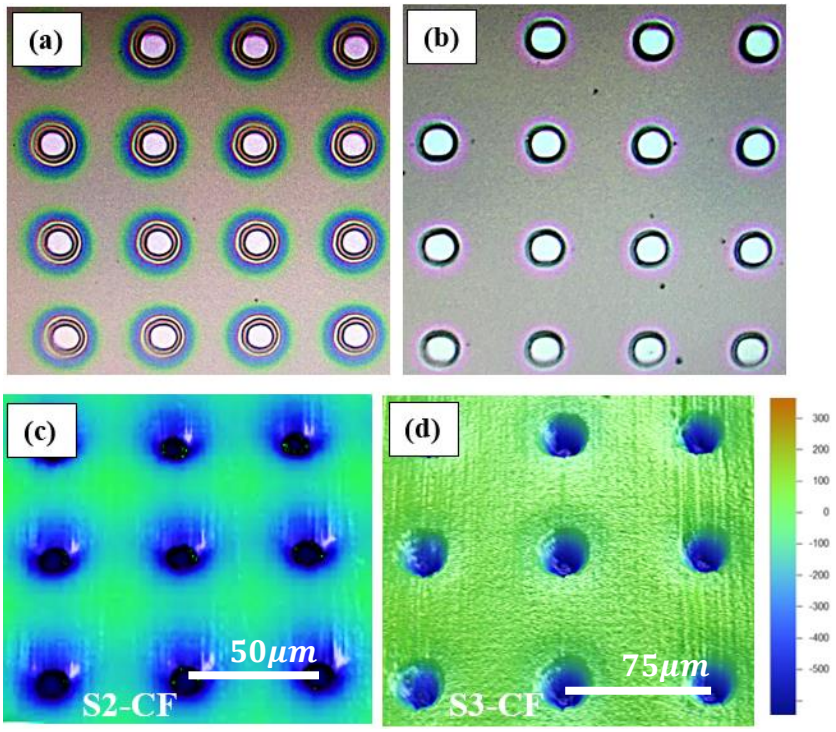

Figure 5. The top (optical microscopy) and angled (profilometer) images of microholes delineated on silicon by both application of contour and filling under different velocities; samples of S2-CF (a & c) and S3-CF (b & d), respectively.

To further investigate the origin of the rings observed around the microholes when silicon is used as substrate, the patterning process of microholes were performed by only countering and both contouring and filling at various laser writing speeds. The details of the samples are given in Table I. The most direct conclusion can be interpreted from Figures 4 & 5 is that the outermost ring is due to the contour application regardless of speed of laser. Indeed, the ring with the purplish color in Figure 3b as labeled by a red semi-circle in Figure 3d has the similarity with the samples demonstrated in Figures 4 & 5. As can be predicted, all blurry purplish rings around the microholes seen in optical microscopy images can be attributed to the reflection of light from the shiny surface of silicon during the contouring process. Moreover, another important interpretation is that the number of rings increases by decreasing of the laser writing speed during contouring of the circles. This is due to the higher duration of laser on photoresist for the lower speed.

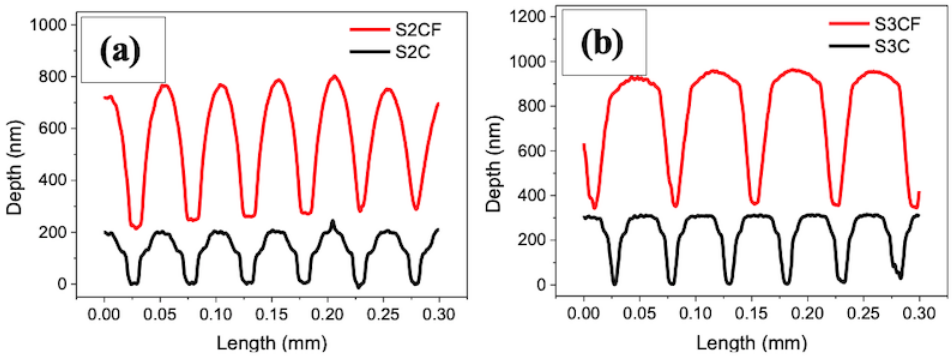

Figure 6. The depth profiles of the samples obtained by only contouring and both contouring and filling. S2C-S2CF and S3C-S3CF depth profiles are given in (a) and (b), respectively.

The depth profiles of the samples named S2C-S2CF & S3-S3CF obtained under different laser speeds of contouring are given in Figure 6 (a & b). It is apparent that the depth of the photoresist can be etched only up to 200-300 nm for both samples when only contouring is carried out. While the measured depth for the samples of S2CF & S3CF (when both contouring and filling applied) is about ~ 500-600 nm which is equal to the coated thickness of the photoresist itself. The more and less deep microholes shown in the profilometer images in Figures 4 & 5, respectively, are correlated with the depth profiles. In addition, since the contour velocity of the laser in the S3C and S3CF samples are higher than S2C and S2CF, Figure 6a represents sharper curve. Accordingly, there are fewer microholes in the S3CF curve in the equal scanning line (0.3 mm) and this resulted in the S3C and S3CF curves not being aligned. Indeed, this situation can be even understood when the scale bars of the Figure 5c and 5d are compared, as the distance between the microholes is bigger in Figure 5d.

4. CONCLUSION

In summary, patterning the positive photoresist coated on glass and silicon substrates with microholes via maskless laser writer photolithography was successfully carried out in this study. It was confirmed by both optical and profilometer images that well-defined, organized and almost perfectly circular microholes could be produced regardless of process parameters. Besides, the penetration depths of the circles obtained for only contouring and contouring & filling can be determined approximately ~ 200-300 nm and ~ 500-600 nm, respectively, from depth profiles. The homogenous coating of photoresist interpreted from the images and depth profiles is another important finding that is revealed in this study. On the other hand, the formation of the rings around the microholes when silicon is used as substrate while no ring is observed for glass is quite important observation that should be considered. Moreover, the number of rings increases by the lower laser speed. The most possible reason for these findings can be attributed to the transparency and reflectivity properties of glass and silicon, respectively. The laser is subjected to multiple reflections from the shiny surface of silicon while the laser is passes through the glass. Therefore, the phenomenon called standing wave effect arises for silicon which results in the rings. Since the laser stays more on the photoresist when the laser speed is low, the standing effect becomes more apparent thus the number of rings increases. On the contrary, very clear and smooth microholes without any ring are obtained for glass. To sum up, we revealed a successful study on the formation of patterns made up of microholes on the positive photoresist on two different substrates. The differences on the patterns due to the reflectivity properties of substrates are explained and demonstrated. In this regard, we believe the results shared in this study would make a contribution to the literature especially in photolithographic area.

SIMILARTY RATE: 2%

ACKNOWLEDGEMENT

The photoresist patterning and characterization of the glass and silicon substrates was conducted in Nanotechnology Application and Research Center at Nigde Ömer Halisdemir University. The authors would like to thank to Dr. Ayşe SEYHAN for the valuable discussions.

REFERENCES

[1] M. Sun *et al.*, "Broad-band three dimensional nanocave ZnO thin film photodetectors enhanced by Au surface plasmon resonance," *Nanoscale*, vol. 8, no. 16, pp. 8924-8930, 2016.
[2] H. N. Pham *et al.*, "The enhancement of visible photodetector performance based on Mn doped ZnO nanorods by substrate architecting," *Sensors and Actuators A: Physical*, vol. 311, p. 112085, 2020.
[3] K.-S. Han, J.-H. Shin, W.-Y. Yoon, and H. Lee, "Enhanced performance of solar cells with anti-reflection layer fabricated by nano-imprint lithography," *Solar Energy Materials and Solar Cells*, vol. 95, no. 1, pp. 288-291, 2011.
[4] C. López-López *et al.*, "Multidirectional light-harvesting enhancement in dye solar cells by surface patterning," Advanced Optical Materials, vol. 2, no. 9, pp. 879-884, 2014.
[5] Y. Wang *et al.*, "Maskless inverted pyramid texturization of silicon," *Scientific Reports*, vol. 5, no. 1, pp. 1-6, 2015.
[6] J. Sheu, H. Chou, W. Cheng, C. Wu, and L. Yeou, "Silicon Nanomachining by Scanning Probe Lithography and Anisotropic Wet Etching," in Materials & Process Integration for MEMS: Springer, 2002, pp. 157-174.
[7] S. H. Zaidi, D. S. Ruby, and J. M. Gee, "Characterization of random reactive ion etched-textured silicon solar cells," IEEE Transactions on Electron Devices, vol. 48, no. 6, pp. 1200-1206, 2001.
[8] A. Baram and M. Naftali, "Dry etching of deep cavities in Pyrex for MEMS applications using standard lithography," *Journal of Micromechanics and Microengineering*, vol. 16, no. 11, p. 2287, 2006.
[9] J. A. Corno, "Chemical and structural modification of porous silicon for energy storage and conversion," *Georgia Institute of Technology*, 2008.
[10] M. Z. Mohammed, A.-H. I. Mourad, and S. A. Khashan, "Maskless lithography using negative photoresist material: impact of UV laser intensity on the cured line width," *Lasers in Manufacturing and Materials Processing*, vol. 5, no. 2, pp. 133-142, 2018.
[11] J. Schober, J. Berger, C. Eulenkamp, K. Nicolaus, and G. Feiertag, "Thick film photoresist process for copper pillar bumps on surface acoustic wave-wafer level packages," in 2020 IEEE 8th Electronics System-Integration Technology Conference (ESTC), 2020: IEEE, pp. 1-7.
[12] I. Khandaker, D. Macintyre, and S. Thoms, "Fabrication of microlens arrays by direct electron beam exposure of photoresist," *Pure and Applied Optics: Journal of the European Optical Society Part A*, vol. 6, no. 6, p. 637, 1997.
[13] J. Koch *et al.*, "Maskless nonlinear lithography with femtosecond laser pulses," *Applied Physics A*, vol. 82, no. 1, pp. 23-26, 2006.
[14] V. Starkov, E. Y. Gavrilin, J. Konle, H. Presting, A. Vyatkin, and U. König, "SU8 photoresist as an etch mask for local deep anodic etching of silicon," *Physica Status Solidi (A)*, vol. 197, no. 1, pp. 150-157, 2003.
[15] M. Han, W. Lee, S.-K. Lee, and S. S. Lee, "3D microfabrication with inclined/rotated UV lithography," *Sensors and Actuators A: Physical*, vol. 111, no. 1, pp. 14-20, 2004.
[16] M.-C. Chou, C. Pan, T. Wu, and C. Wu, "Study of deep X-ray lithography behaviour for microstructures," *Sensors and Actuators A: Physical*, vol. 141, no. 2, pp. 703-711, 2008.
[17] C. A. Mack. "Semiconductor Lithography (Photolithography) - The Basic Process." http://www.lithoguru.com/scientist/lithobasics.html (accessed July 24, 2022).
[18] S. M. Karazi, I. U. Ahad, and K. Benyounis, "Laser Micromachining for Transparent Materials," 2017.
[19] S. Hava, J. Ivri, and M. Auslender, "Wavenumber-modulated patterns of transmission through one-and two-dimensional gratings on a silicon substrate," *Journal of Optics A: Pure and Applied Optics*, vol. 3, no. 6, p. S190, 2001.
[20] C. A. Mack, "Analytical expression for the standing wave intensity in photoresist," *Applied Optics*, vol. 25, no. 12, pp. 1958-1961, 1986.

Eurasian Journal of Science Engineering and Technology

Research

INVESTIGATION OF THE EFFECT OF BENDING PROCESS ON FATIGUE LIFE AND MECHANICAL STRENGTH OF HEAVY COMMERCIAL VEHICLE DRAG LINKS

İbrahim KILINÇ[1,*], Serkan TOROS[2]

[1]*DİTAŞ Doğan Spare Parts and Manufacturing Inc., R&D Center, Niğde/Türkiye*
[2]*Niğde Ömer Halisdemir University, Department of Mechanical Engineering, Niğde/Türkiye*

ABSTRACT

In heavy commercial vehicles, the part that enables the wheels to turn left and right by transferring the movement from the steering box to the wheel via the pitman is called the steering drag link. In order to obtain the desired form in the production of bended drag links, the pipe material is subjected to bending process from certain points by various methods. During this bending process, plastic deformation occurs in the material. In this study, the effect of plastic deformation in tie rod bending on the life of the drag link was investigated. The amount of plastic deformation in the bending region was determined as %12 by performing tie rod bending simulation in a Finite Element Analysis (FEA) software. The fatigue behavior of the %6 and %12 pre-strained material was determined and compared with the fatigue behavior of the undeformed material. Fatigue analyses were carried out in the finite element environment by modeling the drag link as Functionally Graded Material (FGM). In addition, the drag link physical fatigue tests were also carried out and the numerical and experimental results were compared. It was observed that the results of the drag link fatigue analysis modeled as FGM were closer to the experimental values.

Keywords: Drag link, Pipe bending, Plastic deformation, Steering system, Fatigue

1. INTRODUCTION

The drag link is an important part of the steering system that provides the wheels to turn right and left by transmitting the movement from the steering wheel to the wheels. Drag link generally consists of connecting two rod ends with each other by means of a connecting rod. Connecting rods of drag links are generally produced from pipe materials due to their lightness and low cost. Drag links are bent at different offset amounts due to their distance from other components within the scope of vehicles' steering systems and legal regulation requirements. Even if statically high-strength materials are used in drag links, they can be damaged at lower loads when exposed to repeated loads on the vehicle. The process of premature failure or damage of a component as a result of repeated loading is called metal fatigue [1]. In case the vehicles encounter different road conditions, various tensile and compressive stresses may occur on the drag link. These variable stresses produce fatigue, causing microcracks to occur, and the tie rod may be damaged by cracking in the future [2].

DP600 steel material with pre-strain applied in different directions has higher yield strength and fatigue resistance than material without prestrain [3]. Koh and Baek [4] performed a fatigue damage analysis to estimate the fatigue life of a steering drag link. Monotonic tensile and low cycle fatigue tests were performed for the STKM12C steel pipe used in the drag link. In addition, FEA studies were performed to determine the regional stresses and strains in critical bending regions. To verify the FEA results, they experimentally measured the amount of strain in the bending regions by placing a strain gauge on the drag link bend regions. Fatigue life was estimated using a combination of material properties, stress analysis and local strain approach. They performed the drag link fatigue test at 3 different loads and observed that a crack first formed in the bending region and then the crack propagated and the tie rod broke along the cross-sectional area. Lee et al. [5] investigated the fatigue properties of low-carbon steel pipes bent at small radius using the district induction heating method. The microstructure, hardness, high cycle fatigue and residual stress properties of the inner and outer wall sections of the bent pipe in the bending region were compared with the unbent raw pipe properties. They stated that deformed bending walls show better fatigue properties. Budak and Pekedis [6] investigated the effect of pre-deformation on fatigue strength by performing fatigue tests and finite element analyzes for a pre-deformed automobile tie rod end without any pre-deformation. In the finite element analysis, it was seen that the critical regions formed in the rod ends matched the damage regions observed as a result of the experimental tests. The numerical and experimental results they obtained indicate that the pre-deformation affects the fatigue life of the rod end negatively and should be taken into account during the design. Uludamar et al. [7] performed the finite element analysis of a

* Corresponding author, e-mail: ibrahimkilinc@ditas.com.tr (İ. Kılınç)
Recieved: 28.10.2022 Accepted: 25.11.2022
doi: 10.55696/ejset.1195927

drag link and determined the stress values and safety coefficient on the part. They also calculated the resulting stresses theoretically and compared the results. Falah et al. [8] performed a damage analysis of a broken rod end ball joint. They conducted an assessment to determine the cause of the damage to the tie rod end of an SUV that had run for about two years and less than 30,000 km. Visual inspection, chemical analysis, hardness measurement and metallographic examination were performed on the part. They stated that the joint neck region was damaged due to fatigue and crack initiation due to insufficient material and improper heat treatment. Güvenç and Botsalı [9] investigated the fatigue life of the tie rod end, which is a part of the steering system, using computer aided engineering tools. By determining the points where fatigue can occur on the tie rod end in the finite element environment, strain gauges were placed in the critical areas of the tie rod end of a passenger vehicle. The vehicle was exposed to different road conditions and 400 km of road data were collected. According to the calculations they made in the Computer Aided Engineering (CAE) environment using these data, they concluded that the part life is infinite for 300,000 km of data. To confirm this result, they performed an experimental simulation of the tie rod end and said that the results were compatible with each other. Peng et al. [10] investigated the effect of pre-strain on mechanical properties for 316L austenitic stainless steel. They compared the mechanical properties of the samples to which they applied different pre-strain values between 0% and 35%. They showed that the yield points increased, the elongation decreased, and the maximum stress remained constant with increasing pre-strain.

In this study, the effect of plastic deformation occurring during drag link bending process on drag link fatigue behavior was investigated. Ansys finite element software was used to determine the amount of plastic deformation that occurs during the bending process.

Although there are fatigue analysis studies for drag links in the literature, plastic deformation from the bending process is generally ignored in these analyses. In this study, the plastic deformation occurring during the bending process was determined and used as an input in the analyses.

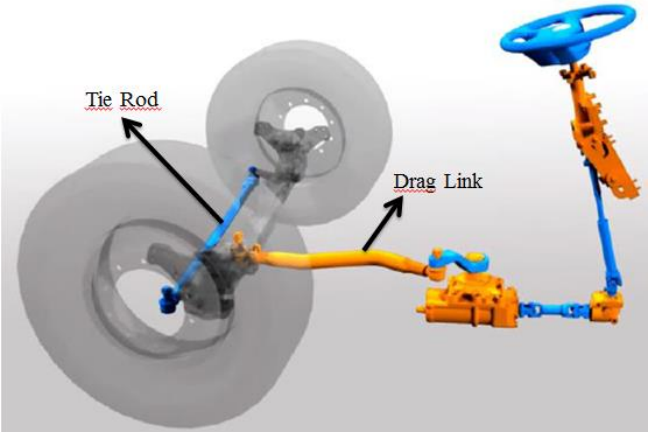

Figure 1. Heavy commercial vehicle steering system [11]

2. MATERIAL AND METHOD

2.1 Materials

In order to determine the fatigue behavior of the drag link pipe material, EN 10025-2 S355JR+N in solid form equivalent to the drag link pipe material EN 10305-1 E355+N was used. The chemical composition of these materials are shown in Table 1.

Table 1. Chemical compositions of E355+N and S355JR+N materials (wt %) [12,13].

Content (%)	E355+N	S355JR+N
C (max)	0.22	0.24
Si (max)	0.55	0.55
Mn (max)	1.60	1.60
P (max)	0.025	0.035
S (max)	0.025	0.035

2.2 Experimental Procedures

The tensile and fatigue test specimens required to determine the mechanical properties of E355+N pipe material and S355JR+N solid material were prepared according to the relevant standards. In addition to the S355JR+N material fatigue tests to determine the drag link fatigue behavior, the drag link bending operation will be simulated in the finite element software in order to see the effect of plastic deformation during the bending operation. The plastic strain obtained as a result of the analysis will be applied to the S355JR+N material as a pre-strain, and the fatigue tests of the samples will be performed separately.

Tensile Tests

In order to determine the mechanical properties of E355+N pipe material, tensile samples were prepared according to DIN 50125 standard on E355+N seamless pipe material with an outer diameter of 52 mm and a wall thickness of 7 mm. Pipe material drawing sample geometry is shown in Figure 2.

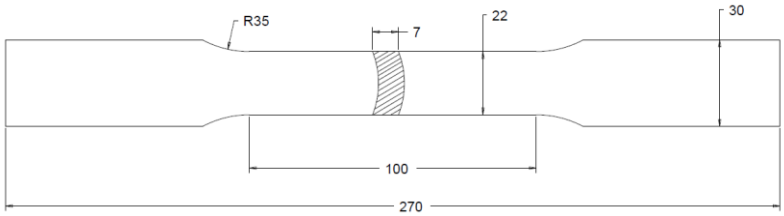

Figure 2. Tensile specimen geometry created according to DIN 50125

The tensile specimen geometry prepared according to the DIN 50125 standard for the determination of the mechanical properties of the S355JR+N solid material is shown in Figure 3.

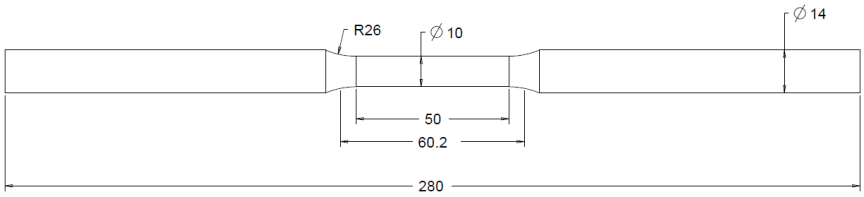

Figure 3. DIN 50125-A 10x50 tensile specimen geometry

Tensile tests were carried out in the tensile testing device with a load capacity of 600 kN shown in Figure 4.

Figure 4. Tensile test device

Fatigue Tests

20 fatigue specimens were prepared according to ASTM E466 from S355JR+N material to be used in fatigue tests. The fatigue specimen geometry is shown in Figure 5.

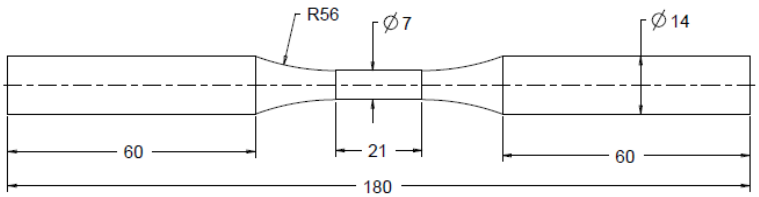

Figure 5. Geometry of fatigue test specimen acc. to ASTM E466

10 specimens without pre-strain were tested in the uniaxial fatigue test device shown in Figure 6. It was tested in 5 different loads (9 kN, 8 kN, 7 kN, 6 kN, 5 kN) at a frequency of 5 Hz until it broke, by making two repetitions at each load value. The plastic deformation that determined as a result of the pipe bending simulation was applied to 10 fatigue specimens and the fatigue test of the specimens was carried out at the same load and frequency values.

Figure 6. Uniaxial fatigue test device

Drag Link Fatigue Tests

Actual fatigue tests of drag links were carried out. The fatigue test setup is shown in Figure 7. Accordingly, the drag link was fixed from the rod end on one side and subjected to axial loading from the rod end on the other side. Fatigue tests were carried out at 5 Hz frequency of a total of 4 tie rods, two for each, at 2 different loads (20 kN, 25 kN).

Figure 7. Drag link fatigue test setup

2.3 Finite Element Simulations

Bending Process Simulation

The amount of plastic deformation in the pipe bending region was determined by simulating the manual press pipe bending process in the ANSYS software. The cad model required for the analysis was modeled in the Creo Parametric 3.0 software. The pipe bend analysis setup is shown in Figure 8.

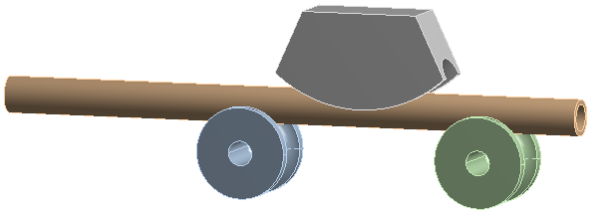

Figure 8. Pipe bending setup with manual press method

Multilinear kinematic hardening module of ANSYS software is used. Nonlinear analysis was performed by using only the plastic values of the actual stress-strain curve of the S355JR+N material as input to the analysis. Pipe domains were meshed with tetrahedrons mesh as shown in Figure 9. Bending die and support rollers were defined as rigid. The support roller is free to rotate around its own axis, and the bending die is released to move in the vertical +Y axis. The bending die was retracted after 35 mm displacement and the pipe was released.

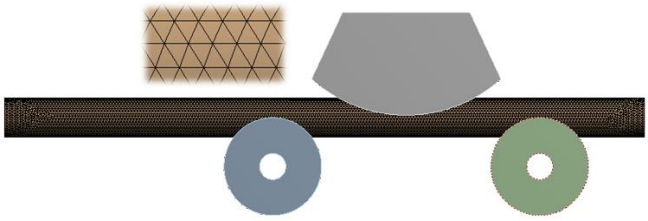

Figure 9. Bending setup mesh state

Drag Link Fatigue Simulation

Since the drag link has different strain levels in the bending region during the drag link bending, fatigue analysis was performed by modeling the drag link as functional grades. The simulations performed using the parts modeled in the FGM structure give consistent results with the experimental results [14]. While creating the functionally graded model, the model was created by considering the wall thickness changes that occur in the inner and outer walls of the bending region in the real environment. At the same time, analyzes were made for the one-piece model without any pre-strain. Figure 10 and Figure 11 show the cad images of no pre-strain model and functionally graded drag link.

Figure 10. Drag link cad image without pre-strain

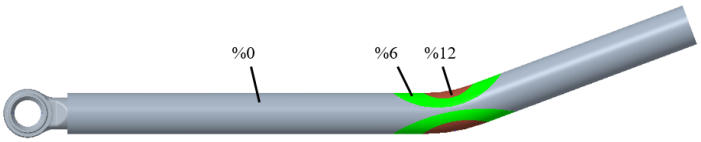

Figure 11. Functional graded drag link cad image

Fatigue analyzes were carried out by fixing the drag link from the inner surface of the housing in the Ansys finite element software and subjecting it to different loads from the housing center on the opposite side. Drag link domains were meshed with tetrahedrons mesh with 707836 elements as shown in Figure 12.

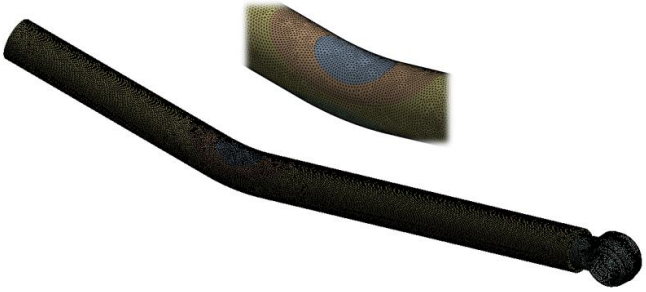

Figure 12. Mesh state of drag link fatigue analysis

3. RESULTS AND DISCUSSION

Tensile Tests

The tensile curves obtained for E355+N and S355JR+N material as a result of tensile tests are shown in Figure 13 and specific points of curves are given in Table 2.

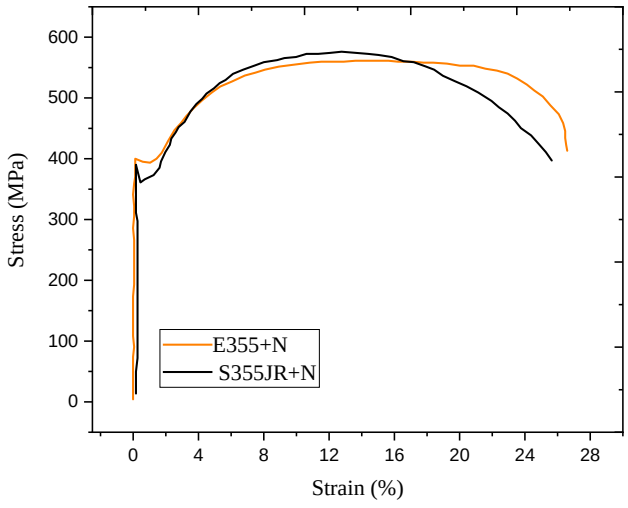

Figure 13. E355+N and S355JR+N materials tensile test curves

Table 2. Tensile test results of E355+N and S355JR+N materials

	Sample Type	Yield Stress (MPa)	Max Stress (MPa)	Elongation (%)
E355+N	Pipe	393.42	560.91	26.59
S355JR+N	Bar	392.52	575.60	25.64

It has been observed that the yield and tensile strength values obtained from the tensile tests are very close to each other. The differences between the values are negligible. Accordingly, it was concluded that S355JR+N material can be used to determine the fatigue behavior of the drag link pipe material.

Material Fatigue Tests

The stress-cycle number (S-N) curves of the unprestrained (0%) and strained (12%) S355JR+N samples are shown in Figure 14. It is seen that the specimens subjected to pre-strain show better fatigue resistance. Higher pre-strain applied material undergoes more plastic deformation. Thus, it shows a higher yield strength feature. In addition, using the interpolation method between 0% and 12% curves, a curve with 6% pre-strain was created.

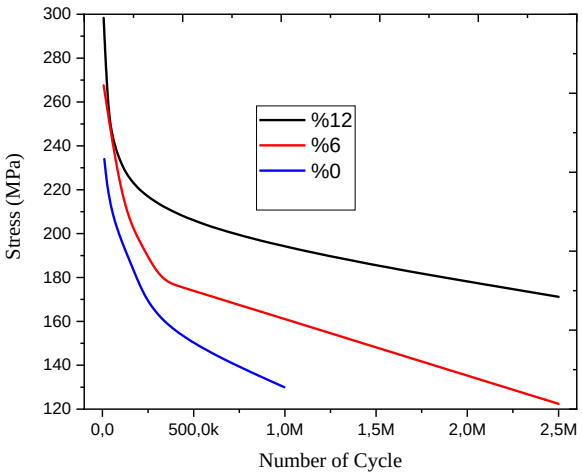

Figure 14. S-N curves of S355JR+N specimens with prestrain level of %0,%6 and %12

Drag Links Fatigue Tests

The tests were continued until the target value of 1.000.000 cycles, which is accepted as infinite life in drag link fatigue tests. The test conditions and test results applied to the drag links are shown in Table 3. It was observed that the drag links that could not reach the target value were damaged by cracking from the inner walls of the bending areas.

Table 3. Drag links experimental fatigue test results

Part No	Fatigue Load (kN)	Frequency (Hz)	Cycle Number	Result
1	20	5	1.000.000	No damage
2	20	5	1.000.000	No damage
3	25	5	449.515	Broken from the bend
4	25	5	524.212	Broken from the bend

Bending Process Simulation

During the bending analysis, pipe bending was ensured by making the bending mold make a translational movement in the vertical direction of 35 mm in the first 3 steps, and the pipe was released by pulling in the opposite direction in the last two steps. As a result of the analysis, approximately 12% plastic deformation was observed in the inner and outer walls of the bend region as seen in Figures 15 and 16 in the pipe bend region. Accordingly, fatigue tests were carried out by applying 12% pre-strain to 10 of the samples produced for the fatigue test of S355JR+N material.

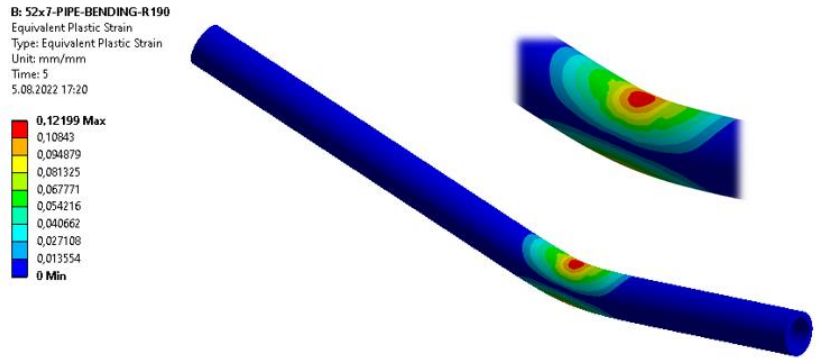

Figure 15. Plastic deformation distribution of the bending inner wall after bending

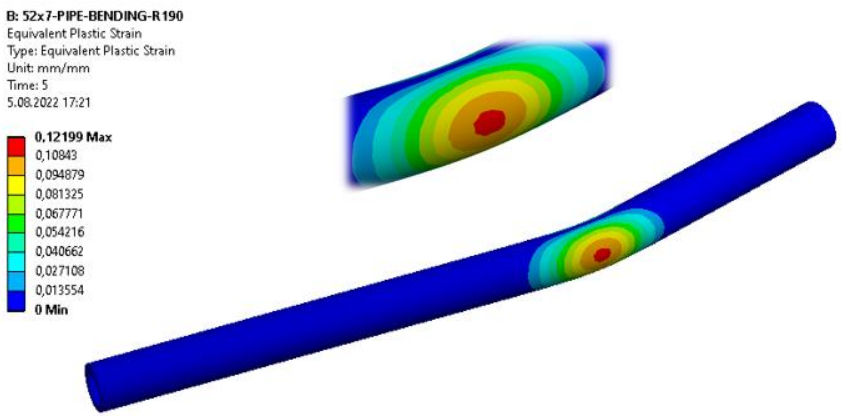

Figure 16. Plastic deformation distribution of the bending outer wall after bending

Drag Links Fatigue Simulation

As a result of the analysis, it was seen that the drag link without pre-strain and the FGM model, which were analyzed at different load values, were damaged at the bending points. It was observed that while the drag link with 0% pre-strain provided the target 1.000.000 cycles at 14 kN load value, the functional graded drag link reached the target 1.000.000 cycles at 20 kN.

Figure 17 shows the stress condition at 14 kN load value for the model with 0% strain. The maximum stress occurred as 129.12 MPa on the inner wall of the bending zone.

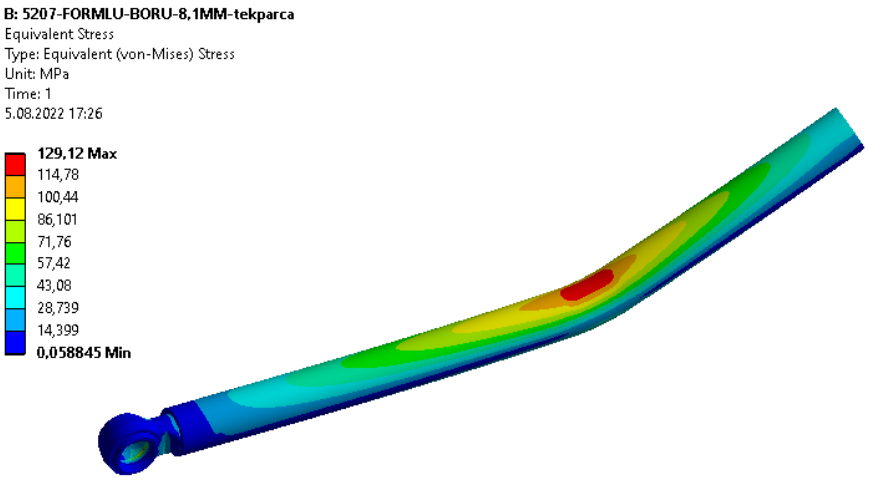

Figure 17. Stress state of the drag link at 14 kN load value

In Figure 18, the life distribution of the drag link with a 14 kN load applied in terms of number of cycles for the model with 0% pre-strain is shown. The part reaches the target number of 1,000,000 cycles at this load value. Each point on the part provides the target cycle number value.

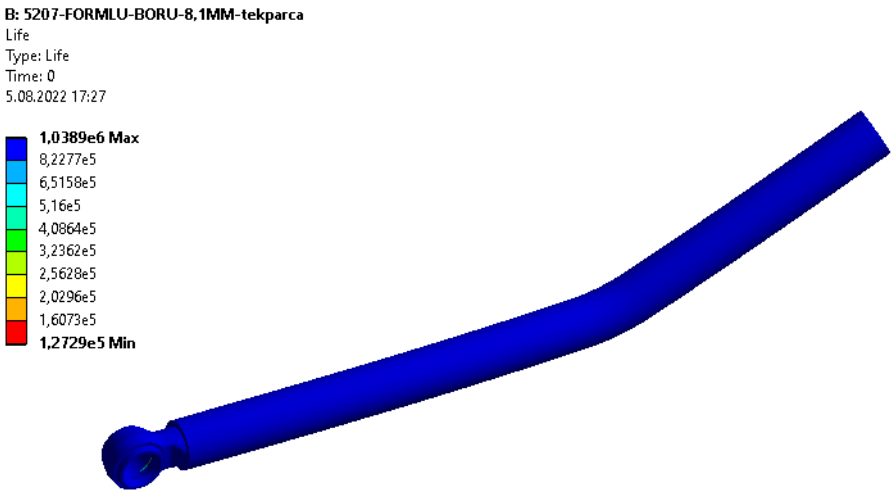

Figure 18. Cycle number distribution of drag link at 14 kN

Fatigue analysis was performed at 20, 22 and 25 kN load values for the drag link modeled as FGM. It has been observed that the drag link at a load of 20 kN provides the targeted 1.000.000 cycles.

Figure 19 shows the stress state occurring at a load of 20 KN. The maximum stress was 179.45 MPa on the inner wall of the bending zone.

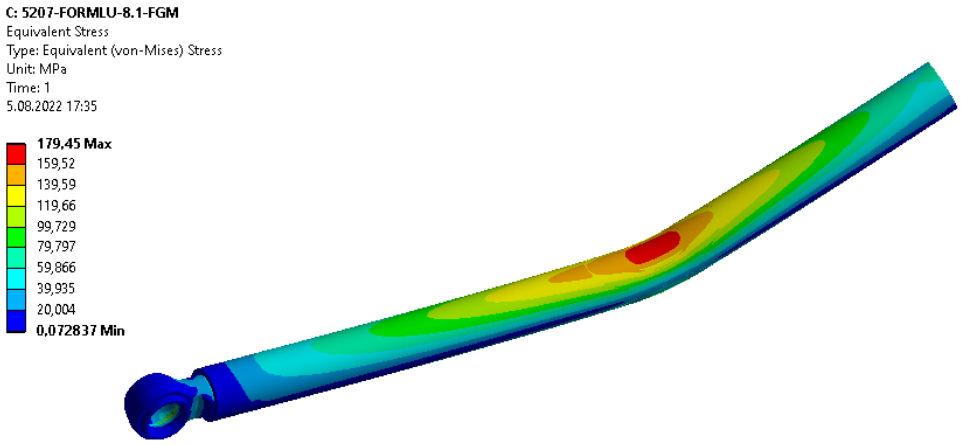

Figure 19. Cycle number distribution of drag link at 20 kN

Figure 20 shows the life distribution of the drag link with 20 kN load in terms of number of cycles. The part has more than 1.000.000 cycles targeted. Each point on the part provides the target cycle number value. The drag link modeled as a single piece provides 1.000.000 cycles at 14 kN, while the drag link modeled as FGM provides more than 1.000.000 cycles at 20 kN.

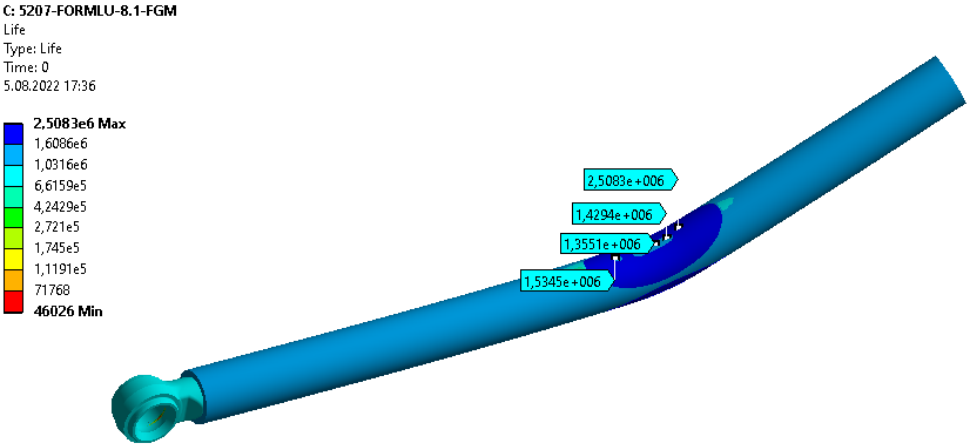

Figure 20. Cycle number distribution of drag link at 20 kN

Table 4 shows the conditions and results of the drag links fatigue analysis, which is assumed to have no pre-strain, functional graded drag link fatigue analysis with pre-strain, and the experimental drag link fatigue test. According to the results obtained, it was seen that the functional graded model, which was created by considering the pre-strain, showed better fatigue behavior and closer to the experimental results than the model without pre-strain. According to the analysis results, there is a significant difference between the fatigue behavior of the drag link model modeled as FGM and the drag link model modeled as one piece.

Table 4. FEA and experimental fatigue results according to pre-strain condition

Force (kN)	Cycle Number For No Prestrained Model (FEA)	Cycle Number For FGM Model (FEA)	Average Cycle Number (Experimental)
14	1.000.000		
16	650.520		
18			
20	98.227	1.355.100	1.000.000 (No damage)
22		512.860	
25		138.180	486.863 (Broken from the bend)

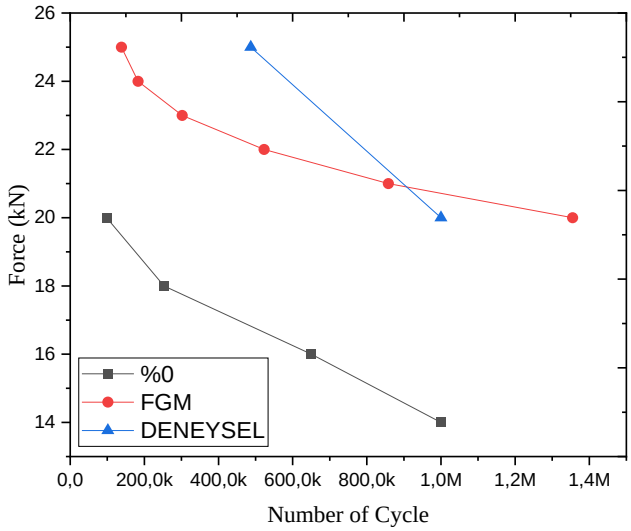

Figure 21. FEA according to the pre-strain condition and experimental test results curves

4. CONCLUSION

In this study, the effect of plastic deformation occurring during drag link bending on fatigue behavior was investigated. Tensile and fatigue tests for the drag link material and fatigue tests of the drag links were carried out. In addition, drag link bending process and fatigue tests are simulated in the finite element analysis environment. The results obtained are listed below:

- The tensile test results of E355+N pipe material and S355JR+N material in equivalent filled form were very close to each other. The differences between the results are negligible. It has been observed that S355JR+N material can be used for the fatigue behavior of the drag link pipe material.
- It was observed that specimens with pre-strain showed better fatigue behavior than specimens without pre-strain.
- According to the finite element fatigue analysis, it was observed that the functionally graded drag link showed better fatigue behavior than the drag link model modeled as a single piece without taking into account the deformation, and the functionally graded model results were closer to the experimental results. By dividing the functionally graded model into more sub-models, it is possible to obtain results closer to the real values.

SIMILARTY RATE: 6%

REFERENCES

[1] J.A. Bannantine, J.J. Comer, and J.L. Handrock, *"Fundamentals of Metal Fatigue Analysis"*, Prentice Hall, New Jersey, 1989.
[2] B. Koca, and B. Ekici, "Fatigue life prediction of a drag link by using finite element method", The ASME 2010 10th Biennial Conference on Engineering Systems Design and Analysis, Istanbul, Turkey, p.1-7, 12-14 July 2010.
[3] B. Das, A. Singh, K.S. Arora, M. Shome, and S.K. Paul, "Influence of pre-straining path on high cycle fatigue performance of DP 600 steel", *International Journal of Fatigue* 126, 369-380, 2019.
[4] S. Koh, and T. Baek, "Fatigue life prediction of an automotive steering drag link", International Conference on Advanced Technology in Experimental Mechanics, Fukuoka, Japan, s.18-22, 12-14 September 2007.
[5] Y.S. Lee, J.S. Lim, Y.N. Kwon, and Y.H. Moon, "Fatigue characteristics of small radius pipe fabricated by pipe bending with induction local heating", *Procedia Engineering* 10, 3333-3338, 2011.
[6] I.N. Budak, and M. Pekedis, "Plastik şekil değişimine uğramış otomobil rotunun yorulma davranışının deneysel ve sayısal analizi", *Dokuz Eylül Üniversitesi Mühendislik Fakültesi Fen ve Mühendislik Dergisi* 23 (68), 647-659, 2021.
[7] E. Uludamar, S.G. Biçer, and M. Taş, "Sonlu elemanlar metodu kullanılarak rot üzerinde oluşan gerilmelerin hesaplanması", *Adana Bilim ve Teknoloji Üniversitesi Fen Bilimleri Dergisi* 1(2), 30-35, Aralık 2018.
[8] A.H. Falah, M.A. Alfares, and A.H. Elkholy, "Failure investigation of a tie rod end of an automobile steering system", *Engineering Failure Analysis* 14, 895–902, 2007.
[9] M.A. Güvenç, and F.M. Botsalı, "Rot başı Yorulma Ömrünün Bilgisayar Destekli Mühendislik Araçları Kullanılarak Tahmin Edilmesi", Uluslararası Katılımlı 17. Makina Teorisi Sempozyumu, İzmir, 14-17 Haziran 2015.
[10] J. Peng, K. Li, Q. Dai, and J. Peng, "Mechanical properties of pre-strained austenitic stainless steel from the view of energy density", *Results in Physics* 10, 187–193, 2018.
[11] S. PM, S. Gawade, and S.S. Kelkar, "CAE Analysis and Structural Optimization of PitmanArm", *International Engineering Research Journal*, p. 1-5, 2015.
[12] TS EN 10305-1, Çelik Borular, Hassas Uygulamalar İçin Teknik Teslim Şartları, Bölüm 1: Soğuk Çekilmiş Dikişsiz Borular, Türk Standartları Enstitüsü, Ankara, 2012.
[13] TS EN 10025-2, Sıcak Haddelenmiş Yapı Çelikleri-Bölüm 2: Alaşımsız Yapı Çeliklerinin Genel Teknik Teslim Şartları, Ankara, 2006.
[14] S. Toros, and K. Altinel, "Contribution of functionally graded material modelling on finite element simulation of rod end parts in automotive steering system", *Journal of Mechanical Science and Technology* 30(7), 3137-3141, 2016.

Eurasian Journal of Science Engineering and Technology

Research

A CASE STUDY ON COST ANALYSIS AND LOAD ESTIMATION OF HYBRID RENEWABLE ENERGY SYSTEM USING HOMER PRO

Saba MUNIR[1,*], Ausnain NAVEED[2], Raja Tahir IQBAL[3], Mohtasim USMAN[4]

[1,2,3,4] *University of Azad Jammu and Kashmir, Department of Electrical Engineering, Muzaffarabad, Pakistan*

ABSTRACT

Pakistan is facing serious energy deficiency issues. Moreover, emission of polluted gases must be minimized to reduce the air pollution. The emission of harmful gases can be lessened by the implementation of renewable energy resources. Such issues can be curtailed through proper planning on national and gross root level. In this study, load estimation and cost analysis for the installation of optimized hybrid model of renewable energy resources in electrical engineering department of University of Azad Jammu & Kashmir has been presented. In order to analyze load and estimate the cost, different scenarios are generated on Hybrid Optimization Model for Electric Renewables (HOMER) Pro software. On the basis of these scenarios, the system having less cost of energy and emission of polluted gases is proposed as the optimal system to power the department.

Keywords: Cost analysis, HOMER Pro, Load estimation, Renewable energy

1. INTRODUCTION

The world is switching to Renewable Energy (RE) due to the fossils depletion and cost-competitive solutions. Also, the innovation in renewable energy technologies allows to combine different RE sources and produce electricity. These RE sources consist of solar energy, tidal energy, wind power, geothermal, micro-hydropower and biomass [1]. Energy intake is intensely inclined to the latest global trade and the fast-growing industry. Global population growth is another issue contributing towards the surge in energy consumption [2]. Typically, most of human energy needs are met from non-renewable energy sources like fossil fuels. However, there are two main problems with growing dependence on fossil fuels to meet energy demand; loss of fossil fuels and rising carbon dioxide emissions which is a major cause of increase in global warming [3]. In Pakistan, power outage is a major problem that is often addressed by conventional production [4]. The economic and technical feasibility analysis for the operation of the conventional and a new hybrid system is presented in [5]. Two micro grid systems were evaluated on the economic aspect in which one was dependent and other was independent. The analysis shows that for interconnected system, the installation of photovoltaic cell and the wind turbines are more effective. In [6], an economic analysis of a standalone hybrid power system for application in Tehran has been presented. The study shows the incident solar radiation, equipment characteristics, electric load profile, and hydrogen fuel design parameters of a hybrid power system. Another work presented in [7] shows that the on grid system is more economic as compared to the off grid system because extra amount of batteries need to be used in the off grid system. Based on solar radiation, a similar study explained the technical feasibility of a standalone system that meets the 2.5% load requirement of the city of Mecca using Homer Pro [8]. A feasibility analysis of wind, solar or hybrid system performance in the west coast of Saudi Arabia is presented [9] where the potential of hybrid energy system in that region was evaluated. A hybrid optimization model of RE resources used to design a small grid at remote sites, islands, on grid and off grid systems where these resources can be used as a mix and or as an independent source to meet power shortages is presented in [10]. The proposed model is analyzed by using Homer Grid. Changing cost of fuel and the atmospheric hazards are the key factors in the study to stimulate the use of RE resources for generating power.

In this work cost analysis and load estimation for the Department of Electrical Engineering (DEE) in University of Azad Jammu and Kashmir (UAJ&K) has been done. DEE is an educational institute which operate five days a week. The average working hours of DEE is 8 hours and the department fulfills its demand through grid. Whereas, a generator of 25KW is used to fulfill the load requirement during the load shedding hours. Given the fact, cost of the existing system is very high which can be lessened by using renewable energy resources. However, it requires proper load and economic assessment. The software which is used for this work is HOMER Pro 3.14 software. The reason for choosing this software is that this software efficiently performs three types of working; optimization, sensitivity analysis and simulation. Moreover, the software defines the quantity of the components, thus, making it easy to find the best optimal result for the system.

* Corresponding author, e-mail: sabamunir298@gmail.com (S. Munir)
Recieved: 28.04.2022 Accepted: 25.11.2022
doi: 10.55696/ejset.1110275

2. CASE STUDY

Pakistan is facing serious energy deficiency issues which can be resolved easily through proper planning. The country's vision of clean and green Pakistan strives for minimum emission of polluted gases to reduce air pollution. Power obtained through conventional sources is also a reason for emission of harmful gases. This emission of harmful gases can be minimized by generating power through RE resources.

In this study, load estimation and cost analysis of DEE located in UAJ&K has been studied. Different scenarios are generated on a clean energy software known as HOMER PRO for the feasibility study of hybrid RE generation. The software is used to analyze and perform the cost analysis on the system. Various gird connected configurations of the system are also studied and on the basis of generated scenarios, the optimal result is find out for the system. The system having low cost of energy is defined as the best system. Moreover, emission of polluted gases is also taken into account where the best solution reduces the harmful emission of gases.

2.1 Existing system

The existing system of the department consists of a grid supply and a backup generator. The power demand is met through grid and a 25 kW generator is used to meet the load demand during power curtailment hours. The department has constant load of 15kW for 8 hours in a day. Since the department works for 8 hours 5 days a week, hence, a constant load curve for all the weekdays can be seen in Figure 1 for a better understanding of load estimation. System model of the existing system has been shown in Figure 2. The Cost of Energy (CoE) is $0.287, whereas, the Initial Capital Cost is $30,000 and the Net Present Cost (NPC) is $90,090M. Most importantly, the Carbon Emission of the existing system is 16,069 Kg/yr with a Fuel Rate of 661 L shown in Figure 3.

3. PROPOSED SYSTEM

A combination of renewable energy sources has been employed in the proposed system. Cost and load analysis was done on all combinations. The optimal plan is evaluated based on these costs and load analysis. Energy Costs and Current Costs are considered and based on these costs the greatest effect is obtained. The arrangement of low energy costs is considered the appropriate system.

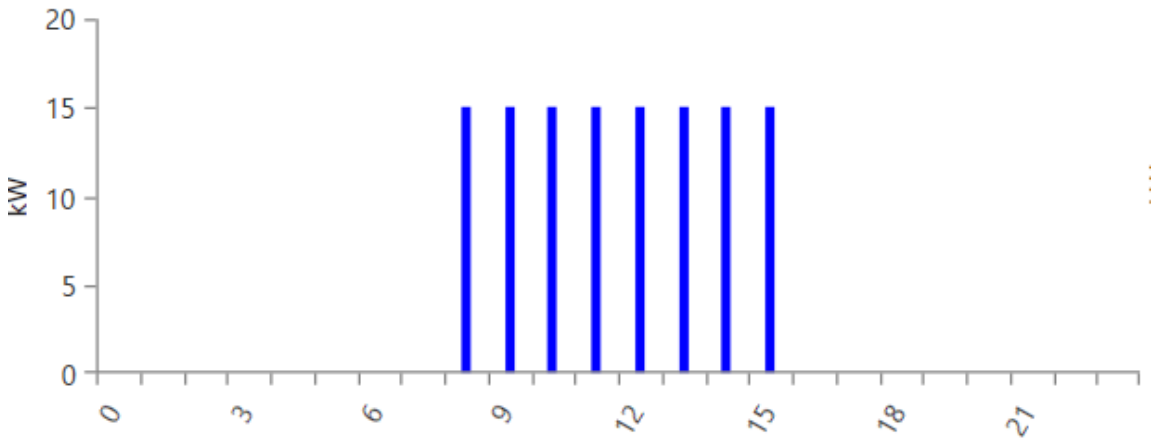

Figure 1: Daily load profile of existing system

A CASE STUDY ON COST ANALYSIS AND LOAD ESTIMATION OF HYBRID RENEWABLE ENERGY SYSTEM USING HOMER PRO

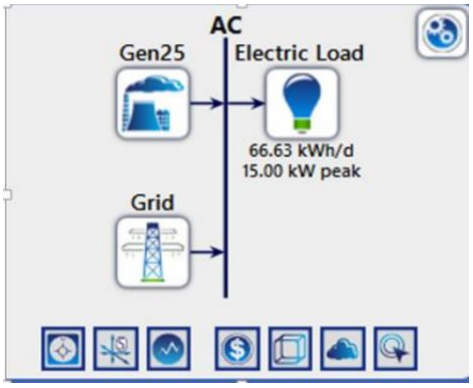

Figure 2: Schematic of existing system

Gen25 (kW)	Grid (kW)	Dispatch	COE ($)	NPC ($)	Operating cost ($)	Initial capital ($)	Hours	Production (kWh)	Fuel (L)
25.0	999,999	CC	$0.287	$90,090	$4,648	$30,000	261	1,631	661

Figure 3: Cost estimation of existing system

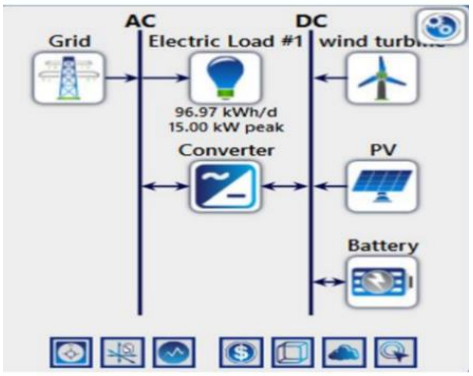

Figure 4: System model of scenario 1

Table 1: Configuration of system for Scenario 1

Storage	PV	Wind	Grid
5 batteries	20KW	20KW	Unlimited

PV (kW)	wind turbine	Battery	Grid (kW)	Converter (kW)	Dispatch	COE ($)	NPC ($)	Operating cost ($)	Initial capital ($)	Ren Frac (%)	Capital Cost ($)	Production (kWh)
20.0	20	1	999,999	20.0	CC	-$0.0344	-$28,171	-$3,394	$15,700	92.1	7,000	33,871

Figure 5: Cost estimation of scenario 1

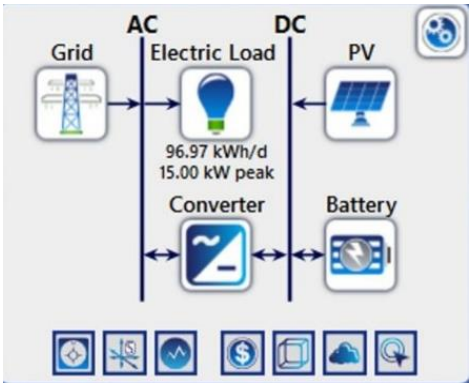

Figure 6: System model of scenario 2

Table 2: Configuration of system for Scenario 2

Storage	PV	Grid
5 batteries	20KW	Unlimited

PV (kW)	wind turbine	Battery	Grid (kW)	Converter (kW)	Dispatch	COE ($)	NPC ($)	Operating cost ($)	Initial capital ($)	Ren Frac (%)	Capital Cost ($)	Production (kWh)
20.0		1	999,999	17.2	CC	$0.0384	$21,083	$768.61	$11,146	77.9	7,000	33,871

Figure 7: Cost analysis of scenario 2

3.1. Scenario 1 (PV, Wind, Grid, Battery Storage)

System model for this scenario is shown in Figure 4 and the specification of this scenario are given in Table 1. It can be observed that Scenario 1 comprises of PV, wind, battery and grid. Here two buses are present; AC and DC buses. Converter, wind, and load are connected to the AC bus, whereas, PV and battery storage are connected to the DC bus. It should be noticed in Figure 5 that the CoE of Scenario 1 is $0.0344, the NPC is $28,171M and initial capital cost is $15,700M. However, the carbon emission rate is -14,510 kg/yr which is very low.

3.2. Scenario 2 (PV, Battery Storage, Grid)

System model for this scenario is illustrated in Figure 6 and the arrangement of this scenario are given in Table 2. It can be observed that Scenario 2 contains a combination of PV, Grid and Battery Storage installed together. Similar to Scenario 1, AC and DC buses are involved in this scenario as well. Grid, Load and Converter is connected with AC bus whereas PV and Storage is connected with DC bus. It can be observed from Figure 7 that the CoE for Scenario 2 is $0.0384 and the NPC is $21,083M. Although, the initial capital cost is $11,146M, but, the carbon emission rate is 14,27kg/yr.

3.3 Scenario 3 (Grid, Battery Storage, Wind)

System model for this scenario is presented in Figure 8 and the specification of this scenario are mentioned in Table 3. It can be observed that Scenario 2 consists of conventional grid, battery storage and wind. Here, again two buses are being used; grid, electric load and converter are connected to the AC bus and wind turbine along with battery storage is connected to the DC bus. As shown in Figure 9, the CoE for Scenario 3 is $0.0365, the NPC is $25,182M and Initial Capital Cost is $8,554. However, the carbon emission rate is 3.31kg/yr which is lesser than Scenario 2 but higher than Scenario 1.

A detailed comparison of the existing system and all the three scenarios is presented in Table 4. It should be observed that the existing system has a high energy cost when compared with all the three proposed scenarios. However, the CoE of scenario 1 is the lowest among all the three scenarios which is $0.0344. Also, the carbon emission rate of the existing system is very high when compared with all the three posed scenarios. Whereas, this rate is minimum for Scenario 1 which is the biggest persuasion to adopt this system.

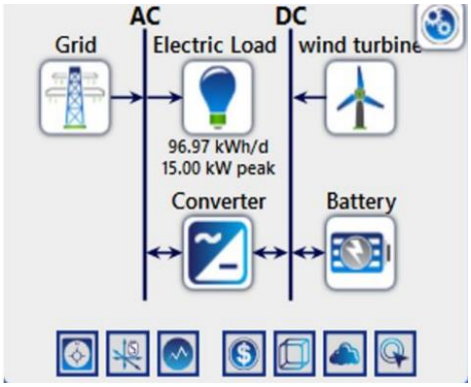

Figure 8: System model of scenario 3

Table 3: Configuration of system for scenario 3

Grid	PV	Load
Unlimited	20KW	15KW

PV (kW)	wind turbine	Battery	Grid (kW)	Converter (kW)	Dispatch	COE ($)	NPC ($)	Operating cost ($)	Initial capital ($)	Ren Frac (%)
	20	1	999,999	19.3	CC	$0.0365	$25,182	$1,286	$8,554	56.3

Figure 9: Cost estimation of Scenario 3

Table 4: Comparison of cost for all scenarios

	INITIAL CAPITAL COST	NET PRESENT COST	CARBON EMISSION	COST OF ENERGY
EXISTING SYSTEM	$30,000	$ 90,090M	16,069 (Kg/year)	$0.287
SCENARIO 1	**$15,700**	**$28,171M**	**-14,510 (Kg/year)**	**$0.0344**
SCENARIO 2	$11,146	$21,083M	1,427 (Kg/year)	$0.0384
SCENARIO 3	$8,554	$25,182M	3,351(Kg/year)	$0.0365

4. CONCLUSION

The DEE in UAJ&K is operated by using grid and diesel generator. This existing system has a very high carbon emission rate which is not aligned with the energy policy of the country. Moreover, the CoE or in other words the average of NPC of electricity generation of the existing system is very high. Also, the generator is being used to supply power during the load shedding hours, but, diesel itself is a very high priced commodity. Therefore, a cost effective solution given in shape of Scenario 1 should be adopted that is capable of reducing the CoE from **$0.287** to **$0.0344,** which means CoE decreases **88.0139%.**

SIMILARTY RATE: 12%

ACKNOWLEDGEMENT

The authors acknowledge the support of the technical staff of University of Azad Jammu & Kashmir to provide the required information.

REFERENCES

[1] R. Hidalgo-Leon, F. Amoroso, J Litardo, et al., "Impact of the Reduction of Diesel Fuel Subsidy in the Design of an Off-Grid Hybrid Power System: A Case Study of the Bellavista Community in Ecuador," Energies, vol. 14, no. 6, pp. 1730, 2021.

[2] F.A. Alturki and A.B. Dayil, "Techno-Economic Evaluation and Optimization of Grid Connected PV and Wind Generating System for Riyadh City," International journal of power and energy engineering, vol. 8, no. 12, pp. 46-63, 2020.

[3] S. Kumar, C.P. Sethuraman and C. Gopi, "Sizing Optimization and Techno-Economic Analysis of a Hybrid Renewable Energy System Using HOMER Pro Simulation," Journal of Scientific and Industrial Research, vol. 80, no. 09, pp. 777-784, 2021.

[4] R. Hidalgo, P. Jacome, J. Urquizo and G. Soriano, "Microgrid design for remote location in chile using a scenario-based methodology," In Proceedings of the 14th LACCEI International Multi-Conference for Engineering, Education, and Technology: Engineering Innovations for Global Sustainability, Boca Raton, FL, USA, pp. 20-22, July, 2016.

[5] M.A.H. Mondal and A.S. Islam, "Techno-economic feasibility of grid connected solar PV system in Bangladesh," In Proceedings of 2009 IEEE 1st International Conference on the Developments in Renewable Energy Technology (ICDRET), Dhaka, Bangladesh, pp. 1-4, 2009.

[6] F. Fazelpour, N. Soltani and M.A. Rosen, "Wind resource assessment and wind power potential for the city of Ardabil, Iran," International Journal of Energy and Environmental Engineering, vol. 6, no. 4, pp. 431-438, 2015.

[7] P. Iqra, S.R. Abdul, et al., "Designing off grid and on grid Renewable Energy System Using Homer Pro Software. Environment Engineering and Management Institute, MUET Jamshoro Pakistan," Journal of International Environmental Application and Science, vol. 12, no. 4, pp. 270-276, 2017.

[8] M. Anwari and A. Hiendro, "Performance Analysis of Pv Energy System in Western Region of Saudi Arabia," *Engineering*. 2013; vol.5, no.1, pp.62-65.

[9] M.A. Ramli, A. Hiendro, and Y.A. Al-Turki, "Techno-economic energy analysis of wind/solar hybrid system: Case study for western coastal area of Saudi Arabia," Renewable Energy, vol. 91, pp. 374-38, 2016.

[10] M. Kamran, M. Mudassar, M. Bilal and M. Shahid, "Techno-Economic Analysis of Distributed Generation for Microgrid Application Using HOMER Pro," International Journal of Emerging Technology and Advanced Engineering, vol. 5, no. **7**, pp. 272-279, 2015.

Eurasian Journal of Science Engineering and Technology

Research Article

THE INFLUENCE OF POST-ANNEALING CdS THIN FILMS GROWN ON ZnO SEED LAYER FOR CdTe SOLAR CELLS

Ali ÇİRİŞ[1*]

[1*] *Niğde Ömer Halisdemir University, Nanotechnology Application and Research Center, 51240, Niğde, Türkiye*

ABSTRACT

In this study, the effect of post-annealing temperature in CdS thin films grown on ZnO seed layer was investigated. CdS thin film and ZnO seed layer were coated by chemical bath deposition method and solution dropping technique, respectively. The structure of the post-annealed samples at 350°C and 400°C consisted of cubic CdS and $CdSO_3$ oxide phases. As a result of recrystallization at 450°C, both hexagonal CdS and cubic CdO phases were formed. While the absorption edge was observed at around 500 nm in all samples, the best transmittance was observed in the sample annealed at 400°C. PL spectra proved the existence of defect types such as deep emission, sulfur vacancy for all samples. Ellipsometer measurements showed that the highest refractive index was in the sample annealed at 400°C. Among the samples, it was concluded that the most suitable window structure for CdTe solar cell applications is CdS thin film post-annealed at 400°C.

Keywords: CdS, ZnO seed layer, CBD, post-annealing temperature

1. INTRODUCTION

In CdTe based solar cells, CdS thin films are conventionally used as n-type junction partners [1, 2]. CdS stands out with its surpassing features such as suitable band gap (~2.4 eV), high photoconductivity, low absorbance and high optical transmittance required for high performance photovoltaic devices [3, 4]. CdS can be grown by many methods such as vacuum evaporation [5, 6], spray pyrolysis [7, 8], close space sublimation [9, 10], RF sputtering [11, 12] and chemical bath deposition (CBD) [13, 14]. However, CdS layer in high efficient CdTe cells is usually grown by CBD method due to the possibility of recrystallization and alloying [15-17]. CBD method provides advantages such as repeatable and controlled process management, adjustable parameters (bath temperature, source concentration, etc.), simple and low cost production [18, 19]. However, problems such as low adhesion, non-uniformity, inhomogeneity may be encountered in the film growth process with CBD [20]. One of the ways to overcome these problems is to change the film growth parameters such as bath temperature, stoichiometry (cadmium/sulfur ratio), the amount of a complexing agent, etc. These changes in the film growth parameters in CBD method directly affect the reaction properties. In this sense, it was deduced that this parameters had a significant effect on the properties such as the crystal structure, grain structure, homogeneity, band gap, transmittance, carrier concentration and resistivity [21-27].

Although these adjustments in growth parameters seriously affect the properties of the films, there are still some difficulties with the desired film quality. In this context, growing CdS thin films onto a seed layer may be a solution to improve film properties. Due to poor quality of film growth, the seed layer plays especially an effective role in the improvement of low adhesion and nucleation [28]. Among the many materials used as seed layer, one of the most suitable for CdS thin films is ZnO. Growing CdS thin films on ZnO seed layer may provide a substructure to advance film properties. However, due to the amorphous nature of CdS deposited by CBD method, an extra processing is needed to improve the crystalline and morphological properties. In this direction, one of the most proper option is heat treatment. The annealing process leads to many effects such as increasing the crystal quality of the films, phase transformation, improving the grain structure, progressing of the optical and electrical properties [29-31].

Considering all aspects, it is thought that depositing CdS thin film on a seed layer followed by heat treatment is an effective process to develop the characteristics of CdS. In this sense, the effect of post-annealing on the structural and optical properties of CdS thin films coated on ZnO seed layer was investigated in this study. For this purpose, post-annealing temperatures ranging from 350°C to 450°C were used.

* Corresponding author, e-mail: aliciris@ohu.edu.tr (A. Ciriş)
Recieved: 26.10.2022 Accepted: 28.11.2022
doi: 10.55696/ejset.1194810

2. MATERIAL AND METHOD

In order to search the effect of post-annealing temperature on CdS thin films grown on ZnO seed layer, the samples were coated on soda lime glass (SLG) substrates. Before coating ZnO seed layer, the SLG substrates were cleaned with acetone, isopropanol and de-ionized water in an ultrasonic bath. Then, ZnO seed layer was grown on the SLG substrates. The solution of ZnO seed layer was prepared using 5 mM zinc acetate dehydrate [$Zn(OOCCH_3)_2$] in absolute ethanol. 1 drop/cm^2 volume of the solution was dropped onto the substrates, and the surface was dried with N_2 gas after dwell time for 20 s. This operation was repeated eight times. After ZnO seeding, the prepared samples were annealed at 350°C for 30 min at air atmosphere [32]. CdS thin films with CBD method were grown using with a mixture of 15 mM $3CdSO_4.8H_2O$, 1.5 M thiourea and 28-30% ammonia hydroxide at a bath temperature of 80°C [33]. The thickness of CdS was set to 50-60 nm for a deposition time of 10 min. The samples were post-annealed for 20 minutes in air atmosphere at temperatures of 350°C, 400°C and 450°C. The prepared samples with post-annealing are schematically shown in Figure 1. In the whole text, labels were used to describe the samples. For example, label ZC-400 refers to the sample post-annealed at 400°C after the CdS thin film is grown upon ZnO seed layer.

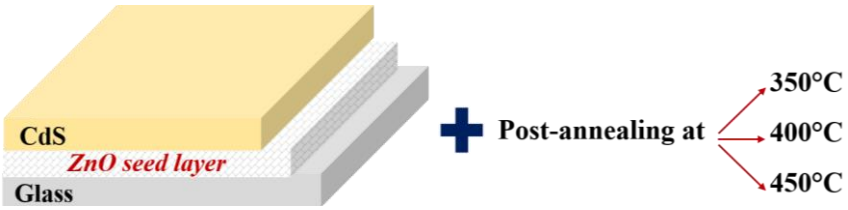

Figure 1. Schematic configuration of CdS samples grown on ZnO seed layer annealed at different temperatures

The crystallinity properties of the samples were analyzed with XRD spectra measured by Rigaku Smartlab diffractometer using CuK_α radiation. Transmittance curves were obtained using Dongwoo Optron UV-Vis spectrophotometer in the wavelength range of 300-1000 nm. Photoluminescence measurements at room temperature (RTPL) were performed with SpectraMax M5 at excitation wavelength of 280 nm. Refractive indexes was measured by J.A.Woollam spectroscopic ellipsometer.

3. RESULTS AND DISCUSSION

The XRD spectra of the samples post-annealed at 350°C, 400°C and 450°C are shown in Figure 2. As seen in Figure, there are overlapping and shouldering peaks in the diffraction patterns of the samples. To detect these peaks, the deconvolution process was applied to the spectrum of each sample. The peaks clarified by the deconvolution are also seen in the Figure. It was observed that the samples annealed at 350°C and 400°C had similar XRD spectra. According to the peak positions in the spectra, (111), (220) and (311) planes of CdS crystallizing in cubic structure were formed at 350°C and 400°C (Card No: 00-010-0454). In addition, $CdSO_3$ oxide phase was also formed in these samples (Card No: 01-078-1474). However, it was observed that the effect/intense of the oxide phase decreased at 400°C. Besides, the increase in post-annealing temperature from 350°C to 400°C led to an improvement from 8.8 nm to 9.8 nm in crystallite size calculated by Scherrer formula [34] based on the main peak of CdS.

In the deconvolution results of the sample post-annealed at 450°C, it was observed that the crystal structure of CdS phase transformed from cubic to hexagonal structure. In the spectrum, it was determined that (100), (002), (101), (110), (103) and (112) planes of hexagonal CdS were formed, respectively (Card No: 00-041-1049). In addition, it was detected that the (111), (200) and (220) planes of CdO phase crystallized in the cubic structure also exist in the crystalline structure of the sample (Card No: 00-005-0640).

Comparing of the XRD results showed that the samples at 350°C and 400°C had a similar crystal structure. However, as the post-annealing temperature increased to 450°C, the crystal structure of the sample underwent a radical change that CdS phase changed from cubic to hexagonal and that extra cubic CdO phase was formed. It was concluded that temperatures up to 400°C are not a high enough for recrystallization of the sample structure, but a temperature of 450°C is enough to drive the crystalline nature of the sample into a new formation. Besides, when the crystallization quality of the samples is examined, it can be said that ZnO seed layer improves the crystallization and allows more specific peaks to be revealed. Because it is known that CdS has nano-amorphic nature and may not cause a distinct change in crystallization even if heat treatment is applied at high temperatures. However, in our samples, the crystal structure of CdS was clearly determined with the support of the deconvolution process. This shows that the ZnO seed layer provides an infrastructure to grow higher quality films, in accordance with its purpose.

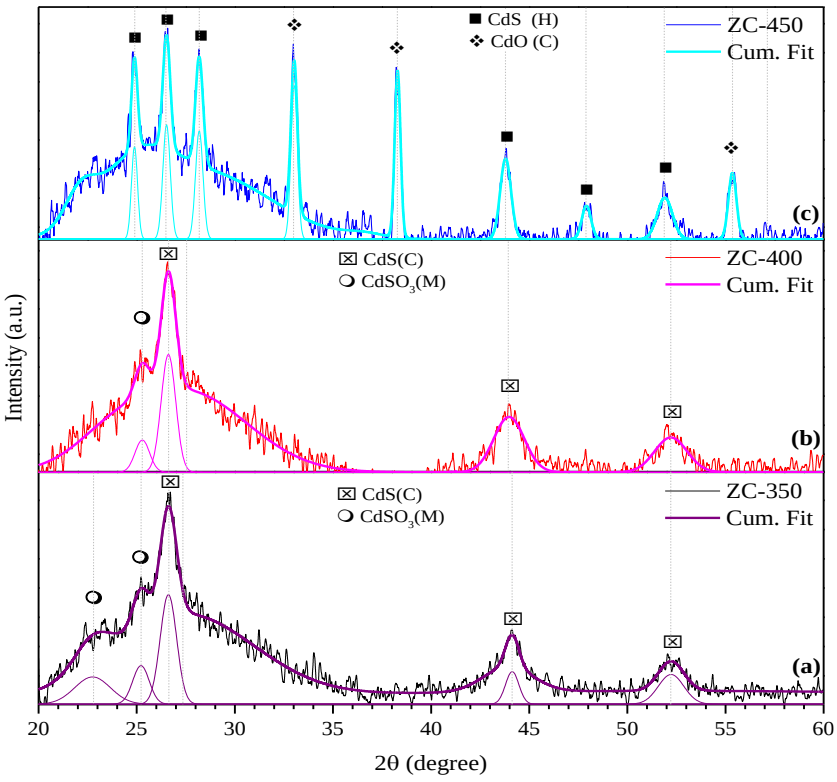

Figure 2. XRD spectra and corresponding deconvolution results of the samples post-annealed at **a)** 350°C, **b)** 400°C and **c)** 450°C (C, H and M in parentheses refer to cubic, hexagonal and monoclinic, respectively)

The transmittance curves of the samples between 300-1000 nm are shown in Figure 3. In the transmittance curves, it is seen that all samples have an absorption edge of around 500 nm, corresponding to CdS. In the wavelength region greater than 500 nm, the transmittance varied between 65% and 85% (at wavelength of 850 nm). Herein, it has the lowest transmittance to the sample post-annealed at 350°C. Increasing the annealing temperature to 400°C caused a 20% increase in the transmittance of the sample, resulting in transmittance of 85%. It can be said that this increment is due to the improvement in the crystallization at 400°C. However, the annealing temperature at 450°C led to a significant decrease in the transmittance. This reduction confirmed with the XRD results which showed that annealing at 450°C caused a serious change in the crystal structure of the sample.

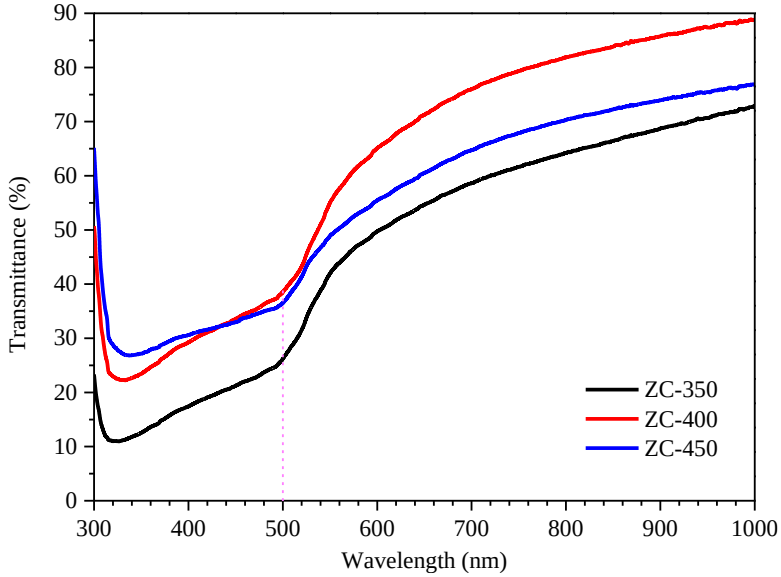

Figure 3. Transmittance curves of the samples post-annealed at 350°C, 400°C and 450°C

Room temperature photoluminescence (PL) spectra and corresponding deconvolution results of the samples post-annealed at 350°C, 400°C and 450°C are shown in Figure 4. When the figure is examined, it is seen that the samples have similar PL spectra. According to the deconvolution results, it was revealed that there were PL emission peaks around 360, 420, 443, 481-485, 530-535 (except 450°C) and 567 nm in all samples. The emission at 360 nm is attributed to transitions from deep levels to shallow levels, while the peak at 420 nm corresponds to the band edge emission [35, 36]. The emission at 443 nm is related to band-edge emission from radiative recombination of excitons [37], while the range of 481-485 nm is associated with host CdS [38]. The peaks around 530-535 nm and 567 nm are connected with vacancy sulphur defects (V_S) [39] and the transition between the interstitial cadmium (I_{Cd}) donor level and the acceptor level [40], respectively.

Unlike the samples annealed at 350°C and 400°C, a dominant CdO phase was formed at 450°C, according to XRD results. Therefore, transitions to CdO phase are also likely in PL spectrum at 450°C. In this context, it can be said that the peak at 485 nm is due to the transition between the conduction band and valence band of CdO. Also, the transition at 530 nm can occur with near band-gap radiative combination due to the oxygen vacancy of CdO material [41].

In the PL results, while the peaks corresponding to CdS were found in the samples annealed at 350°C and 400°C, the presence of recessive $CdSO_3$ phase was not encountered. However, the sample annealed at 450°C exhibited the emission peaks indicating the presence of the dominant CdO phase as well as CdS. In this context, it was concluded that the crystal quality and phase structure of the samples play an important role in PL spectrum.

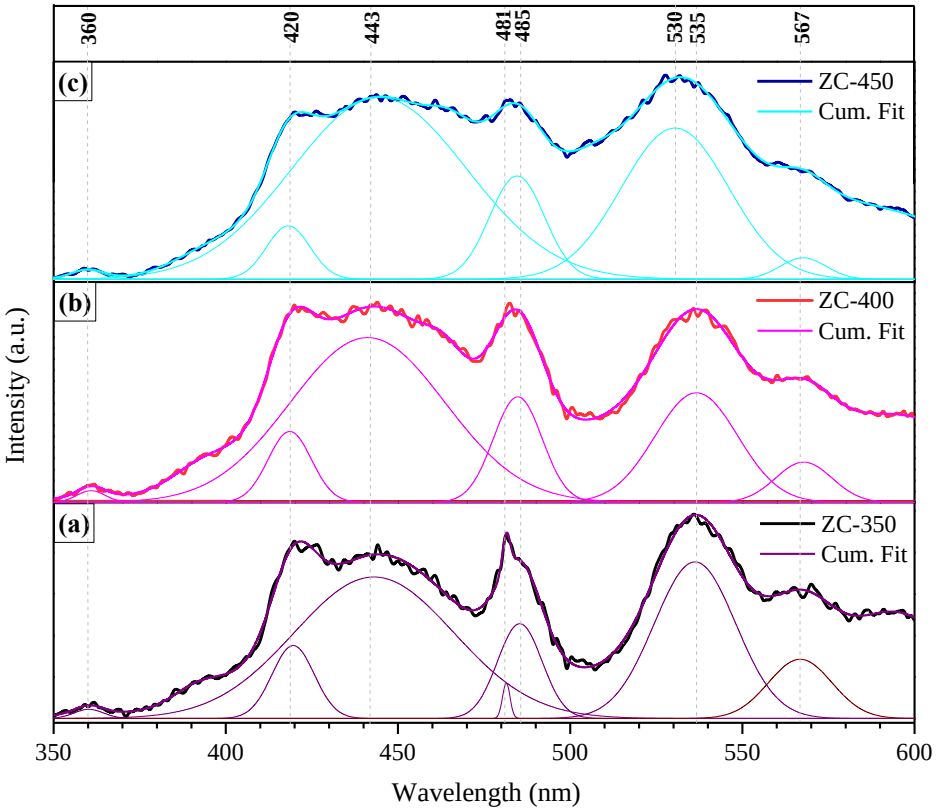

Figure 4. Photoluminescence spectra and corresponding deconvolution results of the samples post-annealed at 350°C, 400°C and 450°C

Refractive index curves of the samples obtained by ellipsometer measurements are shown in Figure 5. In the figure, the refractive index of all samples reached its maximum value around 520 nm, corresponding to the band gap of CdS. After 520 nm wavelength, the refractive index also decreased in response to increasing wavelength. As the annealing temperature increased from 350°C to 400°C, the refractive index also enhanced from 1.56 to 2.14 (at 520 nm). However, it decreased to 1.60 at the temperature of 450°C. It was thought that this change in the refractive indices was due to the transformation in the crystallization and phase structure, as seen in the XRD results. In general, it is seen that the refractive index values of the samples are low compared to the literature [42, 43]. It can be said that this situation is caused by ZnO seed layer which may act as an extinction layer.

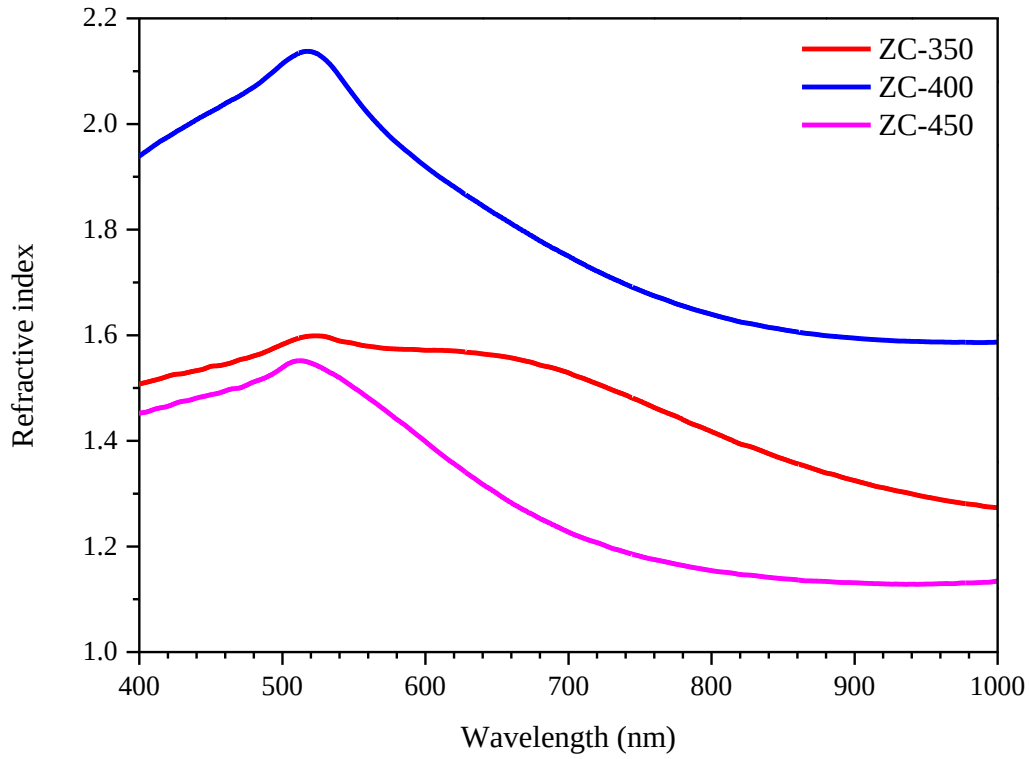

Figure 5. Refractive index curves of the samples post-annealed at 350°C, 400°C and 450°C

4. CONCLUSION

In this study, the effect of annealing temperature on CdS thin films grown on ZnO seed layer was investigated. CdS thin films and ZnO seed layer were coated by CBD method and wet processing, respectively. The samples were post-annealed at 350°C, 400°C and 450°C after film growth. XRD results showed that samples annealed at 350°C and 400°C had similar spectrum with cubic CdS and $CdSO_3$ oxide phases. When the annealing temperature reached 450°C, the crystal structure of the sample was completely changed. Accordingly, cubic CdS transformed into hexagonal structure and recessive $CdSO_3$ phase became dominant cubic CdO structure at 450°C. Transmittance curves showed that all samples had an absorption site of around 500 nm. Also, transmittance was improved when annealing temperature was increased from 350°C to 400°C. However, it was decreased at 450°C due to the transformation in the crystalline structure. PL spectra demonstrated that all samples annealed at different temperatures had a defect structure such as deep level and band edge emissions, host CdS, etc. In addition, PL peaks indicating the presence of CdO in the sample at 450°C were also observed in the spectrum. Ellipsometric measurements showed that the diffraction indices peak at 520 nm with the highest refractive index at 400°C.

Briefly, use of ZnO seed layer to improve the structural and optical properties of conventional CdS can provide a resource for improving device performance in CdTe solar cell applications. In the investigation of the annealing temperatures, it was concluded that post-annealing at 400°C would be more suitable for cell performance, considering the cubic nature of CdTe.

SIMILARITY RATE: 15%

ACKNOWLEDGEMENT

A. Çiriş is grateful the supports of Dr. Y. Atasoy for the preparation of the samples and discussion and Dr. M. Tomakin for the XRD, Optical and PL measurements.

A. Çiriş

REFERENCES

[1] Z. Fang, X. C. Wang, H. C. Wu, and C. Z. Zhao, "Achievements and challenges of CdS/CdTe solar cells," *International Journal of Photoenergy*, vol. 2011, 2011.

[2] S. G. Kumar and K. K. Rao, "Physics and chemistry of CdTe/CdS thin film heterojunction photovoltaic devices: fundamental and critical aspects," *Energy & Environmental Science*, vol. 7, no. 1, pp. 45-102, 2014.

[3] J. Poortmans and V. Arkhipov, *Thin film solar cells: fabrication, characterization and applications*. John Wiley & Sons, 2006.

[4] X. Wu, "High-efficiency polycrystalline CdTe thin-film solar cells," *Solar energy*, vol. 77, no. 6, pp. 803-814, 2004.

[5] G. Khrypunov, A. Romeo, F. Kurdesau, D. L. Batzner, H. Zogg, and A. N. Tiwari, "Recent developments in evaporated CdTe solar cells," (in English), *Solar Energy Materials and Solar Cells*, vol. 90, no. 6, pp. 664-677, Apr 14 2006, doi: 10.1016/j.solmat.2005.04.003.

[6] Y. Lee, W. Lee, Y. Kwon, G. Yeom, and J. Yoon, "Effects of CdS substrates on the physical properties of polycrystalline CdTe Films," *Thin Solid Films*, vol. 341, no. 1-2, pp. 172-175, 1999.

[7] S. Yılmaz, Y. Atasoy, M. Tomakin, and E. Bacaksız, "Comparative studies of CdS, CdS: Al, CdS: Na and CdS:(Al–Na) thin films prepared by spray pyrolysis," *Superlattices and Microstructures*, vol. 88, pp. 299-307, 2015.

[8] A. Hasnat and J. Podder, "Effect of annealing temperature on structural, optical and electrical properties of pure CdS thin films deposited by spray pyrolysis technique," 2012.

[9] H. Moutinho *et al.*, "Deposition and properties of CBD and CSS CdS thin films for solar cell application," *Thin Solid Films*, vol. 436, no. 2, pp. 175-180, 2003.

[10] N. R. Paudel, C. Xiao, and Y. Yan, "Close-space sublimation grown CdS window layers for CdS/CdTe thin-film solar cells," *Journal of Materials Science: Materials in Electronics*, vol. 25, no. 4, pp. 1991-1998, 2014.

[11] N. Romeo, A. a. Bosio, and A. Romeo, "An innovative process suitable to produce high-efficiency CdTe/CdS thin-film modules," *Solar Energy Materials and Solar Cells*, vol. 94, no. 1, pp. 2-7, 2010.

[12] S. Rondiya, A. Rokade, A. Funde, M. Kartha, H. Pathan, and S. Jadkar, "Synthesis of CdS thin films at room temperature by RF-magnetron sputtering and study of its structural, electrical, optical and morphology properties," *Thin Solid Films*, vol. 631, pp. 41-49, 2017.

[13] H. Metin and R. Esen, "Annealing effects on optical and crystallographic properties of CBD grown CdS films," *Semiconductor science and technology*, vol. 18, no. 7, p. 647, 2003.

[14] K. S. Ramaiah, R. Pilkington, A. Hill, R. Tomlinson, and A.-K. Bhatnagar, "Structural and optical investigations on CdS thin films grown by chemical bath technique," *Mater Chem Phys*, vol. 68, no. 1-3, pp. 22-30, 2001.

[15] J. Lee, "Comparison of CdS films deposited by different techniques: Effects on CdTe solar cell," *Applied Surface Science*, vol. 252, no. 5, pp. 1398-1403, 2005.

[16] J. Wang *et al.*, "Influences of the CdS nanoparticles grown strategies on CdTe nanorods array films: A comparison between successive ionic layer absorption and reaction and chemical bath deposition," *Electrochimica Acta*, vol. 202, pp. 32-38, 2016.

[17] X. Wu *et al.*, "High-efficiency CTO/ZTO/CdS/CdTe polycrystalline thin-film solar cells," National Renewable Energy Lab., Golden, CO.(US), 2001.

[18] R. Mane and C. Lokhande, "Chemical deposition method for metal chalcogenide thin films," *Mater Chem Phys*, vol. 65, no. 1, pp. 1-31, 2000.

[19] G. Kitaev, A. Uritskaya, and S. Mokrushin, "Conditions for the chemical deposition of thin films of cadmium sulphide on a solid surface," *Russ J Phys*, pp. 1101-1102, 1965.

[20] J. A. García-Valenzuela, M. R. Baez-Gaxiola, and M. Cota-Leal, "Problems with the Adhesion of Chemical-solution-deposited Films? Solving the Problem of CdS Thin Film Adhesion with a Very Simple and Green Chemical Procedure," *Chemistry Letters*, vol. 51, no. 2, pp. 177-181, 2022.

[21] H. Moualkia, S. Hariech, and M. Aida, "Structural and optical properties of CdS thin films grown by chemical bath deposition," *Thin Solid Films*, vol. 518, no. 4, pp. 1259-1262, 2009.

[22] L. Zhou, X. Hu, and S. Wu, "Effects of deposition temperature on the performance of CdS films with chemical bath deposition," *Surface and Coatings Technology*, vol. 228, pp. S171-S174, 2013.

[23] A. S. Najm *et al.*, "Mechanism of Chemical Bath Deposition of CdS Thin Films: Influence of Sulphur Precursor Concentration on Microstructural and Optoelectronic Characterizations," *Coatings*, vol. 12, no. 10, p. 1400, 2022.

[24] I. Mohammed, G. M. Gubari, N. P. Huse, A. S. Dive, S.-H. Han, and R. Sharma, "Effect of Cd/S ratio on growth and physical properties of CdS thin films for photosensor application," *Journal of Materials Science: Materials in Electronics*, vol. 31, no. 13, pp. 9989-9996, 2020.

[25] A. A. Prema *et al.*, "Effect of Ammonia concentration on structural and optical properties of CdS thin films prepared by CBD method," *International Journal of ChemTech Research*, vol. 10, no. 3, 2017.

[26] A. Kariper, E. Güneri, F. Göde, and C. Gümüş, "EFFECT OF PH ON THE PHYSICAL PROPERTIES OF CdS THIN FILMS DEPOSITED BY CBD," *Chalcogenide letters,* vol. 9, no. 1, 2012.
[27] S. Rondiya *et al.*, "Effect of bath temperature on optical and morphology properties of CdS thin films grown by chemical bath deposition," *Energy Procedia,* vol. 110, pp. 202-209, 2017.
[28] D. Byrne, E. McGlynn, K. Kumar, M. Biswas, M. Henry, and G. Hughes, "A study of drop-coated and chemical bath-deposited buffer layers for vapor phase deposition of large area, aligned, zinc oxide nanorod arrays," *Crystal growth & design,* vol. 10, no. 5, pp. 2400-2408, 2010.
[29] H. Metin and R. Esen, "Annealing studies on CBD grown CdS thin films," *Journal of Crystal Growth,* vol. 258, no. 1-2, pp. 141-148, 2003.
[30] H. Pushpalatha, S. Bellappa, T. Narayanaswamy, and R. Ganesha, "Structural and optical properties of CdS thin film obtained by chemical bath deposition and effect of annealing," 2014.
[31] A. Djelloul, M. Adnane, Y. Larbah, M. Zerdali, C. Zegadi, and A. Messaoud, "Effect of annealing on the properties of nanocrystalline CdS thin films prepared by CBD method," 2016.
[32] İ. Polat, S. Yılmaz, İ. Altın, E. Bacaksız, and M. Sökmen, "The influence of Cu-doping on structural, optical and photocatalytic properties of ZnO nanorods," *Mater Chem Phys,* vol. 148, no. 3, pp. 528-532, 2014.
[33] A. Çiriş *et al.*, "Alloying and phase transformation in CdS/CdSe bilayers annealed with or without CdCl2," *Materials Science in Semiconductor Processing,* vol. 91, pp. 90-96, 2019.
[34] A. L. Patterson, "The Scherrer Formula for X-Ray Particle Size Determination," *Physical Review,* vol. 56, no. 10, pp. 978-982, 1939, doi: 10.1103/PhysRev.56.978.
[35] S. Yılmaz, İ. Polat, M. Olgar, M. Tomakin, S. Töreli, and E. Bacaksız, "Physical properties of CdS: Ga thin films synthesized by spray pyrolysis technique," *Journal of Materials Science: Materials in Electronics,* vol. 28, no. 4, pp. 3191-3199, 2017.
[36] R. Kumar, R. Das, M. Gupta, and V. Ganesan, "Compositional effect of antimony on structural, optical, and photoluminescence properties of chemically deposited (Cd1− xSbx) S thin films," *Superlattices and microstructures,* vol. 59, pp. 29-37, 2013.
[37] P. Kumar *et al.*, "SHI induced enhancement in green emission from nanocrystalline CdS thin films for photonic applications," *Journal of luminescence,* vol. 147, pp. 184-189, 2014.
[38] K. Kaur, G. S. Lotey, and N. Verma, "Optical and magnetic properties of Fe-doped CdS dilute magnetic semiconducting nanorods," *Journal of Materials Science: Materials in Electronics,* vol. 25, no. 6, pp. 2605-2610, 2014.
[39] B. Ahmed, A. K. Ojha, and S. Kumar, "One-pot synthesis of Ni doped CdS nanosheets for near infrared emission and excellent photocatalytic materials for degradation of MB dye under UV and sunlight irradiation," *Spectrochimica Acta Part A: Molecular and Biomolecular Spectroscopy,* vol. 179, pp. 144-154, 2017.
[40] S. Yılmaz, İ. Polat, M. Tomakin, and E. Bacaksız, "Transparent and conductive CdS: Ca thin films for optoelectronic applications," *Applied Physics A,* vol. 126, no. 7, pp. 1-9, 2020.
[41] W. Xiaochun *et al.*, "Optical properties of nanometer-sized CdO organosol," *Journal of materials research,* vol. 13, no. 3, pp. 604-609, 1998.
[42] F. Lisco *et al.*, "High rate deposition of thin film cadmium sulphide by pulsed direct current magnetron sputtering," *Thin Solid Films,* vol. 574, pp. 43-51, 2015.
[43] F. Lisco *et al.*, "The structural properties of CdS deposited by chemical bath deposition and pulsed direct current magnetron sputtering," *Thin solid films,* vol. 582, pp. 323-327, 2015.